Thesis in fulfilment of
M.Sc. Mechanical Engineering

Aerodynamic analysis of design procedures for centrifugal fans

Abhishek Gangappa Hallur
Matriculation Number 752604

Düsseldorf
19. 09. 2024

First Supervisor
Prof. Dr.-Ing. Frank Kameier
Institute of Sound and Vibration Engineering
Maschinenbau und Verfahrenstechnik
Hochschule Düsseldorf
Münsterstr. 156
40476 Düsseldorf
✉ frank.kameier@hs-duesseldorf.de
𝑒 www.stroemungsakustik.de

Second Supervisor
Prof. Dr.-Ing. Bernd Boiting
Fachbereich Energie·Gebäude·Umwelt
Fachhochschule Münster
Stegerwaldstraße 39
48565 Steinfurt

✉ boiting@fh-muenster.de

Task description for a master's thesis of
Abhishek Gangappa Hallur, B.Eng.
Matriculation Number 752604

Aerodynamic analysis of design procedures for centrifugal fans

Within the scope of the Master's thesis, basic numerical strategies for the calculation of an aerodynamic industrial fan of radial design are to be analysed. In detail these are:

➢ Frozen rotor consideration,
➢ influence of the Reynolds number (speed) on dimensionless throttle characteristics,
➢ influence of friction and turbulence,
➢ influence of mesh quality (coarse, medium, fine) on accuracy and calculation time.

Furthermore, the design strategies for such centrifugal fans developed at the Institute are to be evaluated using the example of one single geometry. The ANSYS Multi-Physics tools and TCAE, which works with OpenFoam, are available for the flow calculations. An initial best-price evaluation for a systematic industrial calculation procedure for centrifugal fans is to be developed as a summarised result.

Time plan:

- Thorough investigation of the existing fan design methods at ISAVE   4 Weeks

- Developing a standard workflow for numerical simulations using TCAE   4 Weeks

- Conducting numerical simulations using the example geometry   8 Weeks

- Analysis of the results of numerical simulations   4 Weeks

- Documentation   8 Weeks

Prof. Dr.-Ing. Frank Kameier

Contents

List of Figures

List of Tables

1   Introduction

The recent energy crisis faced by the nations of the European Union due to global geopolitical issues has forced the Parliament of the European Union to undertake stringent energy saving measures. The revised Energy Efficiency Directive [1, L 231/1] published on 20th September 2023, forces the EU countries to collectively achieve an additional 11.7% savings in energy consumption by 2030. This step by the European Commission makes it necessary for the engineers and researchers working on the ground level to improve the efficiency of each and every product that consumes power, including centrifugal fans. In order to improve the efficiency of these fans, they need to be optimised and tested constantly. And numerical simulation method of testing these fans provides great advantage in terms of time, resources, and efforts. Within the scope of this thesis, basic numerical strategies such as influence of Reynolds number on dimensionless throttle characteristics, influence of friction and turbulence, and the influence of mesh quality on the accuracy and calculation time are to be analysed with a frozen rotor approach.

For simulating the fan models, commercially available CFD simulation tool TCAE, which is based on the open source tool OpenFOAM, is opted due to its comparatively lower licensing costs. The institute of ISAVE at Hochschule Düsseldorf hosts its own fan design tool which has been in use for over a decade for academic purposes. And in order to use it for research and commercial purposes, it has to be revalidated. Any difficulties in using the tool or drawbacks in the tool must be identified and discussed appropriately. A stable and reliable simulation methodology in TCAE in combination with the in-house fan design tool is to be developed and validated against an indigenous reference fan and also against results from atleast one other commercially available CFD simulation tool.

2   Discussion on Centrifugal Fan Literature

Centrifugal fans are a special type of turbomachines. One could also say that they are basically a school of fish in a vast ocean of turbomachines. Hence, to understand what centrifugal fans are, it is essential to have a basic idea of what turbomachines and fans in general are. Turbomachines can be described as rotodynamic devices that interact with a working fluid to generate or impart energy from or to the fluid in contact with the rotor [2, Ch. 1, p. 1]. This transfer of energy is always a continuous process and can never be periodic or step processes [3, Ch. 1, p. 3]. Also, this transfer of energy can be noted in the form of pressure and/or momentum changes of the fluid. The author in [3, Ch. 1.4, p. 3] draws the attention in particular to the fact that turbomachines are not to be confused with Positive Displacement Machines (PDMs) since turbomachines are responsible for a continuous transfer of energy by dynamic action. Whereas, in PDMs it is almost the opposite since the energy transfer is periodic and happens with moving boundaries that form confined spaces resulting in compression or expansion of the fluid. For example steam turbines are turbomachines where as steam engines are positive displacement machines. When the proper type of a pump is not specified, it is safe to assume it to be a turbomachine. But there are again, some pumps which are positive displacement machines, e.g. gear pumps. Other popular examples of positive displacement machines are internal combustion engines, which although interact with fluids to extract energy, are not turbomachines.

Turbomachines are classified based on several criteria. But based on the direction of energy flow, they are differentiated into two categories. Power generating turbomachines or power machines, where the energy flows from the fluid to the rotor. And power consuming turbomachines or working machines, where the energy flows from the rotor to the fluid. We are more interested in the power consuming turbomachines, since fans fall in this category. Other major types of power consuming turbomachines are pumps, blowers and compressors. Pumps differ from the rest as they handle incompressible fluids (liquids). Fans, blowers and compressors handle compressible fluids (gases) in general. Further, fans, blowers and compressors can be differentiated based on the pressure ratios they generate. Fans usually generate pressure ratios less than 1.07, blowers generate around 1.5 - 2, and compressors are capable of generating pressure ratios of 2.5 - 10. [3, Ch. 8.1, p. 307]

The author in [4, Ch. 1.3.2, p. 21] highlights a somewhat more technical definition of fans as stated in [5, Sec. 2, p. 2] and quoted below:

"A fan is a rotary-bladed machine which receives mechanical energy and utilizes it by means of one or more impellers fitted with blades to maintain a continuous flow of air or other gas passing through it and whose work per unit mass does not normally exceed 25000 J/kg."

The above definition is further supported by [6, Sec. 1, p. 1], which states:

"The upper limit of fan work per unit mass is normally 25 kJ kg^{-1}, corresponding to an increase of fan pressure of approximately 30 kPa for a mean density in the fan of 1.2 kg m^{-3}"

2.1   Classification of Fans

Based on how air (or gases in general) flows through the fan, [4, Ch. 1.3.2, p. 21] classifies fans into following five types:

- **Axial flow fans.** As the name suggests, in this type of fans the direction of flow of air is parallel to the axis of the impeller. These fans sometimes are also referred to as propeller fans or just propellers. The force applied by the blades on the air can be split into two components. The major component is in the axial direction and hence the flow of air in this direction. But there is also a small tangential component applied due to the blades' rotation. As a result of these two components, there is a slight spin of air around the impeller axis. A schematic diagram of a typical axial fan is shown below in Figure 2-1.
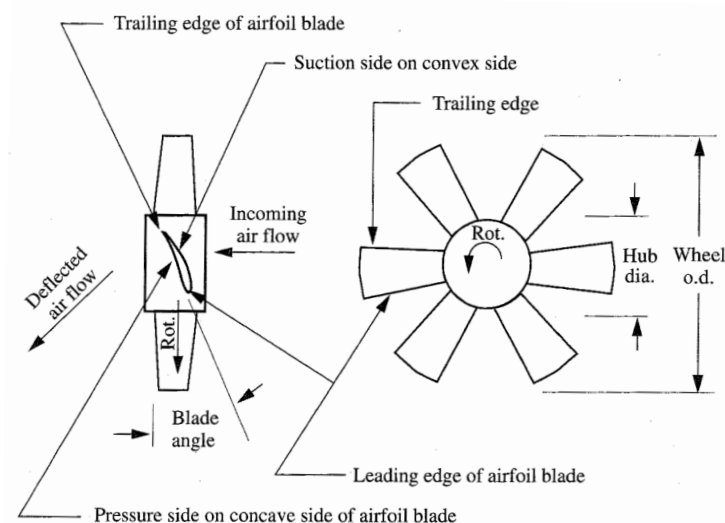
Figure 2-1: Schematic Representation of a Typical Axial Flow Fan [7, Ch. 2, p. 2.9].

- **Centrifugal flow fans.** Or simply referred to as centrifugal fans or radial flow fans, are the class of fans where the air enters axially and turns by an angle of 90° as it flows through the blades and exits the impeller in a radially outward direction. The blades due to their rotation, exert a tangential force on air flowing through them and thus rotate the air stream along with them. This rotation of air stream results in a centrifugal reaction leading to the outward motion of air. In case of centrifugal fans with a casing, the air streams which are thus flowing in outward direction along the entire circumference of the rotor are then collected by a scroll housing and merged

into a single outlet stream that exits the housing in a direction perpendicular to the impeller axis [7, Ch. 7, p. 7.1]. Figure 2-2 shows a typical centrifugal fan and Figure 2-3 shows an angular view of a centrifugal fan fitted in a scroll housing.
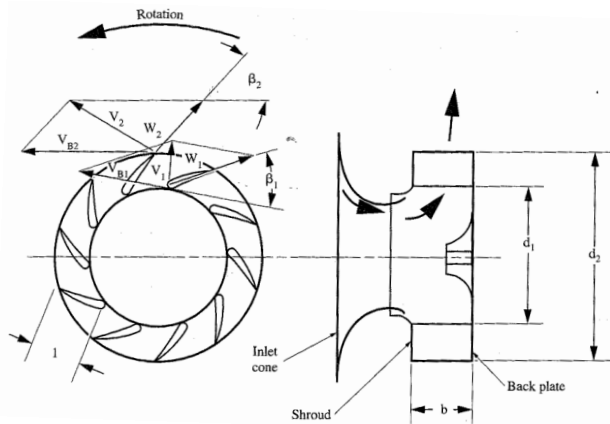
Figure 2-2: Schematic Representation of a Typical Centrifugal Fan with Backward Curved Airfoil Blades [7, Ch. 7, p. 7.5].
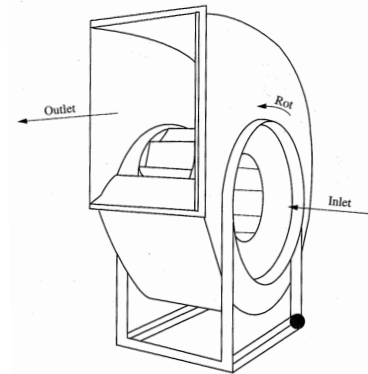
Figure 2-3: Angular Representation of a Typical Centrifugal Fan with Scroll Housing [7, Ch. 3, p. 3.12].

Centrifugal fans can further be classified based on their blade profiles. There are several blade profiles possible. Many of these are discussed in detail in [4, 7, 8]. Just to mention some as discussed in [7, Ch. 3, p. 3.8] are centrifugal fans with airfoil(AF) blades, backward-curved (BC) blades, backward inclined (BI) blades, radial tip (RT) blades, forward curved (FC) blades, and radial blades (RB). Each vary in their advantages, disadvantages, efficiencies and applications. Figure 2-4 schematically represents these six types of blade profiles in a descending order (from left to right) of their approximate maximum efficiencies.

Figure 2-4: Schematic Representation of some Common Centrifugal Fan Blades in Descending Order (from Left to Right) of Their Approximate Maximum Efficiencies [7, Ch. 7, p. 7.2].

- **Compound flow fans.** They are also known as axial-centrifugal fans, tubular centrifugal fans, in-line centrifugal fans or mixed flow fans [7, Ch. 3, p. 3.13]. The air in this type of fans enters the impeller in an axial direction and exits at an angle to the impeller axis. The blades exert force in two directions, viz. tangenially and radially outward (centrifugal reaction). Figure 2-5 shows a configuration of mixed flow fans with conical backplate and cylindrical housing.
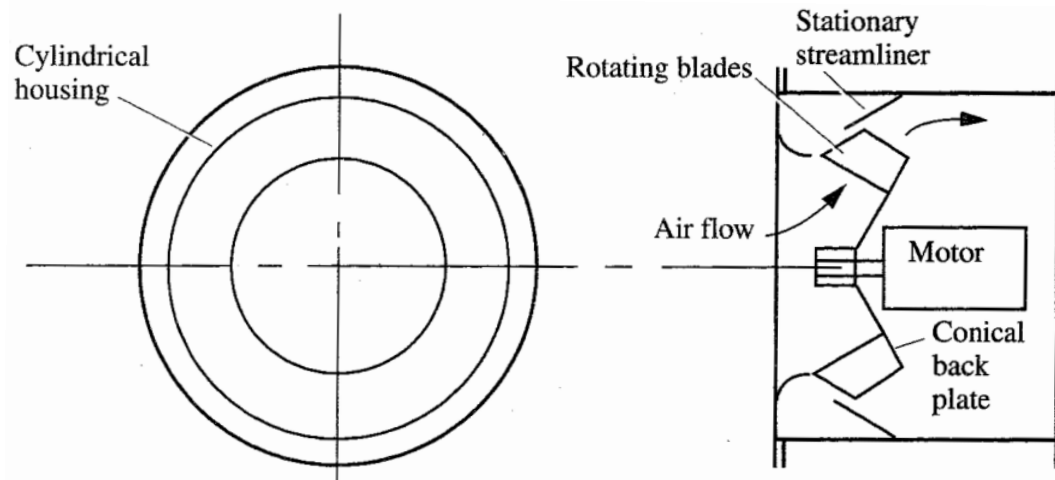
Figure 2-5: Schematic Representation of a Mixed Flow Fan with a Conical Back Plate and Cylindrical Housing [7, Ch. 3, p. 3.13].

- **Cross flow fans.** This class of fans is also known as tangential flow fans. These fans are distinguished by their streamline tangential flow of air at the outlet as shown in Figure 2-6. The blades generate and maintain a vortex with its axis parallel to the impeller shaft. The housing with its unique design, peels off a part of the outer layer of this vortex and feeds it to the diffuser. The uniqueness of this class of fans is that the air stream ends up flowing through the blade profile at least twice by the time it reaches the diffuser.
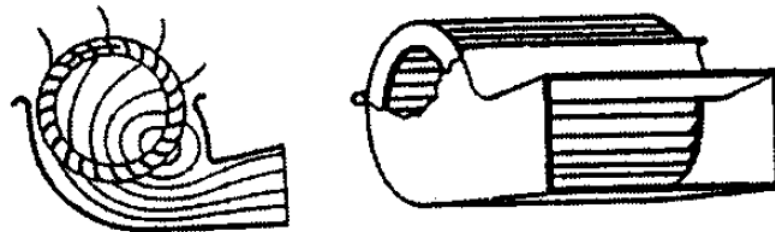
Figure 2-6: A Typical Cross Flow Fan [4, Ch. 1.3.2, p. 22].

- **Ring shaped fans.** These fans are also called vortex or regenerative blowers [7, Ch. 3, p. 3.20]. The fan contains a toric casing with a set of radially extending blades as shown in Figure 2-7. The blades rotate and impart centrifugal reaction and circular motion within the casing. Due to the curved surface of the casing, the air stream is redirected on to the blades resulting in the air stream coming in contact to one or more blades. The overall effect is a helical trajectory of the air stream.

1 Fluid   2 Blade   3 Casing   4 Inlet   5 Outlet
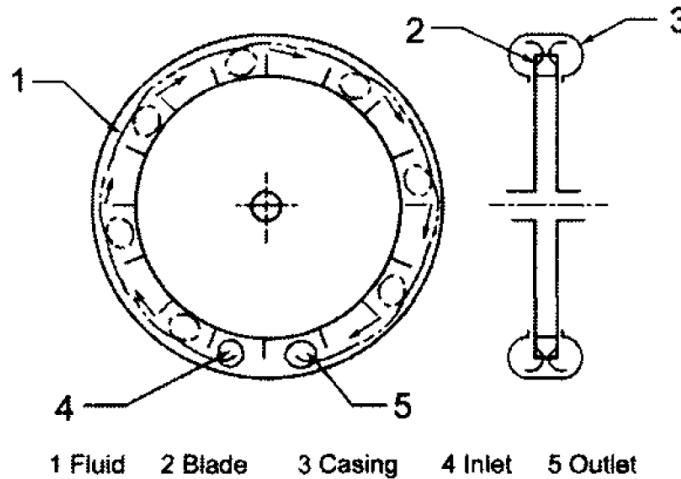
Figure 2-7: Schematic Representation of a Typical Ring Shaped Fan [4, Ch. 1.3.2, p. 22].

For a much detailed classification of fans, [7, Ch. 3, p. 3.1] is suggested. A much clear picture showing comparison of flow pattern through the blades in radial, mixed and axial flow fans is shown in Figure 2-8.
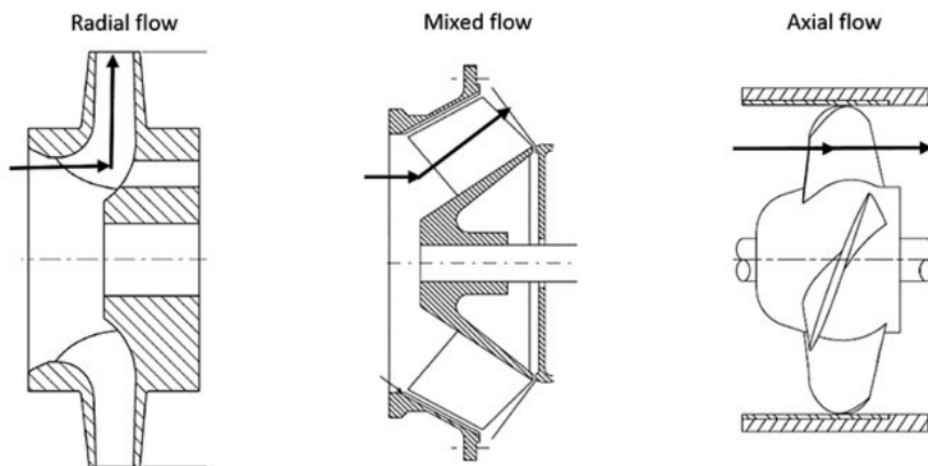
Figure 2-8: Schematic Representation Showing a Comparison of Flow Pattern through Radial, Mixed and Axial Flow Fans [9].

2.2   Designing of Fans

Fans, as discussed, are a class of turbomachines. Hence, most principles applied in designing of turbomachines are applicable in designing of fans too. These principles are discussed in various sections in detail by [2–4, 7, 8, 10]. A brief summary of the same principles is provided in the below sub-subsections.

2.2.1   Velocity Triangles

A velocity triangle, as the name suggests, is a triangle made up of velocity vectors. Needless to say, since it is a triangle, it must have three vectors that each represent fluid or blade velocities of the turbomachine in discussion. The three velocities that make up the triangle are:

- U_i**.** The circumferential velocity of impeller at any given point i on the blade profile. A schematic representation of this can be seen in Figure 2-9. This velocity is always parallel to the tangent at the impeller circumference and perpendicular to the radius through the point i.

- V_{ri}**.** The relative velocity of the fluid with respect to the impeller blade at any given point i that lies within the impeller. A schematic representation of this can be seen in Figure 2-10. This velocity is always tangential to either the blade profile or the fluid streamline that pass through the point i.

- V_i**.** The absolute velocity of the fluid at any given point i that lies within the impeller. The absolute velocity of the fluid V_i is the vectorial sum of the blade velocity U_i and the fluid relative velocity V_{ri}. Thus, $V_i = U_i + V_{ri}$. The vectorial representation of the same, as shown in Figure 2-11, is referred to as velocity triangles. Figure 2-11a shows the velocity triangle at the inlet of the impeller and Figure 2-11b shows the velocity triangle at the outlet of the impeller.

The velocity triangle can be drawn for any point i that lies within the impeller as mentioned, but it is a common practice to draw the triangles along the blade profile at the inlet $(i = 1)$ and outlet $(i = 2)$ of the impeller. Also, it is to be noted that the vectors making up an individual triangle should all be drawn at the same point i. Since the scope of this report deals only with centrifugal fans, the velocity vectors and triangles, shown in the figures below, are applicable to centrifugal fans only. For details on axial fan velocity vectors and triangles, the suggested material in Section 2.2 may be referred.
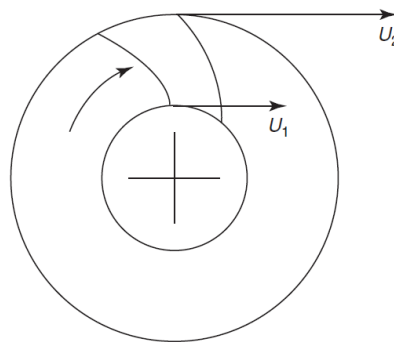
Figure 2-9: Peripheral Blade Velocities [3, Ch. 3, p. 86].

(a) Backward Curved (BC)
Blades.   (b) Radial Tip (RT) Blades.   (c) Forward Curved (FC) Blades.
Figure 2-10: Fluid Relative Velocities Along Various Blade Profiles [3, Ch. 3, p. 87].
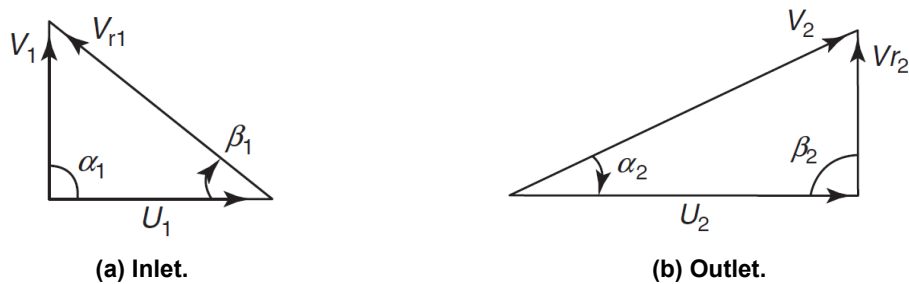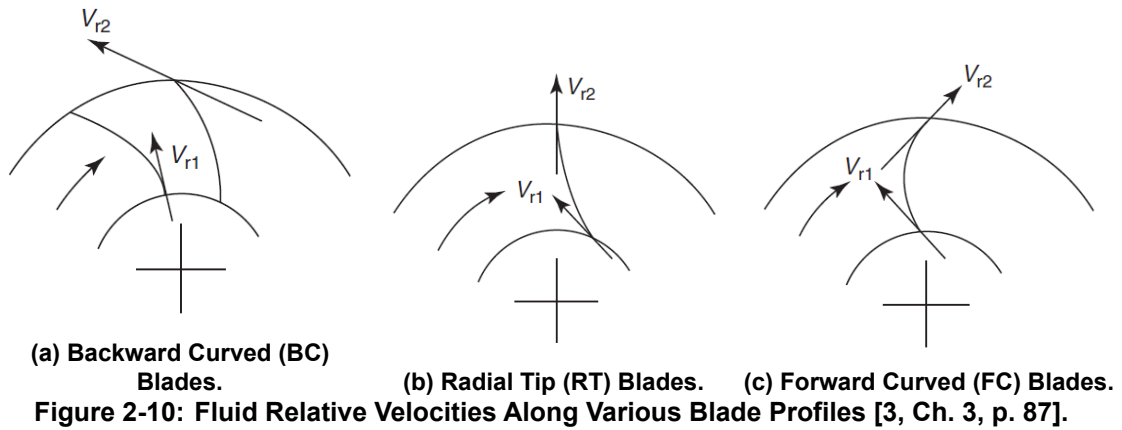
(a) Inlet.   (b) Outlet.
Figure 2-11: Typical Velocity Triangles for a Centrifugal Fan [3, Ch. 3, p. 93].

The angles α_i and β_i are the angles made by the fluid velocities and the blade profiles with blade velocity vectors respectively.

2.2.2   Euler Equations for Turbomachines

The Euler equations for turbomachines relate the power added or removed from the fluid to the characteristics of the turbomachine's blades [11, Ch. 12.3]. A very simplified derivation of this relation is to be found in [12, Ch. 6.5, p. 166]. The derivation follows under the assumption that the flow through the impeller is blade congruent,.i.e.- the flow of fluid follows the blade contour and the blades are of infinitesimally small thickness and are infinite in number. The derivation of Euler turbomachine equations as presented in [12, Ch. 6.5, p. 166] is briefed below.

As per the conservation of angular momentum, the following holds true.

$$\dot{m}(r_2\, V_{2u} \; - \; r_1\, V_{1u}) \; = \; \tau \tag{2.1}$$

Where, τ = torque

r_1 = radius at the inlet of the blade

r_2 = radius at the outlet of the blade

V_{1u} = absolute fluid velocity component in the peripheral direction at the inlet of the blade

V_{2u} = absolute fluid velocity component in the peripheral direction at the

outlet of the blade

$\dot{m}$ = mass flowrate

If W is the work done by applying a force of F through a distance of Δs,

$$W = F\Delta s \tag{2.2}$$

And since arc length is given by radius times the subtended angle,

$$\Delta s = r\Delta\phi \tag{2.3}$$

Which implies,

$$W = F\,r\,\Delta\phi \tag{2.4}$$

The torque, τ is given by,

$$\tau = r\,F \tag{2.5}$$

Making Equation 2.4,

$$W = \tau\Delta\phi \tag{2.6}$$

Since Power is work done in unit time, if we divide Equations 2.2 and 2.6 with Δt we get,

$$P = F\,\frac{\Delta s}{\Delta t}\ =\ \tau\,\frac{\Delta\phi}{\Delta t} \tag{2.7}$$

Equation 2.7 gives the power equation in terms of velocity for linear moving bodies and in terms of angular velocity for rotating bodies. Let us term this angular velocity as ω,

$$\omega = \frac{\Delta\phi}{\Delta t} = 2\pi n \tag{2.8}$$

Substituting ω in Equation 2.7,

$$P = \tau\omega \tag{2.9}$$

Substituting Equation 2.1 in Equation 2.9,

$$P = \dot{m}(\omega r_2 V_{2u}\ -\ \omega r_1 V_{1u})\ =\ \dot{m}(u_2 V_{2u}\ -\ u_1 V_{1u}) \tag{2.10}$$

Specific work is a quantity defined as work done per unit weight of the fluid. Let us denote this as Y. Now, keeping the Y value always positive, Equation 2.10 can be re-written as,

For turbines,

$$Y = (u_1 V_{1u}\ -\ u_2 V_{2u}) \tag{2.11}$$

For Pumps, Fans, and Compressors,

$$Y = (u_2 V_{2u}\ -\ u_1 V_{1u}) \tag{2.12}$$

2.2.3 Dimensional Analysis, Non Dimensional Parameters, and Specific Quantities

The concepts mentioned in the heading are tangled together when it comes to fluid mechanics and turbomachines in particular. Hence, all these concepts shall be discussed simultaneously, while still trying to maintain a systematized flow of information.

In turbomachinery, and in fluid mechanics in general, a vast majority of existing knowledge has come from experimental studies. And for these experiments, the use of cheaper or simpler models that replicate the actual prototypes in all possible manner has been inevitable. To have any valid and reasonable comparison between models and prototypes, the experiments should be governed by the laws of similarity. In other words, the model must satisfy conditions of physical similarity with the prototype. Dimensional analysis is the tool that exploits the principles of these physical similarity between the model and the prototype to help solve complex problems of physics with a mathematical approach. It involves disintegrating the dependent and independent parameters, of a variable of interest, into their corresponding fundamental dimensions, later using them to arrive at dimensionless groups followed by experimental procedures to determine the relationship between these dimensionless groups, finally paving the way to form the equation or formula for the variable of interest. Out of the many techniques available to perform dimensional analysis, the Buckingham π theorem is the most popularly used, which in turn is a formalization of Rayleigh's method of dimensional analysis. [13, Sec. 5, p. 159]

In centrifugal fans, the following important dimensionless parameters can be defined:

$$\Phi = \frac{Q}{ND^3} \quad \text{Flow Coefficient} \tag{2.13}$$

$$\Psi = \frac{gH}{N^2D^2} \quad \text{Head or Pressure Coefficient} \tag{2.14}$$

OR

$$\Psi = \frac{2\,\Delta p}{\rho U^2} \quad \text{Head or Pressure Coefficient} \tag{2.15}$$

$$\Pi_1 = \Phi\Psi = \frac{P}{\rho N^3 D^5} \quad \text{Pumping Power Coefficient} \tag{2.16}$$

$$\Pi_{shaft} = \frac{\Pi_1}{\eta} = \frac{\Phi\Psi}{\eta} \quad \text{Shaft Power Input Coefficient} \tag{2.17}$$

$$Re = \frac{ND^2}{\nu} = \frac{ND^2}{\mu/\rho} \quad \text{Reynolds Number} \tag{2.18}$$

$$\Pi_2 = \frac{\Delta p}{\rho U^2} \tag{2.19}$$

And the following specific quantities can be identified:

$$N_s \text{ or } \sigma = \frac{NQ^{1/2}}{(gH)^{3/4}} = \frac{\Phi^{1/2}}{\Psi^{3/4}} \quad \text{Specific Speed} \tag{2.20}$$

$$D_s \text{ or } \delta = \frac{D(gH)^{1/4}}{Q^{1/2}} = \frac{\Psi^{1/4}}{\Phi^{1/2}} \quad \text{Specific Diameter} \tag{2.21}$$

It may be noted that for most of the formulae listed above, the notations and form are as mentioned in [2, Ch. 1.2, p. 8] [3, Ch. 1.13-1.14, p 32-33]. But the same dimensionless numbers and specific numbers are also discussed in the rest of the literature mentioned in Section 2.2 with different form and notations.

2.3   Selection of Fans

For a given operating condition defined by the required fluid volume flow rate $(\dot{V})$ and fluid total head (Δp_t), selecting a fan involves a lot of challenges like selecting the right type of fan and selecting the right dimensions for the chosen type of fan. It is possible to meet the required conditions by choosing a fan type and dimensions that exceed the needs. But this will not be an optimal choice since the fan will result in excess operating costs and operating conditions that might be detrimental. At the same time, a fan that does not meet the required conditions is too of no use. Hence, selecting a fan that just meets the required conditions is an optimal choice.

Otto Cordier, in 1953, published a diagram, as shown in Figure 2-12a, to choose optimal fans by plotting optimum values of specific diameter (δ_{opt}) and specific speed (σ_{opt}) on a logarithmic scale [14, Sec. 1, p. 354]. It is to be noted that [14, Sec. 1, p. 354] has referred to specific diameter as "Diameter number" and specific speed as "Speed number" as seen in Figure 2-12. For a given operating point defined by the fluid volume flow rate and fluid total head, if one is limited by the shaft speed, then by referring to the Cordier diagram, it can easily be decided as to what type of fan suits the needs and further the optimal diameter of the impeller for the same operating point can also be calculated. And contrarily, if one is limited by the impeller diameter, then it is possible to calculate the optimal shaft speed that is needed to meet the operating point. In both the cases, the optimum refers to the maximum efficiency that can be achieved.

In Figure 2-12b, it can be observed that axial turbomachines posses high specific speed and low specific diameter, radial turbomachines posses low specific speed and high specific diameter and the mixed flow turbomachines occupy the middle ground. This placement of different types of turbomachines on the Cordier diagram is based on the experimental results from Cordier [14, Sec. 1, p. 354]. Bommes states in [15] that one can expect high efficiency centrifugal fans in the region $0.16 \leq \sigma \leq 0.63$. And this region, with a slight
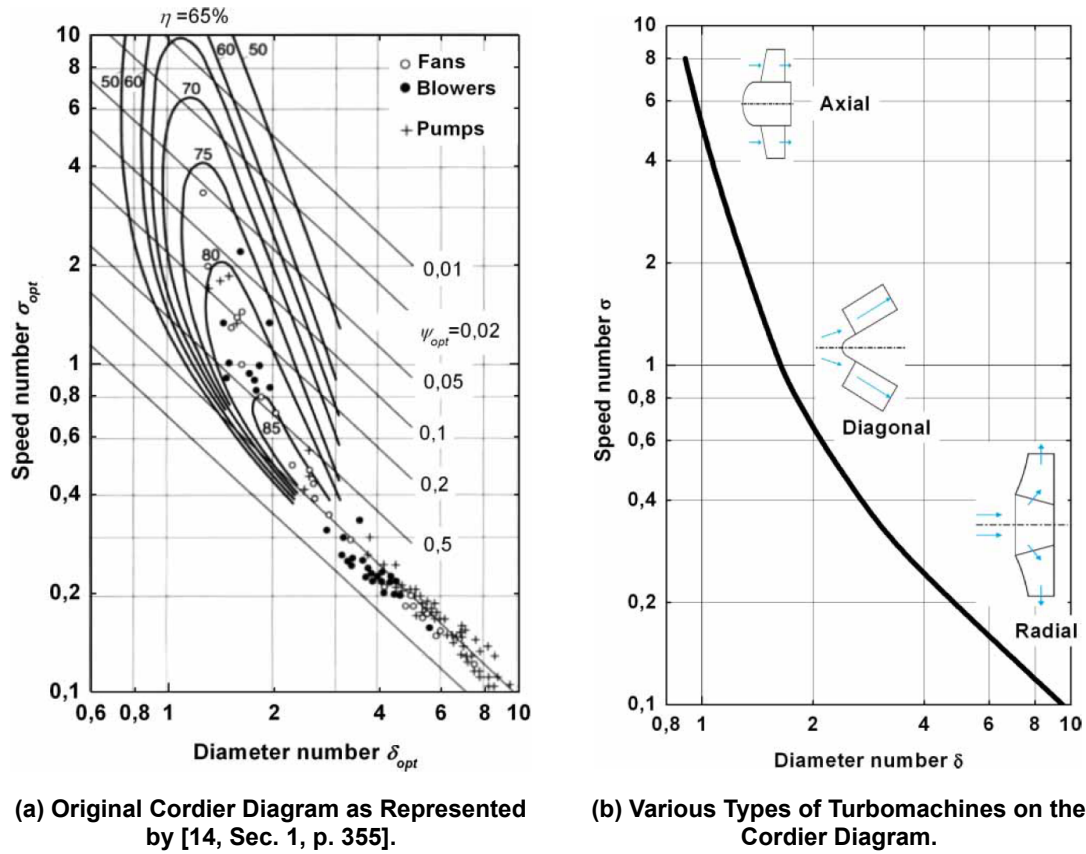
(a) Original Cordier Diagram as Represented by [14, Sec. 1, p. 355].

(b) Various Types of Turbomachines on the Cordier Diagram.

Figure 2-12: Cordier Diagram and Placement of Various Types of Turbomachines on It [14, Sec. 1, p. 355].

modification of $0.2 \leq \sigma \leq 0.63$ as per [16, p. 29] and as shown in Figure 2-13, has been colloquially referred to as Bommes region on the Cordier diagram by researchers at the institute of ISAVE in Hochschule Düsseldorf.
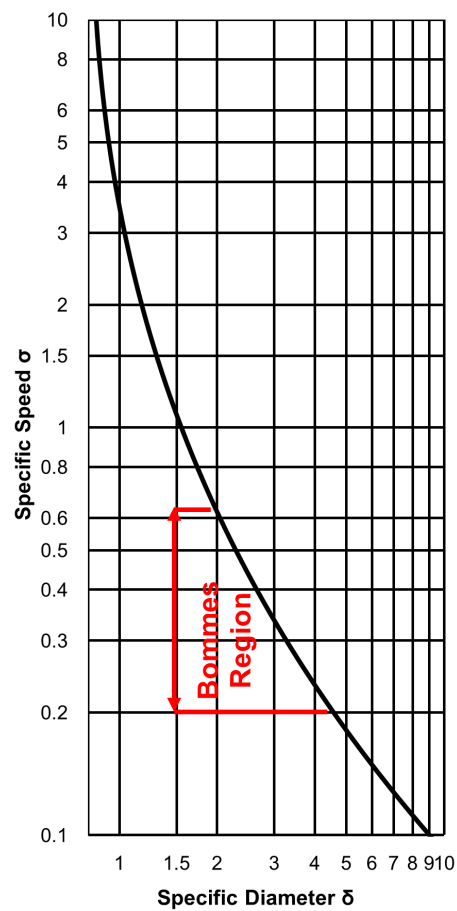
Figure 2-13: Bommes Region on Cordier Diagram [17].

3 Design Methodologies

The methodology for fan design being used at the institute of ISAVE was developed by Dr. Leonhard Bommes. It was later studied, developed and significantly automated by various professors and researchers at ISAVE. A brief introduction to these strategies and their development is provided in the following sections.

3.1 Bommes Methodology

Dr. Leonhard Bommes (1920-2011) worked as a professor of turbomachinery at the engineering school of Düsseldorf from 1964 and continued his position at the Fachhochschule Düsseldorf (now Hochschule Düsseldorf), founded in 1971, until his retirement in 1986 [18]. He made several significant contributions in the field of fans and centrifugal fans. One of his major contributions is a methodology for designing optimal centrifugal fans for any given operation point described by the volume flow rate ($\dot{V}$), total pressure rise (Δp_t), mean density of the fluid (ρ_m), and the impeller rotational speed (n) or the outer diameter of the impeller (D_2) [15, 19]. This strategy or design methodology was based on the knowledge gained by Dr. Bommes over years of research and experience through his work at Pollrich GmbH and Fachhochschule Düsseldorf. Hence, some of the significant formulae described in [15] are purely empirical. The entirety of [15] can be summarised as in Figure 3-1.

The Bommes methodology was a purely pen and paper - manual methodology. All the calculations were done manually and the final fan design drawn manually. The design of the impeller is pretty straight forward and is based on semi-empirical formulae. These impeller design formulae as seen in [15] are used to date with little or no modifications. The complexities and ambiguities arise when one wants to design the spiral casing with parallel walls. Parallel walled spiral casings are preferred over other designs due to their relative ease of manufacturing and comparatively good degree of energy conversion from fluid velocity (kinetic energy) to static pressure (pressure energy) [15, 20, Ch. 3.6, p. 72]. As per [20, Ch. 3.6, p. 72] the optimal casing contour is given by Equation 3.1. It further presents a good explanation on how to manually construct the design of a spiral casing using Equation 3.1.

$$\ln \frac{r_a}{r_z} = \frac{\dot{V}'}{2\pi \cdot BK}\,\phi \tag{3.1}$$

Where, ϕ = arbitrary polar angle

r_a = radius of the spiral at ϕ

r_z = radius of the spiral at $(\phi = 0)$

B = width of the spiral casing, i.e.- the distance between the parallel walls
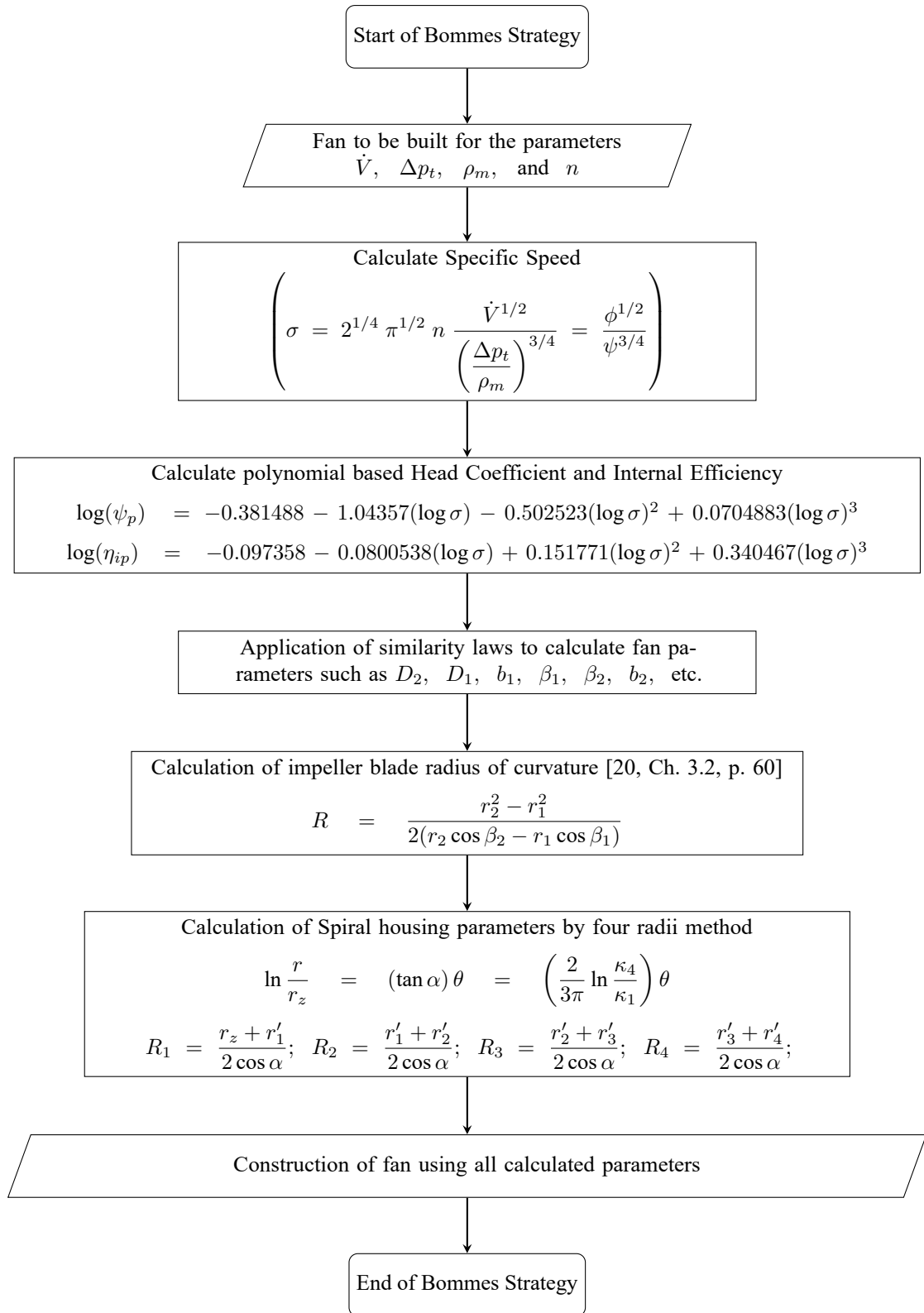
Figure 3-1: Summary of Bommes Strategy.

$$K = c_{2u} r_2$$
$$\dot{V}' = \text{volume flowrate}$$

On the other hand [15] uses a slightly different equation, Equation 3.2, to calculate the spiral casing. Though both the equations, Equation 3.1 and 3.2, produce logarithmic

spirals, they are not the same. Bommes calls the spiral designed using Equation 3.1 as the "Einheitssilhouette" and mentions that this spiral has proven itself efficient for the specific speed values ranging $0.16 \leq \sigma \leq 0.63$ [15] or $0.2 \leq \sigma \leq 0.63$ [16, p. 29].

$$\ln \frac{r}{r_z} = \tan(\alpha)\theta = \left(\frac{2}{3\pi} \ln \frac{\kappa_4}{\kappa_1}\right) \theta \qquad (3.2)$$

Where, r_a = radius of the spiral at θ

r_z = radius of the spiral at $(\theta = 0)$

α = spiral pitch angle

θ = arbitrary polar angle

$\kappa_1 \geq \dfrac{2}{3}$

$\kappa_4 \geq 0.9$ and ≤ 1.1

In the Bommes method the value of r in Equation 3.2 is solved at four pole angles, i.e.- $\theta = \dfrac{\pi}{2}, \pi, \dfrac{3\pi}{2}$, and 2π, yielding the four radii, viz. r'_1, r'_2, r'_3, and r'_4 respectively. The physical significance of the two variables κ_1 and κ_4 is shown in Equation 3.3 and Figure 3-2.

$$r_1' = \kappa_1 D_2 \quad \text{at} \quad \theta = \frac{\pi}{2} \qquad (3.3\text{a})$$

$$r_4' = \kappa_4 D_2 \quad \text{at} \quad \theta = 2\pi \qquad (3.3\text{b})$$
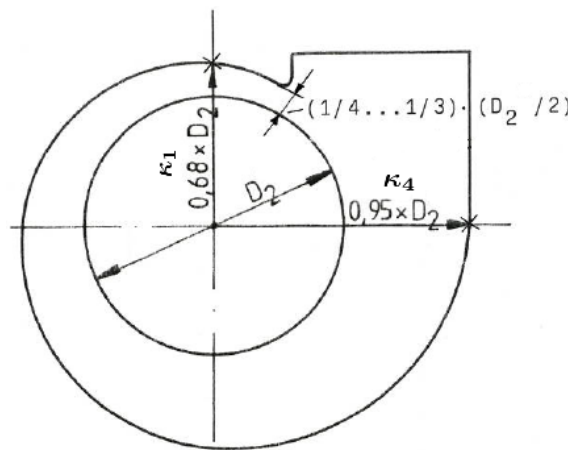
Figure 3-2: Bommes Spiral Showing κ_1 and κ_4 [21, Sec. 4.5, p. 73].

In the [20, Ch. 3.6, p. 75] methodology, the actual radii of the four quadrants forming the spiral and consequently their centers are determined schematically. Whereas in the [15] methodology the radii of the four quadrants forming the spiral, viz. R_1, R_2, R_3, and R_4 are determined mathematically as shown in Equation 3.4.

$$R_1 = \frac{r_z + r_1'}{2\cos\alpha}; \quad R_2 = \frac{r_1 + r_2'}{2\cos\alpha}; \quad R_3 = \frac{r_2 + r_3'}{2\cos\alpha}; \quad R_4 = \frac{r_3 + r_4'}{2\cos\alpha}; \quad (3.4)$$

There is no discussion in [15] on how to construct the fan design manually using the four radii determined from Equations 3.2 and 3.4. Rather, the construction of the the spiral is intuitive and has to be inferred from the diagram presented in Figure 3-3, derived from [15]. However, it is very much possible to use the the method described in [20, Ch. 3.6, p. 75] to construct a spiral designed using Equations 3.2 and 3.4. But this has not been verified or mentioned in any of the available literature. And these manual methods of constructing the spiral will not be discussed further in this thesis, since in the modern times with the advancements in CAD construction software, the manual methods are of pretty much no use. The four spiral components obtained from Equations 3.2 and 3.4 can easily be constructed within most CAD software using a 3 point arc option or similar.
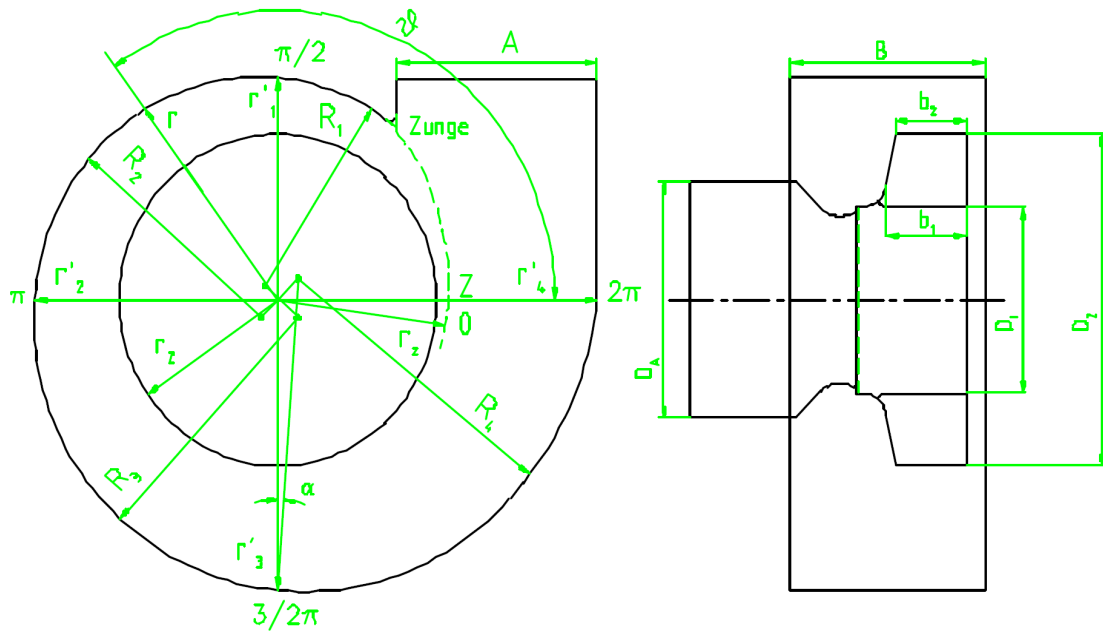
Figure 3-3: Physical Dimensions and Their Nomenclature on a Bommes Fan [15].

3.2   Excel Tool Methodology

The Bommes strategy was meant to be a manual design technique. The idea of automating the Bommes strategy came as early as in 1987 by Güntzel and Gottschalk [21, App., p. 90], wherein an automation code was written in the programming language BASIC. Later in 2001, Müller [22, Sec. 4, p. 13] incorporated the process of solving for the fan design parameters as well as the four radii (R_1, R_2, R_3, and R_4) for upto four fans in a spreadsheet (Microsoft Excel in this case), followed by displaying them on a Cartesian coordinate system for further comparison with the loss free logarithmic spiral. In the same thesis, Müller also laid down the initial idea of optimising the width of the spiral designed using Bommes method (presumably), to match the width of a logarithmic spiral designed using

Equation 3.1. The only thing being that the feedback loop to vary the control parameter b_1 (impeller blade inlet width) for optimising the spiral width was a manual technique based on visual perception and trial and error method. And here arise a few ambiguities. The first being the control parameter, i.e.- b_1, which Müller uses to optimise the spiral width. The word "presumably" is used since Müller does not make it clear if the four radii spiral based on Equation 3.2 (Bommes spiral) is being optimised or the spiral based on Equation 3.1 (logarithmic spiral). The only spiral width that can be changed by varying b_1 is the logarithmic spiral, as per Equation 3.5 [22, Sec. 4, p. 14]. The Bommes four radii spiral can be controlled only via the two semi-empirical constants κ_1 and κ_4. And assuming that Müller changes the logarithmic spiral width to match the Bommes spiral width, the idea of optimisation of spiral width itself loses the meaning. The second ambiguity arises in the way Müller calculates x and y coordinates for the logarithmic spiral. Müller in [22, Sec. 4, p. 14] gives Equation 3.5 as means to calculate x and y coordinates for the logarithmic spiral. If r_a from Equation 3.1 is resolved into its x and y components, the similarities between Equations 3.1 and 3.5 show up. But the fact that Müller uses impeller blade inlet width (b_1) instead of casing width (B) to resolve for x and y coordinates is not explained in his literature.

$$f_{(x)} = \frac{D_2}{2} \cdot e^{\left(\frac{\zeta \cdot \dot{V}}{2 \cdot \pi b_1 \cdot k}\right)} \cdot \cos\left(\zeta\right) \tag{3.5a}$$

$$f_{(y)} = \frac{D_2}{2} \cdot e^{\left(\frac{\zeta \cdot \dot{V}}{2 \cdot \pi b_1 \cdot k}\right)} \cdot \sin\left(\zeta\right) \tag{3.5b}$$

Where, b_1 = impeller blade inlet width

ζ = arbitrary polar angle

$k = \Delta p \cdot \dfrac{\left[\dfrac{D_2}{2}\right]}{\rho \cdot u_2}$

$u_2 = \dfrac{D_2 \cdot \pi \cdot n}{60}$

The next significant developments in the direction of automating and enhancing the Bommes strategy happened between the years 2007 and 2009, when the department of Fluid Mechanics and Acoustics at Fachhochschule Düsseldorf involved itself in the research project [19]. Within the framework of this project, Horvat further improved the spreadsheet (Microsoft Excel) method of designing centrifugal fans. It is to be noted that though this methodology is referred to as excel methodology, its core principle is still based on [15], i.e.- the Bommes Methodology. The excel method offers users an option to design upto four fans

simultaneously in either a spreadsheet format or via an interactive graphical user interface (GUI) based on UserForms in visual basic application (VBA). Additionally, the excel sheet with the final fan design parameters is further coupled to a commercial CAD software, Autodesk Inventor, and the fan model within Autodesk Inventor is parametrised. This gives users significant advantage in designing new fans. All one needs to do is enter the required fields in the excel GUI, viz. volume flowrate ($\dot{V}$), total pressure rise (Δp_t), mean density of the fluid (ρ_m), and the impeller rotational speed (n) or the outer diameter of the impeller (D_2) and the 3D design of the fan is readily available in Autodesk Inventor. Horvat follows closely the method used by Müller and designs two spirals for each fan. The first is the Bommes' four radii spiral (or the Einheitssilhouette) which takes into account the fluid losses and the second is the logarithmic spiral as per Equation 3.1 which does not take into account any losses and assumes an ideal flow through the casing. To plot the logarithmic spiral in excel, Horvat uses similar approach as Müller and resolves the components as per Equation .

$$f_{(x)} = \frac{D_2}{2} \cdot e^{\left(\frac{\zeta \cdot \dot{V}}{2 \cdot \pi b_2 \cdot k}\right)} \cdot \cos(\zeta) \tag{3.6a}$$

$$f_{(y)} = \frac{D_2}{2} \cdot e^{\left(\frac{\zeta \cdot \dot{V}}{2 \cdot \pi b_2 \cdot k}\right)} \cdot \sin(\zeta) \tag{3.6b}$$

Where, b_1 = impeller blade inlet width

$\qquad \zeta$ = arbitrary polar angle

$$k = \Delta p \cdot \frac{\left[\frac{D_2}{2}\right]}{\rho \cdot u_2}$$

$$u_2 = \frac{D_2 \cdot \pi \cdot n}{60}$$

As it can be observed in Equation 3.6, Horvat uses b_2 as opposed to B by Mode in [20, Ch. 3.6, p. 73] and b_1 by Müller in [22, Sec. 4, p. 14]. He supports this change by stating that the use of b_1 is a special case where the shroud angle $\gamma = 0°$ and as a result $b_1 = b_2$. He further states that in order to successfully optimise the spiral width, a change in the shroud angle (γ) is necessary [19, Sec. 4.3, p. 36]. In [17], under the VBA module "ah_Solver_Control_log_Spirale" Horvat defines the VBA sub procedures "Solver_Vent_#_eta()" (# is to be replaced by the corresponding fan number, i.e.- 1 to 4) responsible for controlling the solver functions needed to optimise the spiral width. And in these sub procedures, Horvat varies b_1 and γ, which then influence the b_2 value (see Figure 3-4 for reference) leading to a change in the spiral width as per Equation 3.6. It is

clear that the so optimised spiral has an influence on the impeller dimensions and hence the impeller after optimisation is no more within the boundaries of Bommes methodology.
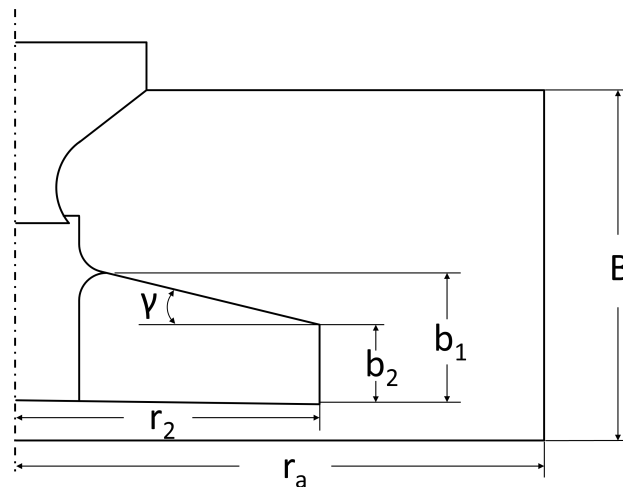
Figure 3-4: Schematic Representation of a Bommes Fan Cross-section.
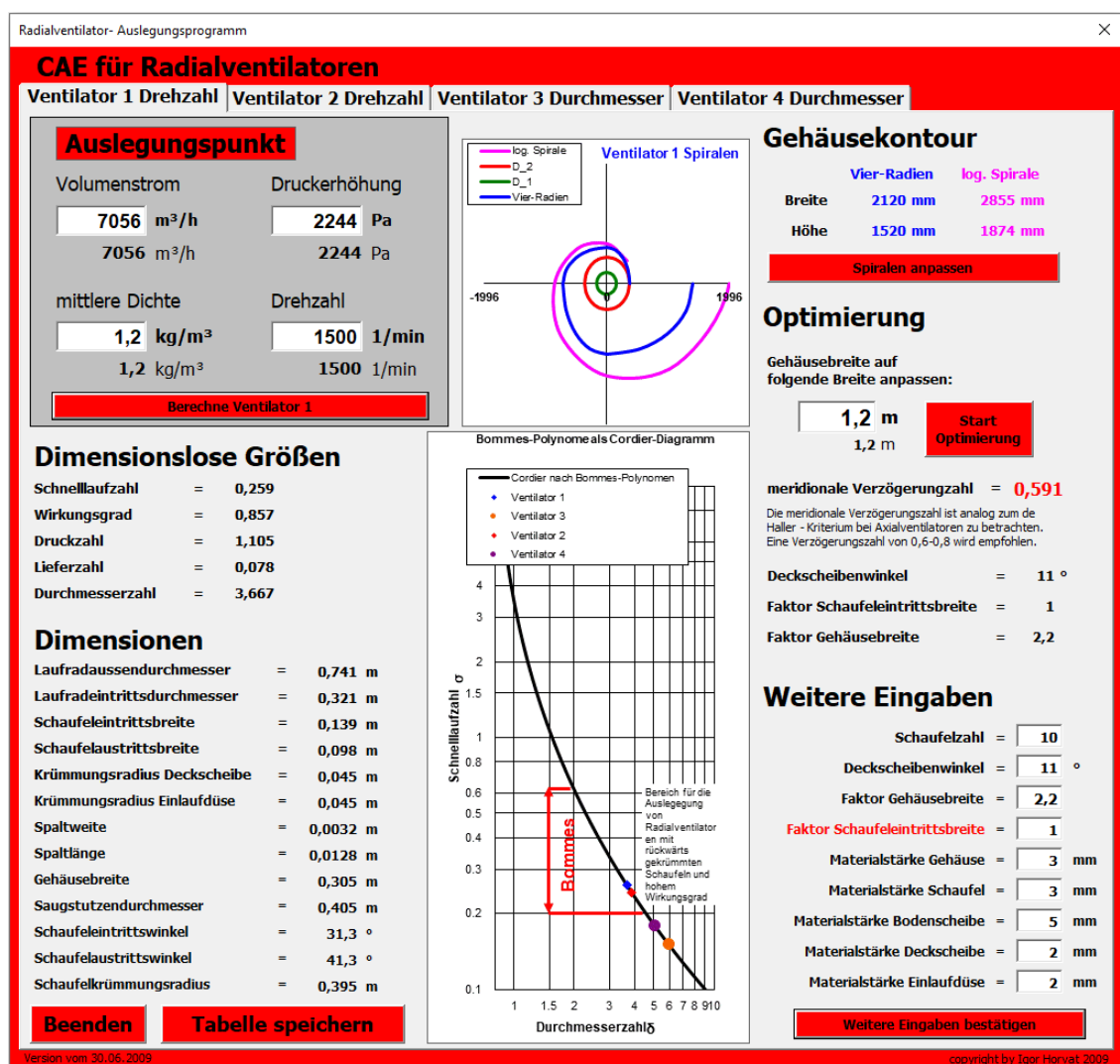
Figure 3-5: Graphical User Interface from the Excel Tool 2009 [17].

Figure 3-5 shows the graphical user interface (GUI) of the excel tool. The GUI can be

launched by clicking on the "Starte GUI" button on the "Auslegung" sheet in the excel. Each fan has its own tab for the design procedure. Figure 3-5 is showing the tab for designing the first fan. The grey area on the top left, with the heading "Auslegungspunkt", contains the text boxes to enter the design point values at which the user wants to design the fan and the red button "Berechne Ventilator #" within the grey area is to be used to generate the fan. Once the fan is generated, its dimensionless properties like the specific speed (σ), fan efficiency (η), pressure co-efficient (Ψ), flow co-coefficient (ϕ), and specific diameter (δ) are listed under the heading "Dimensionlose Größen" and the physical dimensions needed to construct and manufacture the impeller are listed under the heading "Dimensionen", both just below the grey input area. In the center, at the top, the casing spirals as per Equation 3.2 (Bommes spiral or the four radii spiral) in blue and Equation 3.6 (logarithmic spiral) in magenta are displayed. The red and green circles in the same graph display the impeller outlet and impeller inlet diameters respectively. Below the spiral graph is the Cordier diagram showing the Bommes region and each fan as dots on the curve. On the extreme right side, under the heading "Gehäusekontour", the spiral widths (along X axis, Breite) and heights (along Y axis, Höhe) are displayed for Bommes spiral in blue and for logarithmic spiral in magenta. The Bommes spiral can be fitted on to the logarithmic spiral by clicking the button "Spiralen anpassen". Just below it are the advanced options such as the optimisation of the logarithmic spiral as per user defined spiral width under the heading "Optimierung" and further fine tuning options under "Weitere Eingaben". Optimisation is achieved by entering a user desired value in the text box in the optimisation area followed by clicking on the red button "Start Optimierung". The user is then expected to click on the "Spiralen anpassen" button to perform the curve fitting and successfully conclude the optimisation. The user is also displayed the deceleration factor which shows the reduction of meridional velocity that the fluid undergoes when it passes through the blade passages [15]. And at the last on the bottom right are the advanced fine tuning options like the number of blades, the shroud angle, material thickness for each component, etc.

Once the user seems satisfied with the design, it can be saved in the excel sheet by clicking the "Tabelle speichern" button. The sheet "Inventor" in the excel lists all the physical parameters that are used to parametrise the 3D CAD model of the fan in Autodesk Inventor (here after referred to as Inventor). To successful finalise the fan design, the Inventor assembly file must be opened and refreshed to load the newly designed fan and here the user might be required to further fine tune the fan based on visualisation of the fan 3D CAD model. For this purpose, the user is required to adjust the values of the fine tuning options under "Weitere Eingaben" and click the button "Weitere Eingaben bestätigen" to bring the changes into effect. There are however a few things to be noted here. The changes in either spiral width optimisation or the fine tuning options do not take into consideration the effect or changes that they will have on each other. This means that if the user optimises the spiral

width, then the values under the fine tuning options are refreshed, resulting in the loss of previously entered values. The same goes the other way around. If the user fine tunes the fan by changing the values in the fine tuning options, then the spiral width optimisation is lost. Also, the user must take care to choose values for the fine tuning options in such a way that the resulting fan remains within the boundaries of the Bommes methodology. In some cases, the impeller extrudes below the casing bottom wall. In such cases, the casing width factor (Faktor Gehäusebreite) can be increased. And the distance between the hub and the casing bottom wall must not be too wide or too narrow. At the moment, this tuning is done based on the user's experience in designing the casing. However, care must be taken to keep the casing width factor (Faktor Gehäusebreite) between 2 and 3. Another hint in deciding suitable casing width factor comes from the Bommes methodology. Bommes mentions in [15] that the casing outlet should be a square or must have as little deviation from a square as possible. He further mentions that the width of the casing outlet (this width is orthogonal to the previously discussed casing width) must be chosen such that the resulting outlet area is similar to the suction pipe area, as shown in Equation 3.7.

$$A = \frac{\pi D_A{}^2}{4B} \tag{3.7}$$

Where, A = width of the casing outlet

D_A = diameter of the suction pipe ϕ

B = width of the spiral casing, i.e.- the distance between the parallel walls

As per [20, Ch. 3.6, p. 75], the tongue of the casing must be placed at an angle of $45°$ or above. Having the freedom to choose the tongue position, suitable casing outlet width (A), and the casing width (B) makes it difficult to parametrise the 3D CAD model for the casing. One way to solve this could have been to get one of the discussed parameters (either A or the tongue position angle) as an user input value. However, in the Inventor file linked to the excel tool [17], Horvat chooses to fix the tongue position angle to $50°$ to overcome the difficulties in parametrising the CAD model, effectively making the dimension A dependent on spiral width. Another dimension for which Horvat defines a fixed value is the tongue radius, or the dimension r_z in Equation 3.2. Equation 3.8 represents the changes Horvat did to r_z in the parametrised Inventor CAD file.

$$r_z = \frac{D_2 \times 5}{8} \tag{3.8}$$

Another significant change Horvat made to the fan design in the excel tool is the change in position of the impeller inside the casing. Figure 3-6 shows a comparison of the impeller positions as per Bommes and Horvat. Intuitively in the Bommes methodology the smallest distance between the impeller and the casing should be at the tongue and as reported

by [21, Sec. 4.5, p. 73] (see Figure 3-2 for additional reference) this distance should be between $\frac{1}{4}$ and $\frac{1}{3}$ times the impeller outlet radius as shown in Figure 3-6a with a red dimension line. Where as Horvat modifies the impeller position on the grounds of acoustic improvements [19, Sec. 4.1, p. 33], and moves the closest distance between the impeller and the casing way below the tongue as shown in Figure 3-6b with a red dimension line. However, Horvat retains the value of the distance between the impeller and the tongue to $\frac{1}{4}$ and $\frac{1}{3}$ times the impeller outlet radius as shown with a yellow dimension line in Figure 3-6b. Horvat suggests in [19, Sec. 4.1, p. 33] that though the change in the impeller position is acoustically advantageous, it comes with some losses in the aerodynamic efficiency of the fan.

(a) Bommes. (b) Horvat.
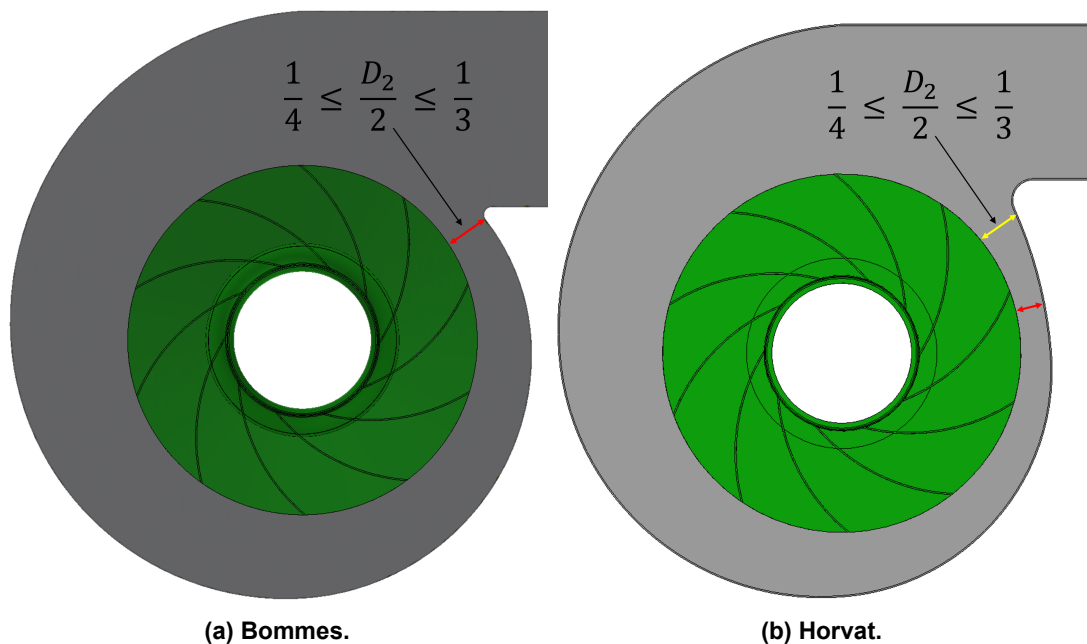
Figure 3-6: Impeller Posoitions Inside the Casing as per Bommes and Horvat.

There have been minor variations and improvements of the excel tool since 2009 and Figure 3-7 shows one of the most recent variation of the tool in English used for academic purposes.

Additional to the set of instructions discussed previously in this section, following are the improvised set of instructions that can be used for efficiently obtaining a good Bommes fan design [24, Sl. 1].

- While adjusting the casing width factor (named as "design factor casing"), the distance between the hub wall and the casing bottom wall must be as small as possible, subjected to the manufacturing and operational limitations.

- The casing spiral width must be approximately double the impeller outlet diameter.

- The fluid velocities at the suction inlet and the casing outlet must be same or must have the least deviation. This can be controlled by changing the casing width factor
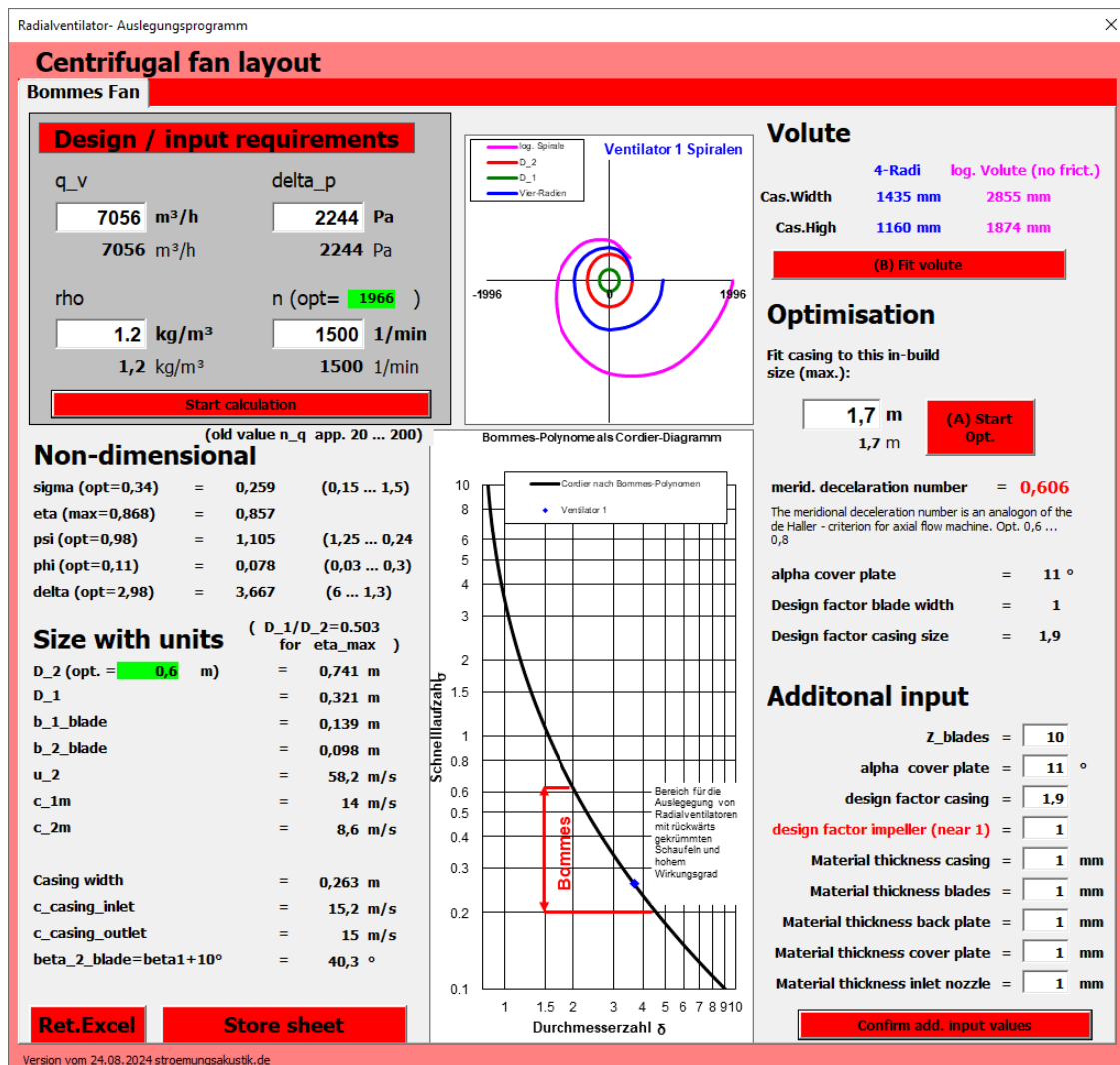
Figure 3-7: Graphical User Interface from One of the Recent Variations of the Excel Tool 2024 [23].

and matching the fluid velocity at the casing outlet to the fluid velocity at the suction inlet. The fluid velocities are displayed under the "Size with units" heading in the recent version of the excel tool as seen in Figure 3-7.

- The fine tuning options, "design factor casing" should preferably be between 2 and 3 and "design factor impeller" should preferably be 1. Appropriate changes must be done only if need be.

Any fine tuning suggested in this section must only be done when the parametrised Inventor file is open parllelly and is refreshed after each modification to make sure that the values do not yield any physically unrealistic designs. For example, it is possible to change the values of the casing and impeller design factors such that the impeller protrudes out of the casing making it physically meaningless. Also, users must note that setting the impeller design factor value anything other than 1 will result in a impeller that no longer adheres to the Bommes methodology.

4 Numerical Simulation and Validation

The excel tool discussed in brief in the previous sections has been in use for academic purposes at the institute of ISAVE at Hochschule Düsseldorf. However, in order to be able to use it for designing fans for research and commercial purposes, it needed to be revalidated. Validating via numerical simulation methods offer significant advantages over prototype testing. But to trust the results obtained from the numerical simulation, the simulation methodology in itself needs to be validated first. To do so, a reference fan - RV722 was simulated and its results were validated against its test bench results. RV722 is a typically high pressure machine in the of Bommes region on the Cordier diagram. It reaches an efficiency of upto 87% with low level of losses and can produce a flow that is optimum from flow separation and efficiency point of view. The term "RV722" stands for Radialventilator (technical term for a centrifugal fan in German) with an impeller outlet diameter (D_2) of 722 mm. The results from the numerical simulation of RV722 were also compared with the results from Ansys CFX for the same CAD model. The CAD model for the reference fan and the frozen rotor simulation results for it from Ansys CFX [25] were available for use at the institute of ISAVE. The test bench results which originally come from [26] are also to be found in [25]. The current chapter will deal with the introduction of the numerical simulation methodology employed and the validation of the same methodology.

Figures 4-1 and 4-2 show the basic dimensions and different CAD views of the reference fan respectively. The linear dimensions in Figure 4-1 are in millimeters (mm).

(a) RV722 Impeller Dimensions.   (b) RV722 Casing Dimensions.

(c) RV722 Impeller Blade Dimensions.   (d) RV722 Spiral Dimensions.
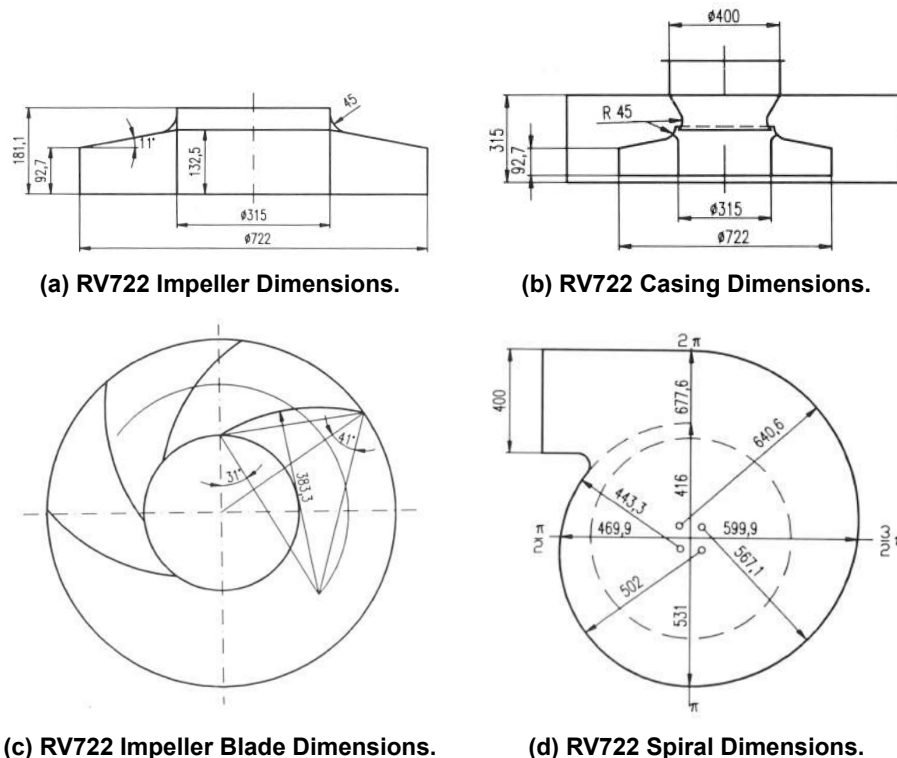
Figure 4-1: Dimensions for RV722 [10, Ch. 3.4, p. 128].

(a) Isometric View.

(b) Cross-sectional Rear View.

(c) Side View.
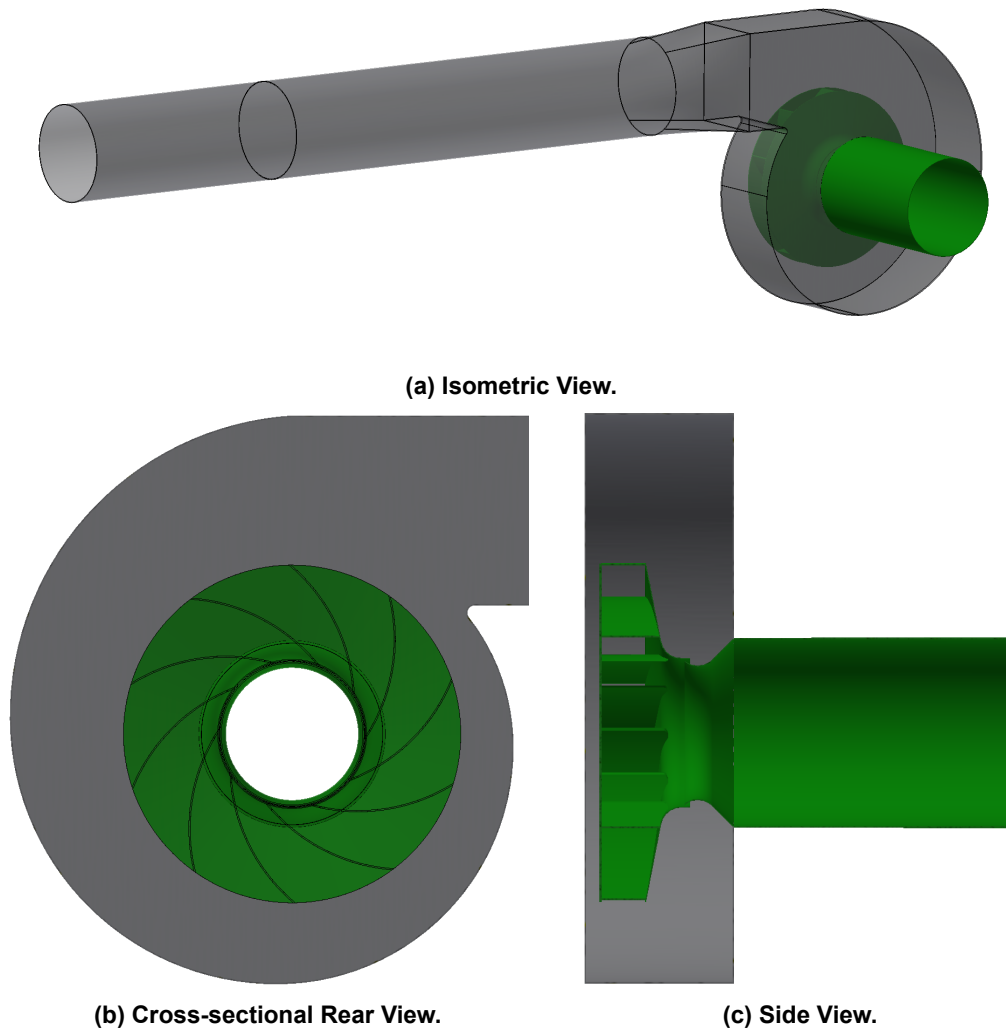
Figure 4-2: CAD Views of RV722.

The reference fan was designed by Strauch and Schneider [27, Sec. 1, p. 1] for a design point with details as shown in Table 4-1. The same fan was then geometrically downsized by a factor of 0.594 to get the reference fan described in Figure 4-1 [27, Sec. 5.4, p. 35]. Table 4-2 shows the physical dimensions obtained by Strauch and Schneider for the main design of the reference fan as well as the corresponding dimensions after downsizing.

The fan design methodology in [27, Sec. 5, p. 29] did not expect the fluid density (ρ) as an input. It instead relied on the equation for ideal gas law as shown in Equation 4.1 to calculate the density.

$$\rho = \frac{p}{R_{specific} \times T} \tag{4.1}$$

Where, ρ = fluid density

p = absolute pressure

$R_{specific}$ = specific gas constant

T = absolute temperature

HSD

ISAVE

Parameters	Value
Volume Flow Rate, $\dot{V}\ [m^3/h]$	30 000
Total Pressure Rise $\Delta P_t\ [Pa]$	5700
Rotational Speed $n\ [RPM]$	1460
Air Temparature $T\ [°C]$	20
Air Static Pressure at inlet $p\ [Pa]$	98 000
Specific Gas Constant of Air $R_{specific}\ [J/kgK]$	287

Table 4-1: Design Point Details for the Main Design of the Reference Fan [27, Sec. 1, p. 1].

	Before Downsizing	After Downsizing
Suction Pipe Diameter, $D_A\ [mm]$	630	400
Impeller Inlet Diameter, $D_1\ [mm]$	530	315
Blade Inlet Angle, β_1	31°	31°
Blade Thickness, $s\ [mm]$	5	—
Blade Inlet Width, $b_1\ [mm]$	232	132.5
Shroud Radius of Curvature, $r_D\ [mm]$	75	45
Impeller Outlet Diameter, $D_2\ [mm]$	1215	722
Blade Outlet Angle, β_2	41°	41°
Number of Blades, z	10	10
Blade Outlet Width, $b_2\ [mm]$	156	92.7
Blade Radius of Curvature $R\ [mm]$	645.9	383.8
$r_1'\ [mm]$	790.8	469.9
$r_2'\ [mm]$	893.5	531
$r_3'\ [mm]$	1009.5	599.9
$r_4'\ [mm]$	1140.3	677.6
$R_1\ [mm]$	747.6	444.3
$R_2\ [mm]$	844.7	502
$R_3\ [mm]$	954.4	567.1
$R_4\ [mm]$	1078.1	640.6

Table 4-2: Physical Dimensions of the Reference Fan Before and After Downsizing [27].

HSD

ISAVE

4.1 Numerical Simulation Methodology

In order to perform CFD analysis, TCFD module of TCAE (version 22.10v2) is used. TCFD expects a 3D fluid domain to be defined using "Patches" which in turn are defined using STL surfaces forming parts of the fan 3D geometry. And to create these STL surfaces, is used. It is also expected to define any internal boundaries or surfaces of interest, where the user would later like to retrieve simulation results, as patches. These internal surfaces divide the entire fluid domain of the geometry under study into various components. Additionally, the inlet and outlet surfaces to the 3D model too are to be defined as patches. In order to create the STL surfaces used to define these patches, the 3D geometries obtained from Inventor are processed in SALOME 9.10.0. Proper care should be taken while creating the STL surfaces, since these surfaces cannot be modified later in TCFD module. Also, a proper and fine meshing of the surfaces before exporting as STL files is advised in order to avoid perplexing errors in TMESH module which uses snappyHexMesh as mesh generator. Once exported as STL files, they can all be stored in a single folder or in seperate folders making up the individual components of the fluid domain.

Once the STL files are ready, they can then be imported within the TMESH module and the patches can be defined by activating them and assigning each patch a function. If the fluid domain is planned to be split into multiple components, then the patches forming each component should be activated in their respective component only. It is important that all the connections between the components are defined. Special care is to be given to the direction of flow of fluid while defining the connections between the components. Later, meshing size for each patch and the desired side of the closed volume to be meshed for each component should be defined.

For meshing purpose, the available fluid domain was divided into the following virtual components:

- Component 1: Suction
- Component 2: Impeller
- Component 3: Casing
- Component 4: Loft
- Component 5: Outlet Pipe
- Component 6: Extra Pipe

As can be seen in Figure 4-3, the Casing is further divided into multiple components. Such a division is not necessary for simulating the fan. However, the division gives an idea about the mesh refinement in different regions of the fan, making it easier to control the mesh cell size in different regions. The mesh components are shown in Figure 4-3.
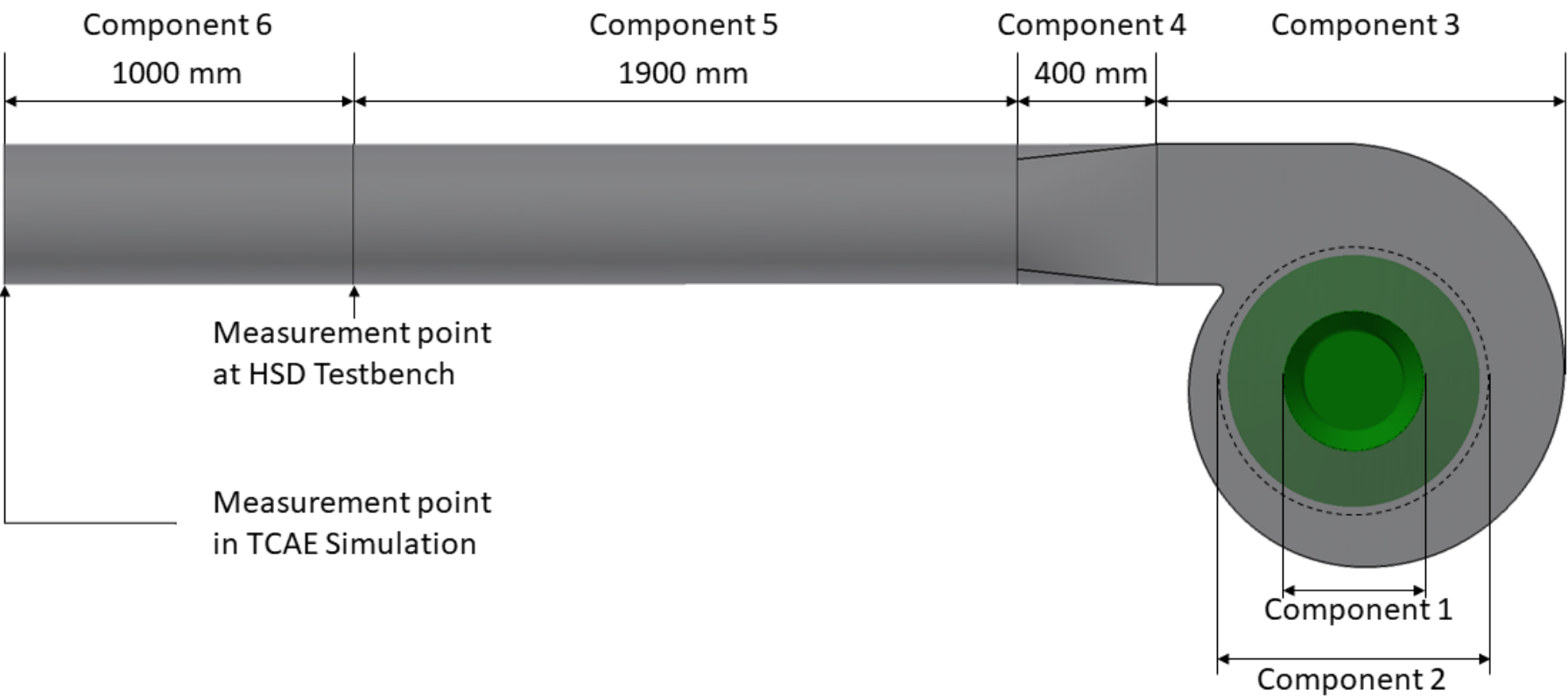
Figure 4-3: Mesh Components for RV722.

And for simulation purpose, the available fluid domain can be visualised into the following three components, wherein suction and casing are static components and impeller is a rotating component. The same components are shown in Figure 4-4. While discussing the simulation results, the Casing will represent the entire domain formed by Casing, Loft, Outlet Pipe, and Extra Pipe.

- Component 1: Suction

- Component 2: Impeller

- Component 3: Casing
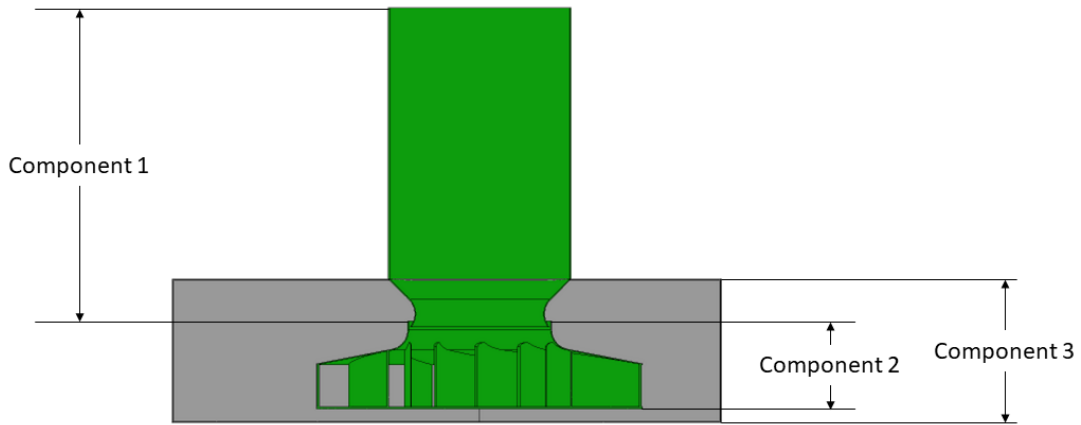
Figure 4-4: Simulation Components for RV722.

Pressure boundary conditions at the inlet and velocity boundary conditions at the outlet were applied in order to mimic the procedure used to obtain the Ansys CFX results in [25]. This will ensure that the comparisons are as fair as possible. However, the number of iterations per operating point was set high to determine the efficiency of TCAE in converging at the solution. The convergence criteria was set to 0.001 of efficiency and the averaging window was set to 100 to get a very good average value. The convergence is decided as per Equation 4.2 [28, Sec. 12.3.3, p. 139].

$$\max_i |\phi_i - \langle\phi\rangle| \leq \xi\langle\phi\rangle \qquad (4.2)$$

Where, ϕ = selected quantity evaluated in i^{th} iteration = Efficiency

ξ = convergence tolerance = 0.001

$\langle\phi\rangle$ = average value of the selected quantity over the last averaging window

4.2 Influence of Mesh Size

To study the influence of mesh size on result accuracy and calculation time, three different variants were simulated in TCAE. At first, a medium sized unstructured hexahedral mesh was employed. Table 4-3 gives an overview of the number of hexahedral mesh elements generated and the time needed for simulation in TCAE.

Component Name	Number of Mesh Elements
Suction	165 846
Impeller	22 167 339
Casing	3 499 627
Loft	34 312
Outlet Pipe	76 462
Extra Pipe	39 932
Total	25 983 518
Mesh time	1.5 hours
Number of cores employed	8
Total simulation time	121.5 hours
Number of core-hours	972
Number of operating points	10
Iterations per operating point	2000

Table 4-3: Mesh and Simulation Details with Respect to Table 4-4 for Variant TS002V0003.

As seen in Table 4-3, impeller has extremely high number of mesh elements compared to other components, though it was supposed to be on the same level of refinement as the rest of the components. Upon further investigation it was found that the blade surfaces were meshed extremely finer than the applied refinement level in the mesh settings. The same can be seen in Figures 4-5 and 4-6. Figure 4-5 shows a cross-sectional view of the meshed fluid components while Figure 4-6 shows a zoomed in view of the impeller blade. This was an unintended effect caused due to the bleeding of the gap refinement applied between the blade surfaces and the Hub and Shroud surfaces as shown in Figure 4-6.
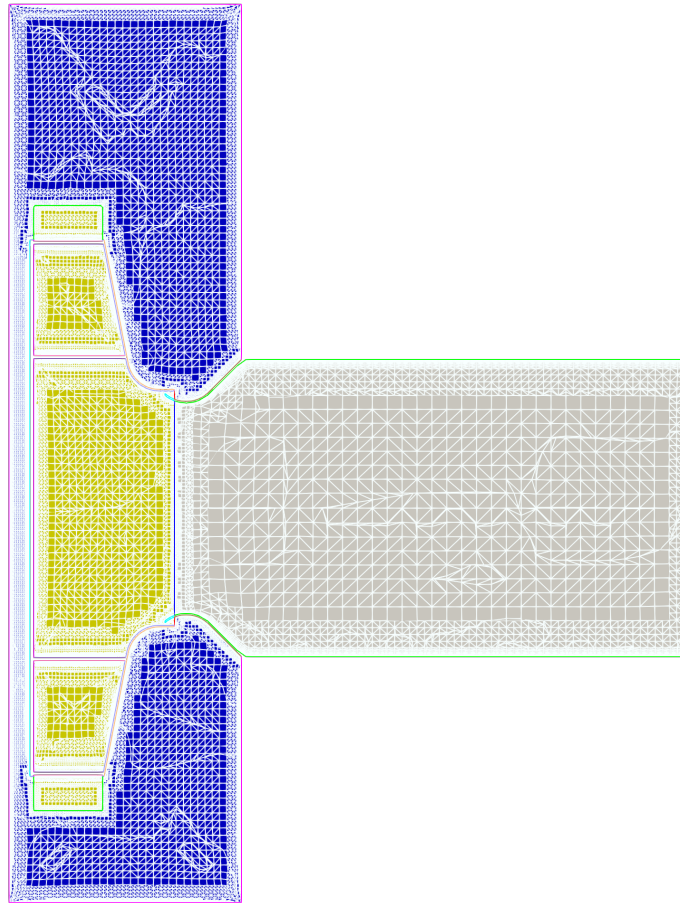
Figure 4-5: Cross-sectional View of Meshed Components of TS002V0003.
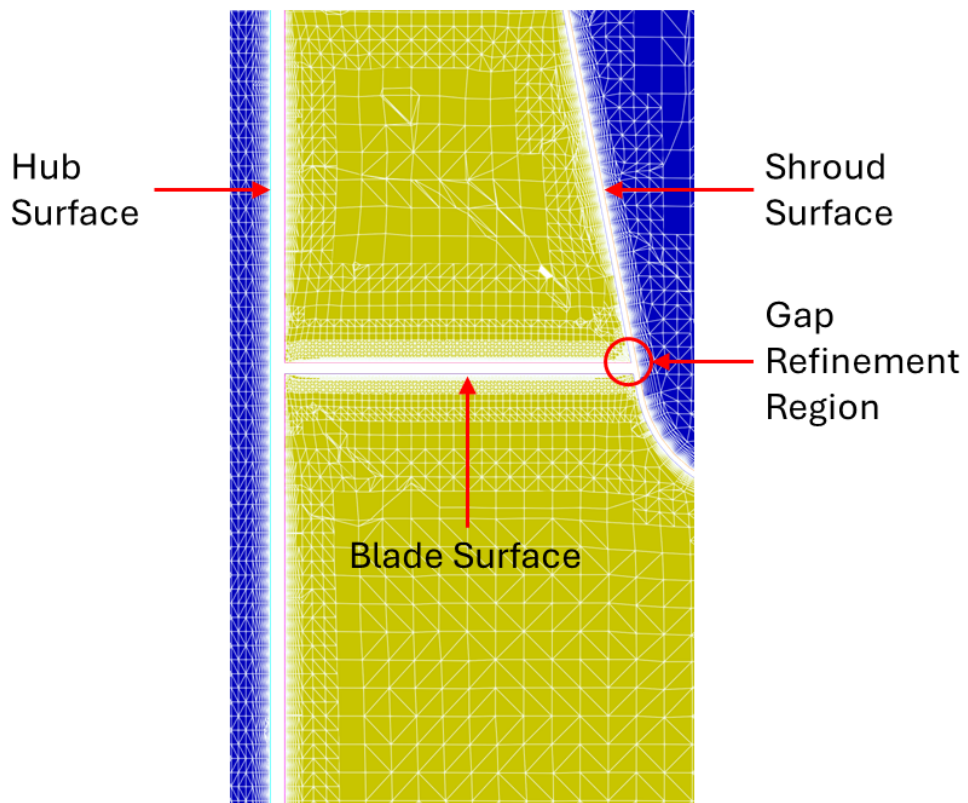
Figure 4-6: Zoomed in View on the Blade Surface of TS002V0003 Showing the Bleeding of Gap Refinement.

The simulation results for fan efficiency and the total pressure rise achieved by the mesh variant TS002V0003 along with a comparison with the results from Ansys CFX and test bench can be seen in Figure 4-7. The numerical simulation methodology discussed in Section 4.1 produces fairly good results in comparison to Ansys CFX. TCAE simulation yielded an efficiency of 83.5% for the optimal point at 1500 RPM, while Ansys CFX predicted the efficiency to be 82.0% for the same model and the fan itself on the test bench achieved an efficiency of 86.5% at the same operating point. TCAE simulation achieved a total pressure rise of 2140 Pa for the same point and Ansys CFX achieved 2085 Pa. While the fan on the test bench achieved 2239 Pa.

(a) Efficiency. (b) Total Pressure Rise.
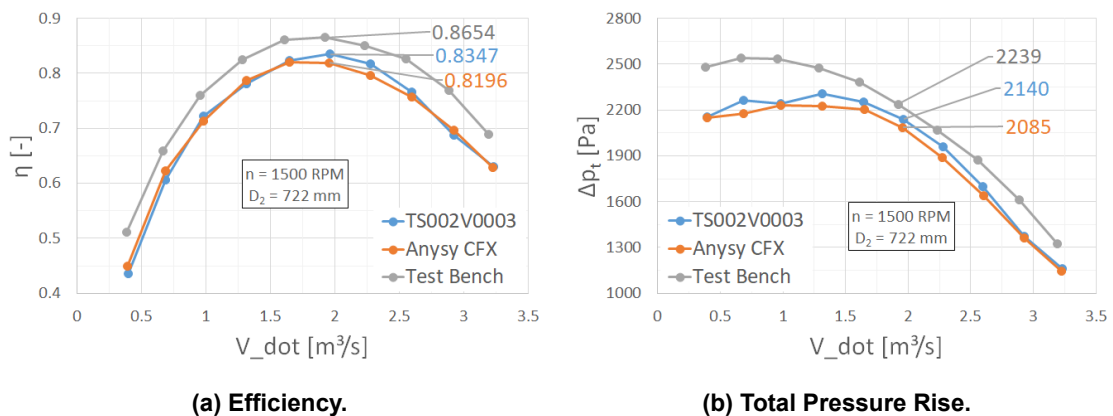
Figure 4-7: Efficiency and Total Pressure Rise for the mesh variant TS002V0003.

Later a much coarser mesh variant, TS002V0004, and a variant with a much balanced and fine mesh size, TS002V0007, were simulated with the same methodology as described in Section 4.1. However, the following changes were applied to the mesh variant TS002V0007, without affecting the validity of the comparison of the mesh variants. The mesh components 4 (Loft) and 5 (Outlet Pipe) as shown in Figure 4-3 were merged with the component 3(Casing). This was done since both these components did not have any geometrical complexities and merging them with the component Casing would save some time during STL surface generation and also while defining the components for numerical simulation. And due to the reduced components the simulation time is expected to reduce as well. But considering the simplicity of the flow in these components, the reduction in simulation time is expected to be very insignificant compared to the total simulation time. The original CAD model made available for the thesis research had a minor error in the way the casing spiral wall was extruded, leading to a reduction of casing width by one times the wall thickness of the casing. The spiral wall was extruded from the outside wall, while it must have been extruded starting from the inside wall. Unfortunately, this error was noticed only after the first two mesh variations were solved and hence the changes were brought into affect only for the variant TS002V0007. The error and the changes applied are illustrated in Figure 4-8. Since the wall thickness of the casing is very small compared to the casing width, this change is not going to bring about any aerodynamic improvements, as will be

seen later during the result discussion.

(a) Before Modifications.

(b) After Modifications.
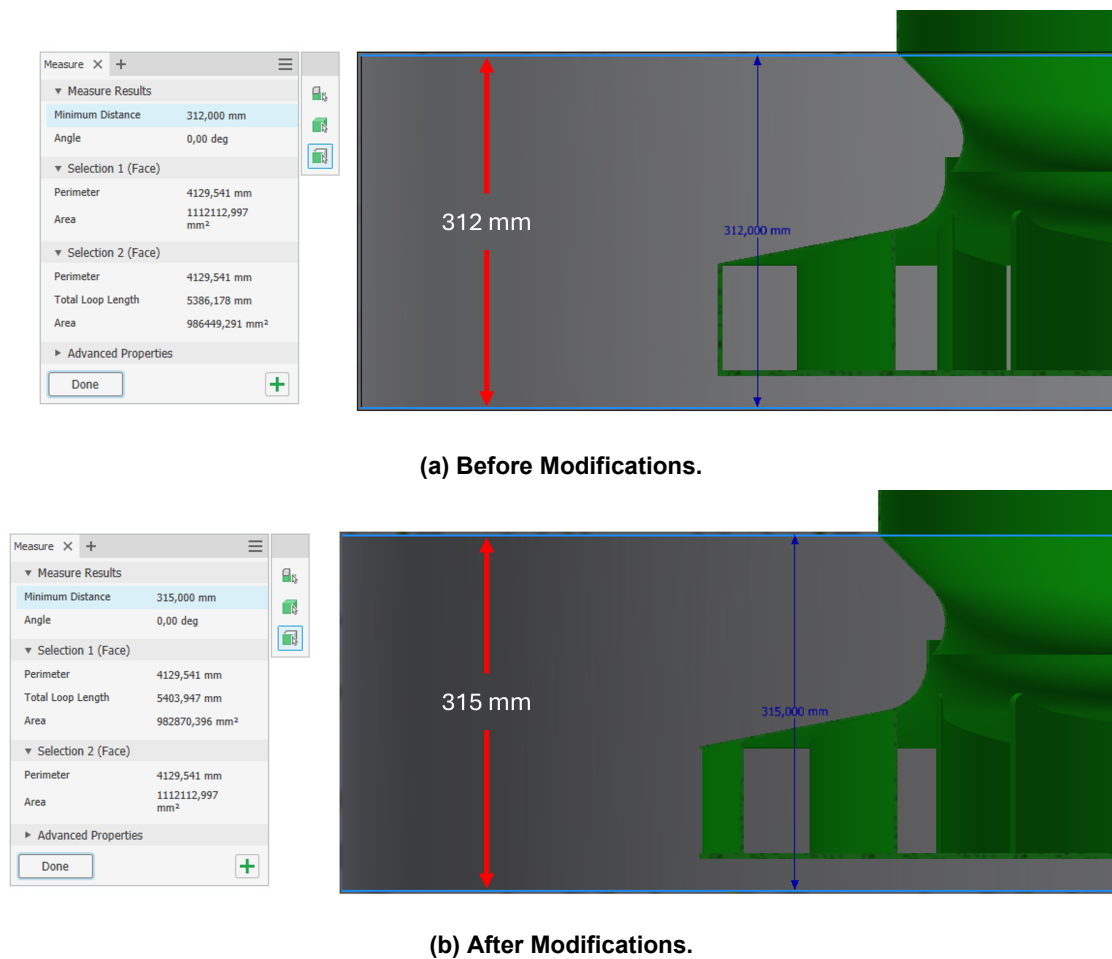
Figure 4-8: Changes to the CAD Model Applied in the Mesh Variant TS002V0007.

Additionally, since the number of mesh elements on the impeller blade surface seemed excessively fine in the mesh variant TS002V0003, the gap refinement that lead to the bleeding effect was skipped in TS002V0004 and TS002V0007, thereby having a better control over the refinement process and the number of hexahedral mesh elements generated.

Figure 4-9 shows a comparison of cross-sectional views of the meshed fluid components in all three mesh variants and Figure 4-10 shows a comparison of mesh refinement on the blade surface. As can be observed in Figure 4-9c, one could argue that the mesh refinement in the Suction and Casing zones seem excessively fine leading to unnecessary increase of total simulation time. The mesh cell size in the suction zone could be increased. However, the casing zone is prone to curls and flow separation and hence it is important to have a finer mesh refinement in this zone to capture any curls or flow separations as precisely as possible. If need be, the mesh components 4 and 5 can be reintroduced and their mesh cell size can be increased. This allows for an independent control of mesh cell size in the casing zone, effectively reducing the total number of mesh cells.

Figure 4-11 shows a comparison of mesh refinement in another critical part of the fan design, i.e.- the recirculation zone between the casing and the impeller. Since this region is

responsible for the recirculation of the fluid from the casing zone back into the impeller zone it plays a vital role in predicting the fan efficiency. Hence it is important to capture the aerodynamics of this region with good accuracy. And a very fine refinement of the mesh at this region is justified. As seen in the Figure 4-11, all three mesh variants achieved good mesh refinement in the region under discussion. However, in the mesh variants TS002V0003 and TS002V0004 the inflation layer seems to grow abruptly. Whereas the mesh variant TS002V0007, Figure 4-10c, was able to avoid this problem and achieved a stable inflation layer. As a rule of thumb, if the y+ value is around 1, a minimum of 10 inflation layers are suggested. And in all the simulations in this thesis, an inflation layer with 10 layers is used. This satisfies the bare minimum and can be increased or decreased based on the y+ values on the areas of interest.

A comparison of number of hexahedral mesh elements generated in each component for all three mesh variants and the number of cores employed as well as the amount of time required to simulate them can be seen in Table 4-5. The components "Loft" and "Outlet Pipe" for the mesh variant TS002V0007 do not have any entries for the reasons discussed earlier and hence have been represented by "—".

	Workstation 1	Workstation 2
Processor	Intel	Intel
Model	Xenon	Xenon
Max Clock Speed	3.5GHz	2.60GHz
Total Number of Logical Processors	8	28
RAM	64 GB	128 GB
Operating System	Windows 10 Education	Windows 10 Education
System Type	64-Bit	64-Bit
Varinats Simulated	TS002V0003 TS002V0004	TS002V0007 TS003V0002

Table 4-4: Specifications of the Workstations Employed for Numerical Simulations.

The simulation time mentioned in Tables 4-3 and 4-5 are to be used as a rough approximation and is not to be considered as simulation speed benchmarking times. Due to the restricted nature of time available for this thesis, different mesh variants were simulated on different workstations parallelly. Additionally, the times mentioned in the Tables 4-3 and 4-5 do not include the time required for the STL surface generation in SALOME, which is an intermediate step between the creation of the fan 3D geometry in Inventor and fan simulation in TCAE (or OpenFOAM). Table 4-4 gives the specifications of the workstations employed and the mesh variants solved on them.

(a) TS002V0003.　　　　　(b) TS002V0004.　　　　　(c) TS002V0007.
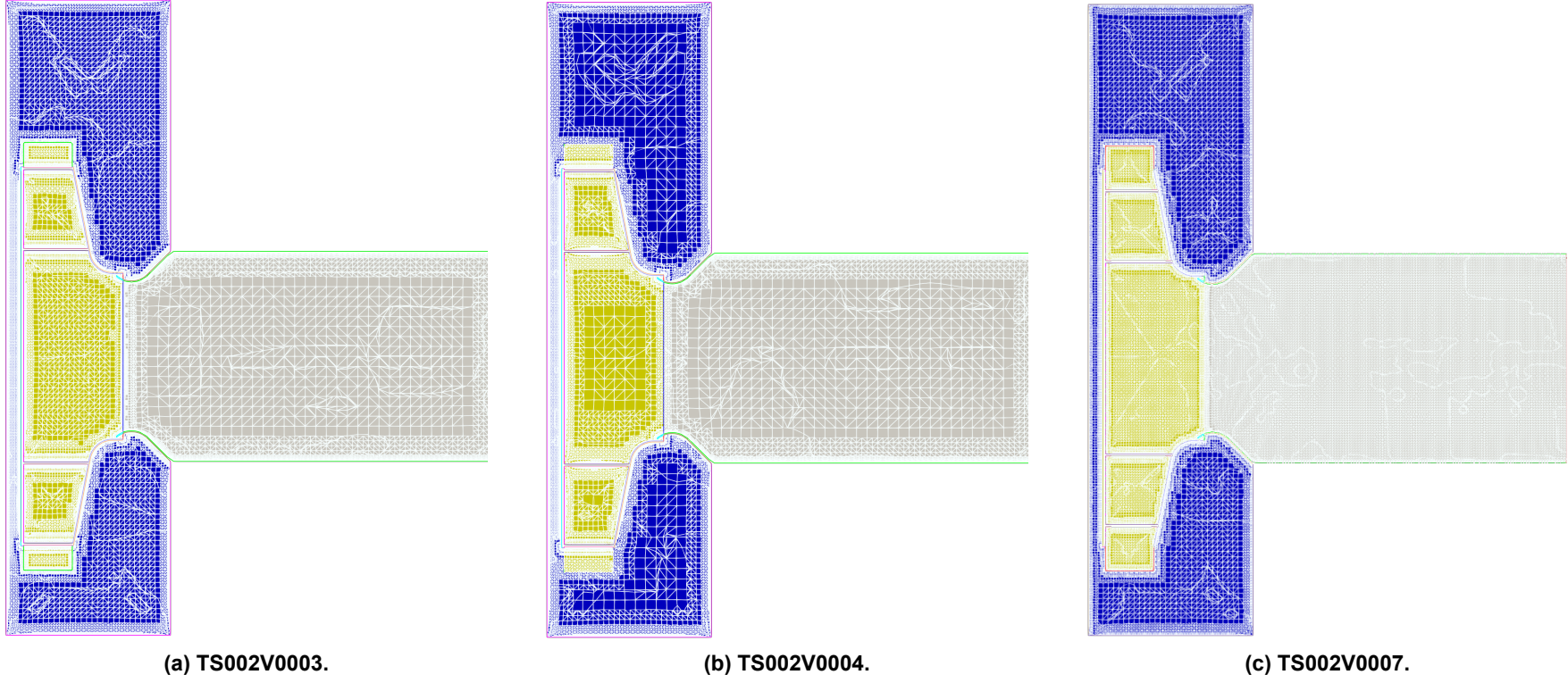
Figure 4-9: Cross-sectional Views of Fluid Components Showing a Comparison of Mesh Refinement.

(a) TS002V0003.

(b) TS002V0004.
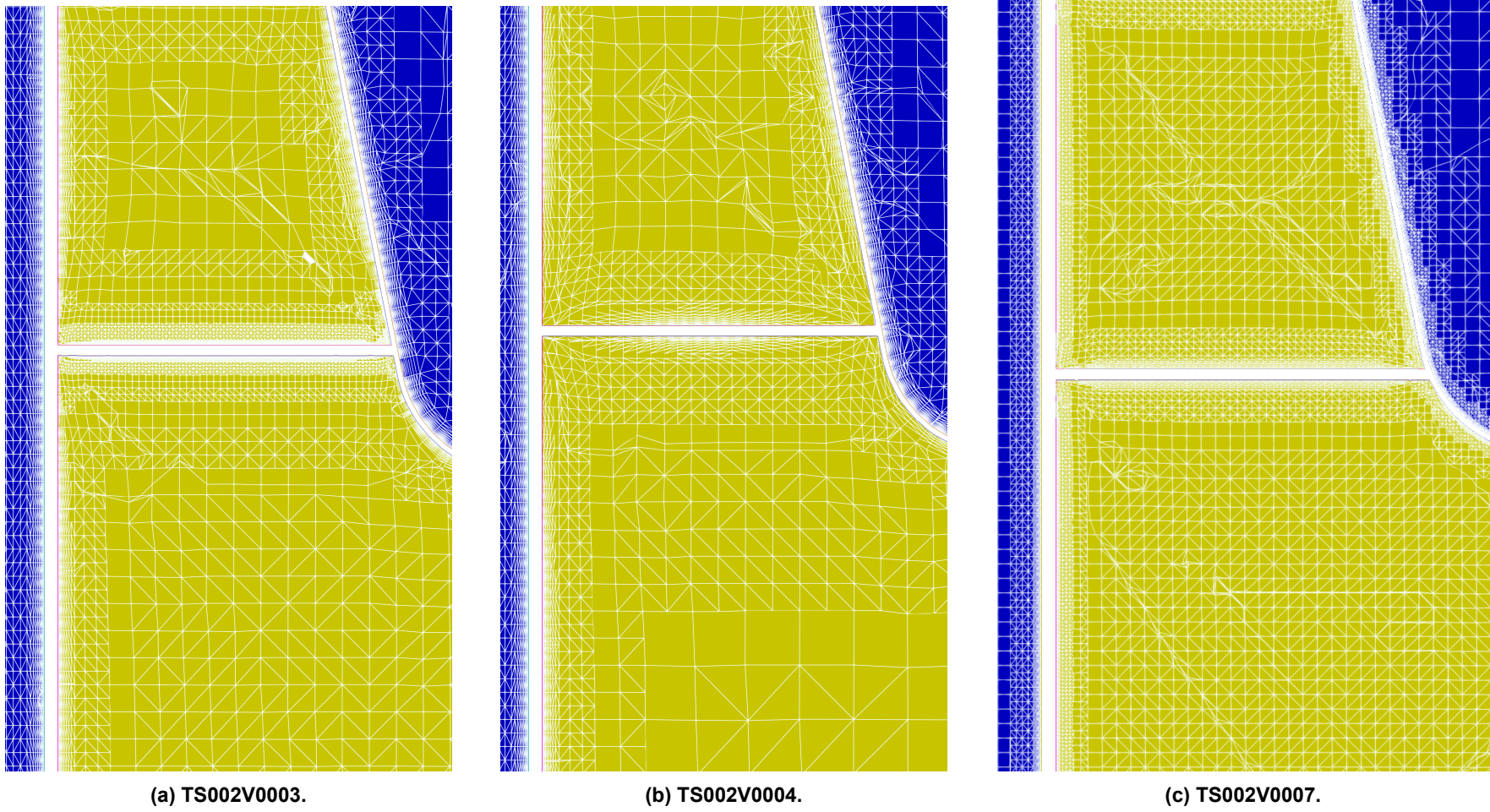
(c) TS002V0007.

Figure 4-10: Zoomed in Views Showing a Comparison of Mesh Refinement on Impeller Blade Surfaces.

(a) TS002V0003.   (b) TS002V0004.   (c) TS002V0007.
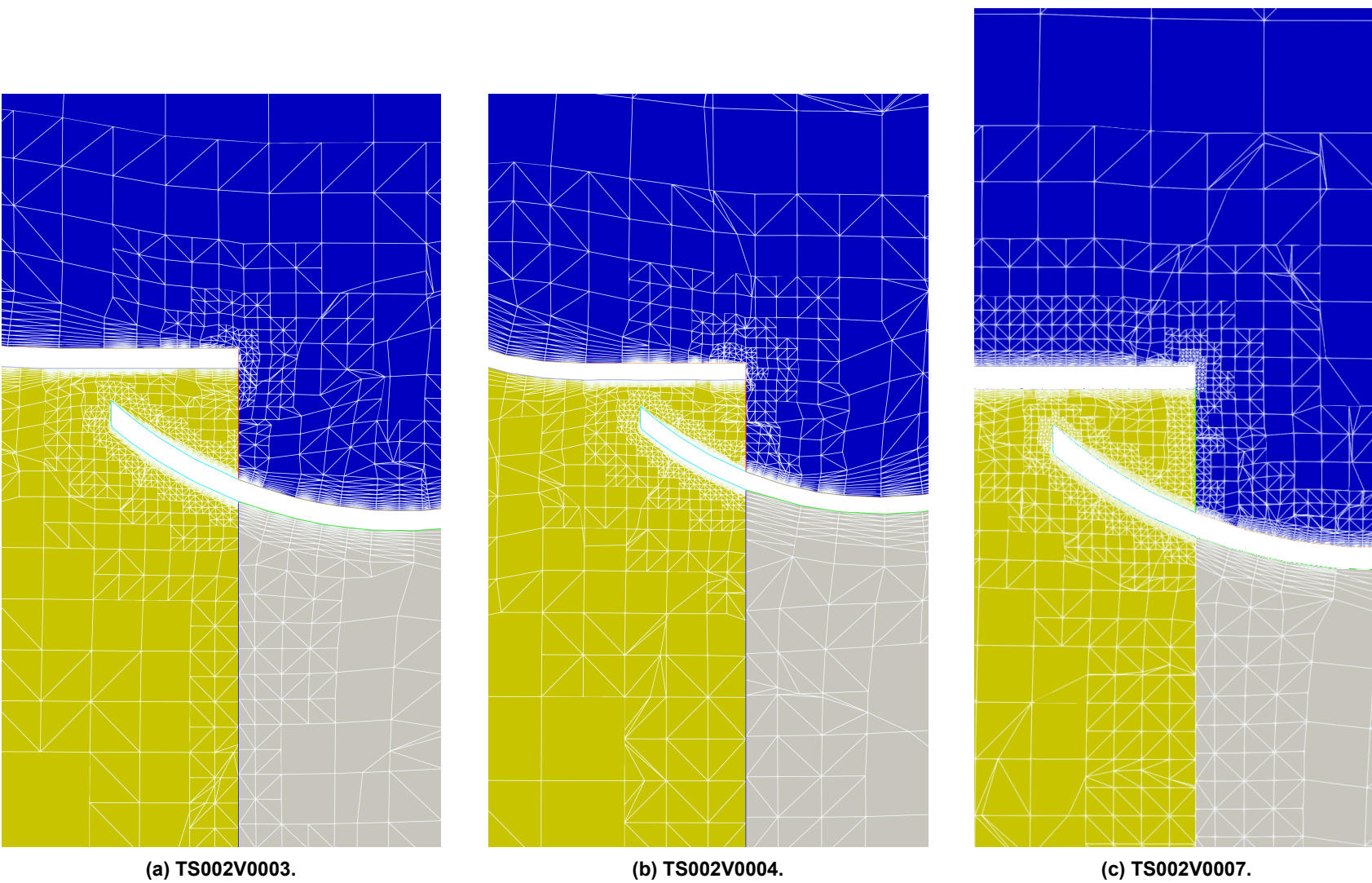
Figure 4-11: Zoomed in Views Showing a Comparison of Mesh Refinement on Recirculation Zone.

	Mesh Refinement and Simulation Time Details		
	TS002V0003	**TS002V0004**	**TS002V0007**
Suction	165 846	121 395	910 541
Impeller	22 167 339	2 375 872	9 622 997
Casing	3 499 627	3 108 833	10 997 665
Loft	34 312	61 889	—
Outlet Pipe	76 462	76 462	—
Extra Pipe	39 932	39 932	611 086
Total	25 983 518	5 784 383	22 142 289
Number of cores employed	8	8	24
Mesh time	1.5 hours	0.5 hours	0.75 hours
Total simulation time	121.5 hours	32.5 hours	55.5 hours
Number of core-hours	972	260	1332
Number of operating points	10	10	10
Iterations per operating point	2000	2000	1000

Table 4-5: Mesh Refinement and Simulation Time Details with Respect to Table 4-4 for All Three Mesh Variants.

The three mesh variants, TS002V0003, TS002V0004, and TS002V0007, were simulated at 1500 RPM for the operating points listed in Table 4-6. The numerical simulation results for fan efficiency and total pressure rise of all three mesh variants in comparison with the results from the test bench and Ansys CFX as available in [25] can be seen in Figure 4-12 shows. Again, both TS002V0004 and TS002V0007 predict the results with a good accuracy just like in the variant TS002V0003. Especially at the design point, TCAE seems to predict better than Ansys CFX. But the fact that the simulation in Ansys CFX was done with a much coarser mesh and with lesser iterations per operating point might contribute to the deviations. However, it is safe to conclude that the simulation methodology used in this thesis research is reliable and can predict results with a good accuracy.

Operating Point Number	Mass Flowrate at Outlet [kg/s]	Corresponding Volume Flowrate [m³/s]
1	0.47	0.4
2	0.82	0.68
3	1.18	0.98
4	1.58	1.32
5	1.98	1.65
6	2.35	1.96
7	2.73	2.28
8	3.12	2.6
9	3.51	2.93
10	3.87	3.23

Table 4-6: Operating Points at which All Three Mesh Variants were Simulated.

(a) Efficiency - TS002V0003.

(b) Total Pressure Rise - TS002V0003.

(c) Efficiency - TS002V0004.

(d) Total Pressure Rise - TS002V0004.

(e) Efficiency - TS002V0007.

(f) Total Pressure Rise - TS002V0007.
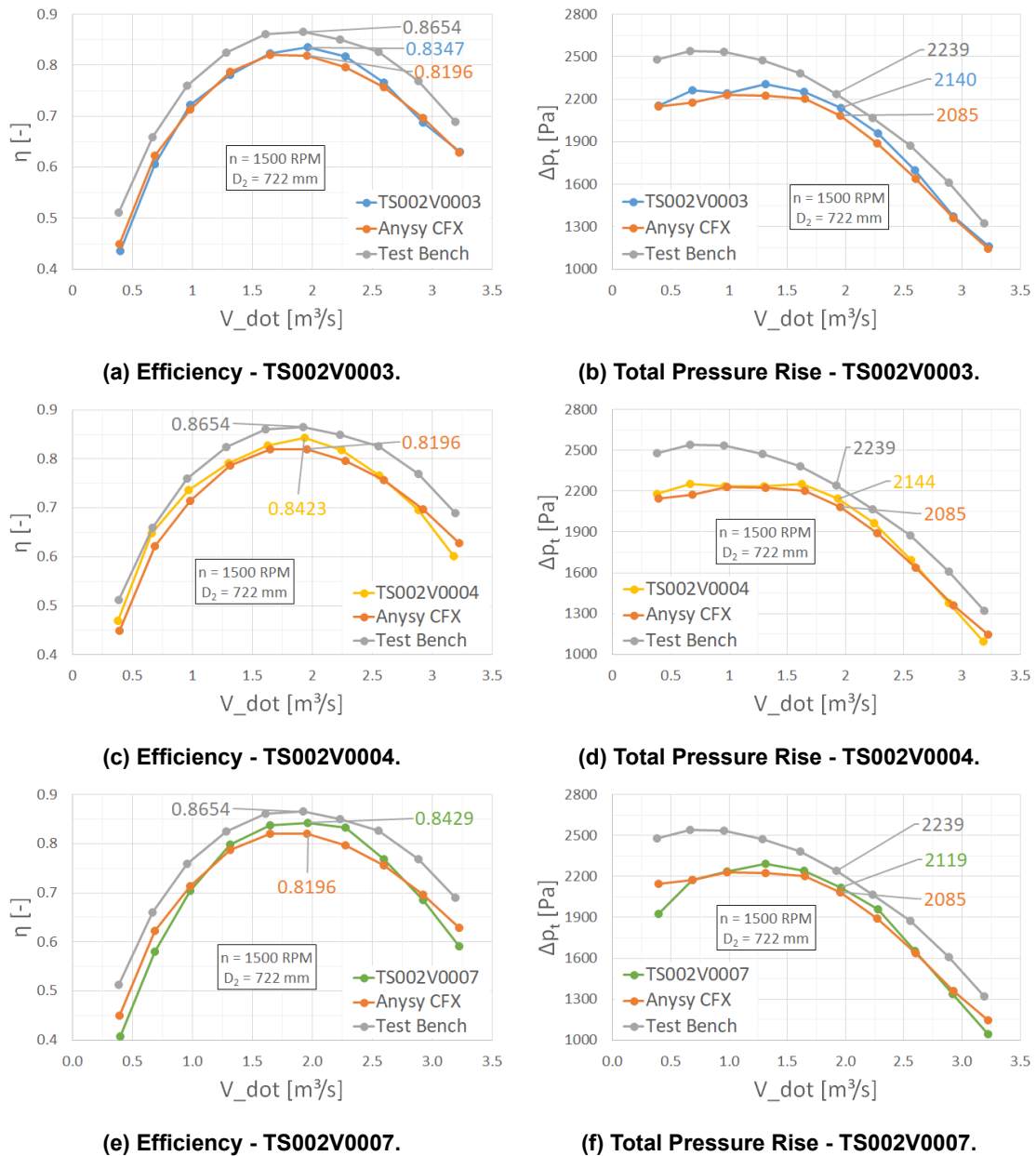
Figure 4-12: Efficiency and Total Pressure Rise for All Three Mesh Variants in Comparison to those from Ansys CFX and Test Bench.

A comparison of efficiency and total pressure rise for just the three mesh variants can be seen in Figure 4-13. The coarse mesh variant TS002V0004 is able to produce pretty much the same results as the finely and more uniformly distributed mesh variant TS002V0007. It would be of interest in the future to further increase the mesh cell size and study the changes in efficiency and total pressure rise predictions by TCAE.
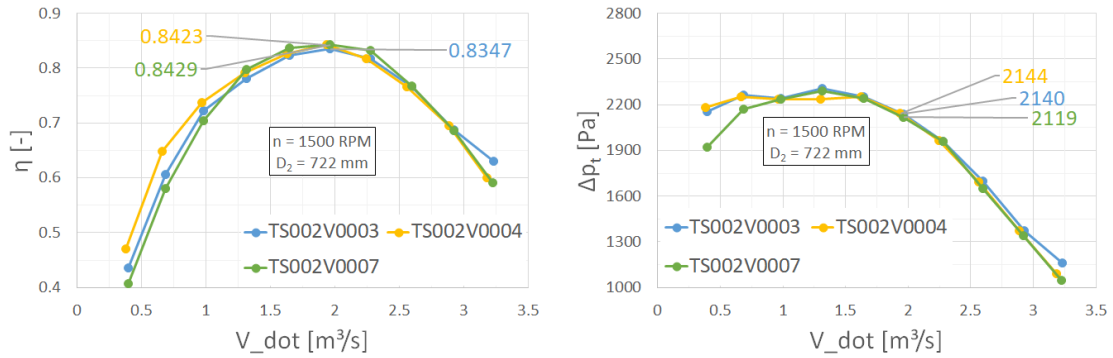
(a) Comparison of Efficiency for the Three Mesh Variants.

(b) Comparison of Total Pressure Rise for the Three Mesh Variants.

Figure 4-13: Comparison of Efficiency and Total Pressure Rise for All Three Mesh Variants.

Figure 4-14 shows us the velocity profiles for all three mesh variants in surface line integral convolution (Surface-LIC) format. The velocity profiles are on the impeller mid cross-section and at the optimal point, i.e.- point 6 in Table 4-6. Additionally, the vector fields within the stationary suction and the casing zones depict absolute velocities, while the vector field within the rotating impeller zone is depicting the relative velocities. Further, Figure 4-15 shows zoomed-in views of the Surface-LIC for velocity profiles in the impeller zone on the impeller mid cross-section and at the optimal point.

The simulation methodology discussed in Section 4.1 seems to predict the CFD results with a good accuracy even with coarsely meshed fluid components, as seen in the mesh variant TS002V0004. In TS002V0003 and TS002V0007, both the mesh variants have roughly the same total number of hexahedral mesh cells and they both need high number of core hours as observed in Table 4-5. However, the way the mesh elements are distributed on the blade surface is very different. It is of interest to evaluate the effect of this varied blade surface mesh refinement in prediction of wall bounded turbulent flows. In the current thesis research, all the numerical simulations were carried out with $k - \omega\ SST$ turbulence model. As per literature [29–31], it is recommended to have a y+ value of $y+ \leq 1$ to successfully predict wall bounded turbulent flows. But in order to achieve such low y+ values, one would need infinitesimally fine mesh refinement on the blade surfaces, as achieved in the mesh variant TS002V0003. Further the same literature also dictate that if it is not possible to have a y+ value of $y+ \leq 1$, a value of $1 \leq y+ \leq 30$ should be sufficient. The y+ values achieved at optimal points in all three mesh variants are as listed in Table 4-7 and are also visually represented in Figure 4-16 .

(a) TS002V0003.   **(b) TS002V0004.**   **(c) TS002V0007.**
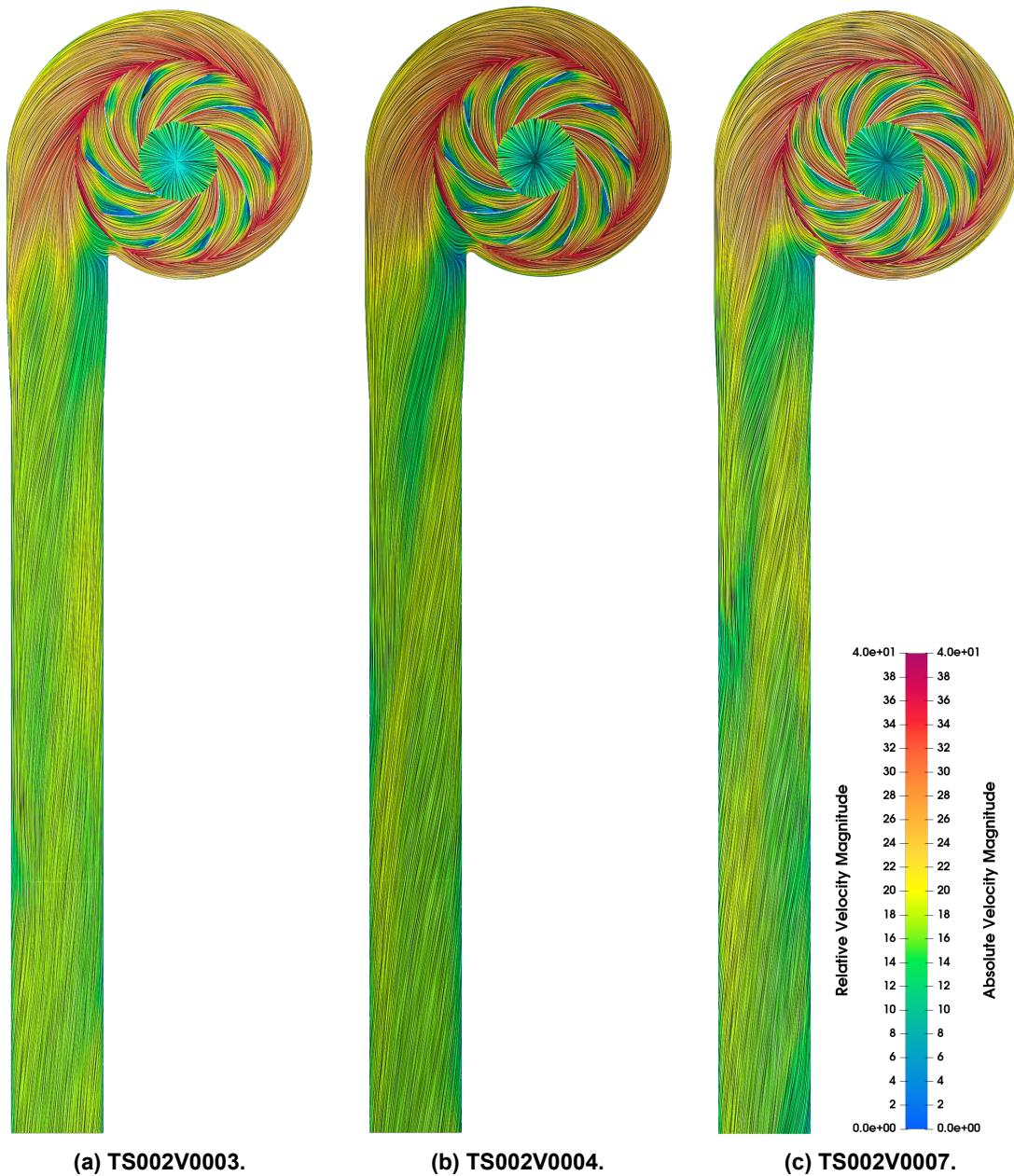
Figure 4-14: Velocity Surface-LICs for Optimal Points of All Three Mesh Variants at Impeller Mid Cross-Sectiont; D_2 = 722; n = 1500 RPM; $\dot{V}$ = 1.32 $m^3 s^{-1}$.

Relative Velocity Magnitude

0.0e+00 2 4 6 8 10 12 14 16 18 20 22 24 26 28 30 32 34 36 38 4.0e+01

Absolute Velocity Magnitude

0.0e+00 2 4 6 8 10 12 14 16 18 20 22 24 26 28 30 32 34 36 38 4.0e+01

(a) TS002V0003.

(b) TS002V0004.

(c) TS002V0007.
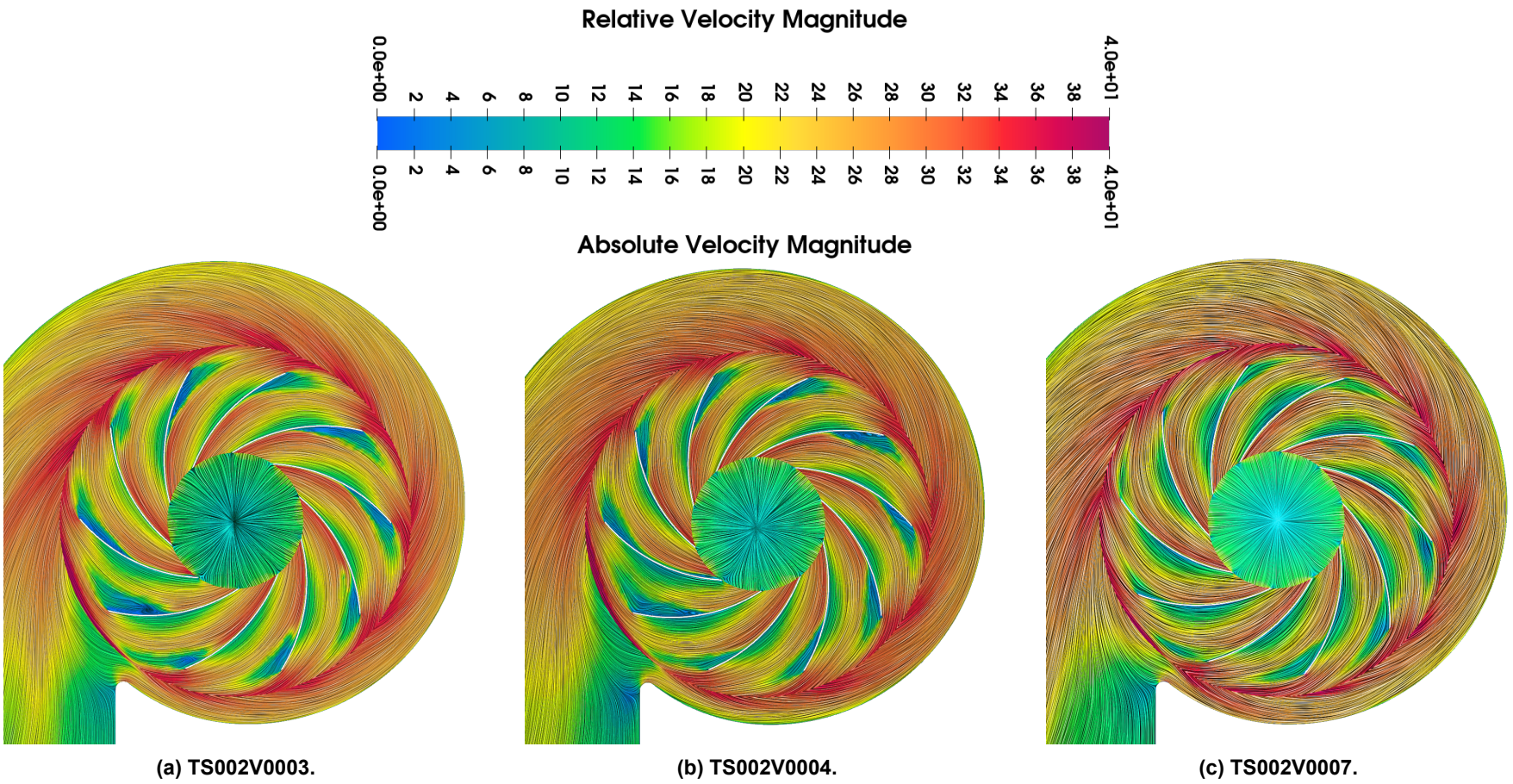
Figure 4-15: Zoomed-in Views of Impeller Zones Showing Velocity Surface-LICs for Optimal Points of All Three Mesh Variants at Impeller Mid Cross-Section; D_2 = 722 mm; n = 1500 RPM; $\dot{V}$ = 1.96 $m^3 s^{-1}$.

	Pressure Side			Suction Side		
	Min y+	**Max y+**	**Average y+**	**Min y+**	**Max y+**	**Average y+**
TS002V0003	49.7113×10^{-6}	117.668	0.3516	5.3856×10^{-6}	141.057	0.2781
TS002V0004	11.1015×10^{-3}	276.751	10.3506	$2.686\,03 \times 10^{-3}$	406.224	8.6709
TS002V0007	4.8137×10^{-3}	93.705	5.1140	$4.842\,50 \times 10^{-3}$	251.257	3.6933

Table 4-7: Y+ Values at Optimal Point for All Three Mesh Variants.

	Pressure Side			Suction Side		
	Min y+	**Max y+**	**Average y+**	**Min y+**	**Max y+**	**Average y+**
n = 1000 RPM	1.3133×10^{-3}	58.953	2.0082	2.3260×10^{-3}	181.264	2.7231
n = 1500 RPM	4.8137×10^{-3}	93.705	5.1140	4.8425×10^{-3}	251.257	3.6933
n = 2400 RPM	34.5645×10^{-3}	154.613	9.5805	7.9187×10^{-3}	388.906	7.0872

Table 4-8: Y+ Values at Optimal Points for TS002V0007 at Different Impeller Speeds.

(a) TS002V0003.

(b) TS002V0004.

(c) TS002V0007.

yPlus
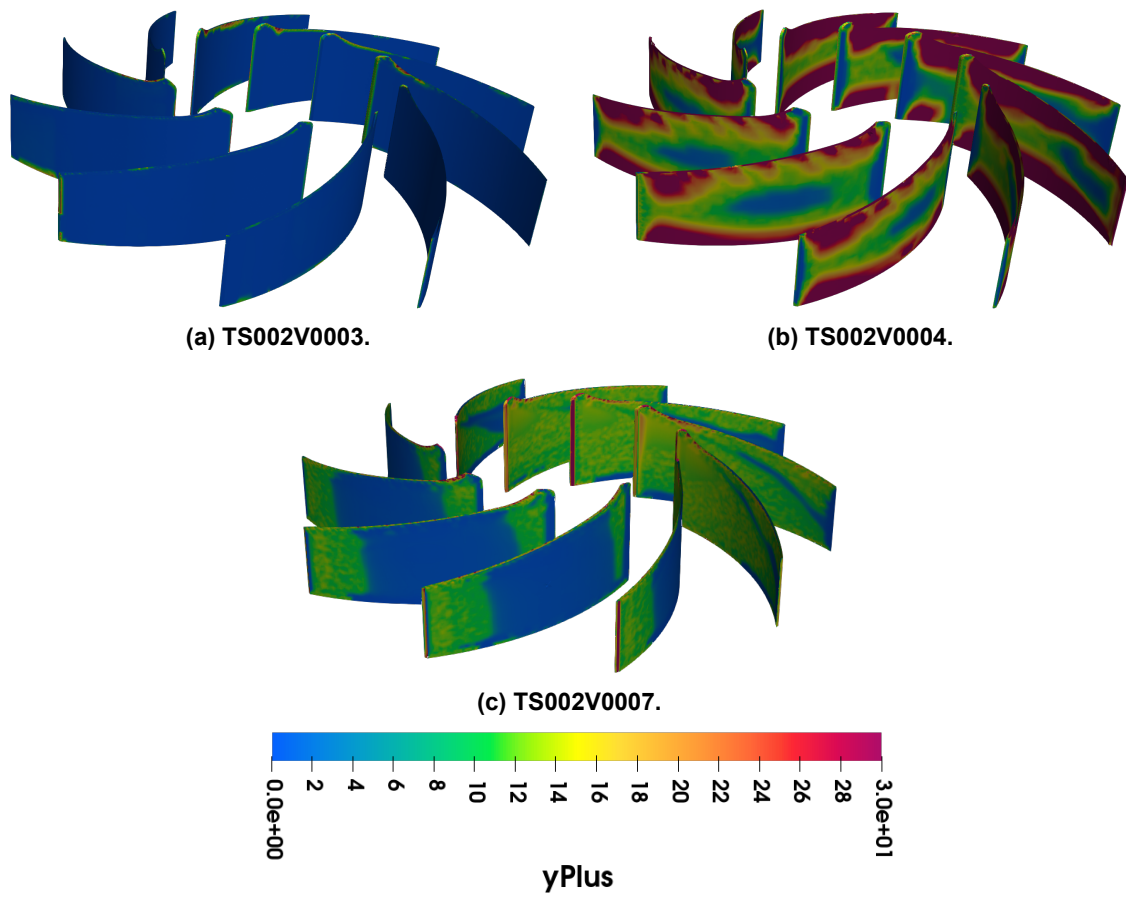
Figure 4-16: Visual Representation of Y+ Values at Optimal Point for All Three Mesh Variants; D_2 = 722; n = 1500 RPM; $\dot{V}$ = 1.32 $m^3 s^{-1}$.

4.3 Influence of Impeller Speed

Since the mesh variant TS002V0007 had satisfactory inflation layer thickness and predicted fan performance with good accuracy for the conditions stated in Table 4-5, it was further simulated for the operating points listed in Table 4-6 at two additional impeller speeds - 1000 RPM and 2400 RPM. The change in impeller speed influences the fan Reynolds number and can be calculated as per Phelan et al. (1979, p671) [32, Sec. 2,p. 671] using Equation 4.3. The resulting fan Reynolds numbers are as listed in Table 4-9.

$$Re_{fan} = \frac{\pi \rho N D_2{}^2}{\mu} \tag{4.3}$$

Where, ρ = density of the fluid $[kg\ m^{-3}]$
N = impeller speed $[RPM]$
D_2 = impeller outer diameter $[m]$
μ = dynamic viscosity of the fluid $[Pa\ s]$

Impeller Speed N [RPM]	Fan Reynolds Number Re_{fan}
1000	2.52×10^6
1500	3.78×10^6
2400	6.05×10^6

Table 4-9: Fan Reynolds Numbers for Different Impeller Speeds of TS002V0007.

Figure 4-17 shows a comparison of fan efficiency and pressure rise as achieved by the variant TS002V0007 for all three impeller speeds. And as quite expected, the optimum efficiency point shifts to the left, i.e.- the optimum efficiency occurs at a lower volume flowrate, for a lower impeller speed and it shifts right, i.e.- the optimum efficiency occurs at a higher volume flowrate, for a higher impeller speed. However, the value of the optimum efficiency at all impeller speeds remains pretty much the same, emphasising the fact that its the same fan with the same performance characteristics. This can be better illustrated by plotting the dimensionless characteristics graphs for the fan at different impeller speeds, as done in Figure 4-18. It is to be noted that the graph for efficiency at an impeller speed of 1000 RPM is missing the last two operating points as evident from Figure 4-17a. The reason for omitting these two points is discussed in Section 4.5.

(a) Efficiency.

(b) Total Pressure Rise.
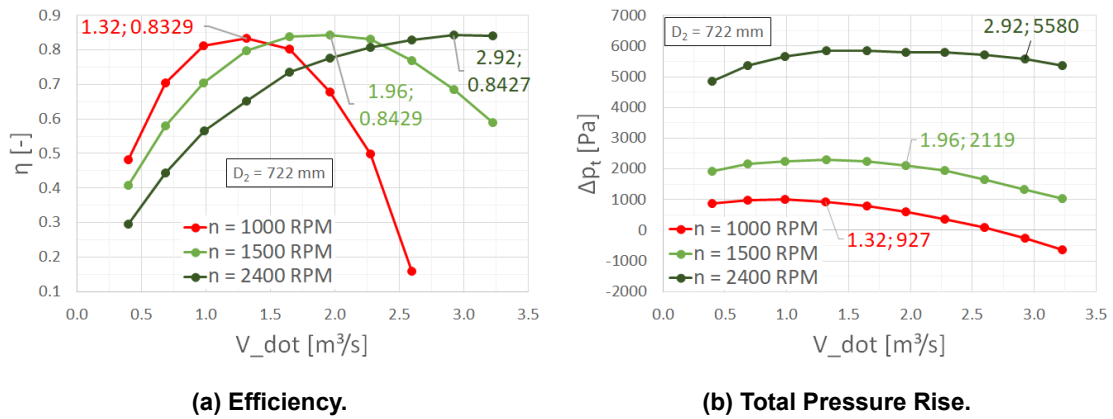
Figure 4-17: Efficiency and Total Pressure Rise for TS002V0007 at Different Impeller Speeds.

Figure 4-18 shows the dimensionless characteristics for the reference fan RV722 with the results from the mesh variant TS002V0007 simulated at different impeller speeds. The characteristic curves for each impeller speed are of different lengths because the characteristic curves were plotted to operating points with same volume flowrate instead of same flow coefficient (ϕ) values. Normally, it is a common practice to decide fixed ϕ values for which the volume flowrate values corresponding to different impeller speeds are calculated and the fan is simulated at these flowrates. But in the current thesis research, since the simulation of the entire fan curve with ten operating points was taking considerably long time, it was decided to plot the dimensionless characteristic curves for the available flowrate points to save time and resources. Nevertheless, the current dimensionless curves are good enough to show that the curves overlap to a very good degree proving the accuracy and reliability of the numerical simulations for varied operating speeds. Table 4-8 and Figure 4-19 show the y+ values for the mesh variant TS002V0007 at different impeller speed.

(a) η v/s ϕ.

(b) ψ v/s ϕ.
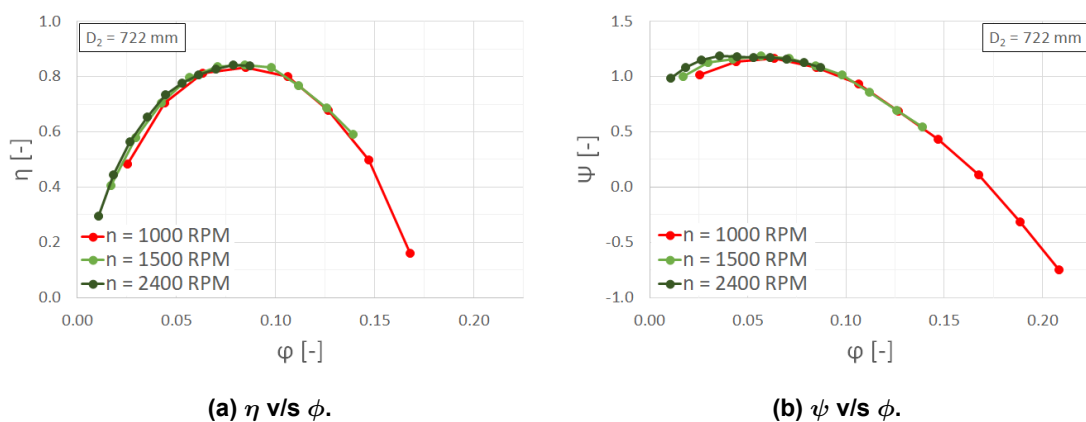
Figure 4-18: Dimensionless Characteristics Curves for the Reference Fan RV722 Based on the Results from TS002V0007.

Figure 4-20 shows a comparison of velocity Surface-LICs for all three impeller speeds of TS002V0007 at their respective optimal points and at impeller mid cross-section. The

(a) n = 1000 RPM; $\dot{V}$ = 1.32 $m^3 s^{-1}$.

(b) n = 1500 RPM; $\dot{V}$ = 1.96 $m^3 s^{-1}$.

(c) n = 2400 RPM; $\dot{V}$ = 2.92 $m^3 s^{-1}$.

yPlus
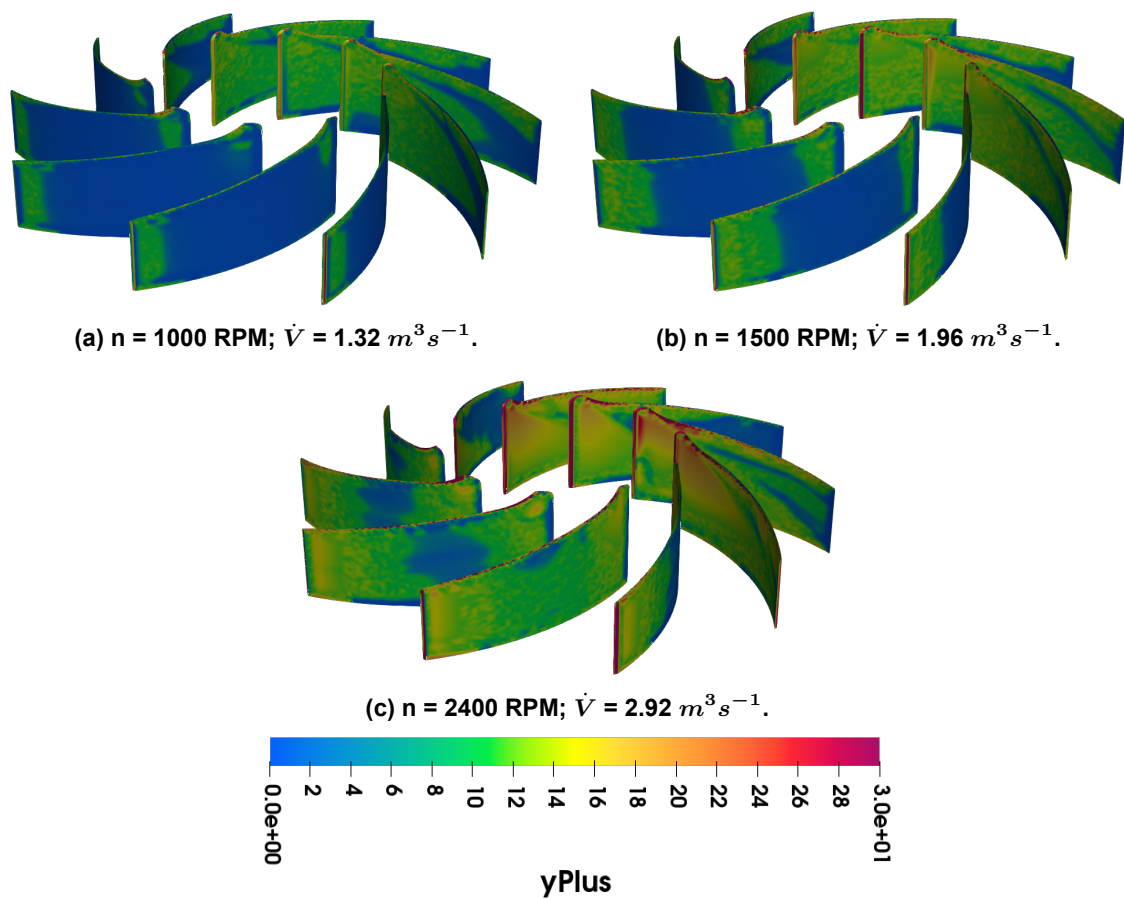
Figure 4-19: Visual Representation of Y+ Values at Optimal Points for TS002V0007 at Different Impeller Speeds.

optimal volume flowrate points for TS002V0007 (RV722) as evident from Figure 4-17 are 1.32 m^3/s, 1.96 m^3/s, and 2.92 m^3/s at 1000 RPM, 1500 RPM, and 2400 RPM respectively. Figure 4-21 shows zoomed in views of the impeller zones for the same three cases.

(a) n = 1000 RPM; $\dot{V}$ = 1.32 $m^3 s^{-1}$.

(b) n = 1500 RPM; $\dot{V}$ = 1.96 $m^3 s^{-1}$.

(c) n = 2400 RPM; $\dot{V}$ = 2.92 $m^3 s^{-1}$.
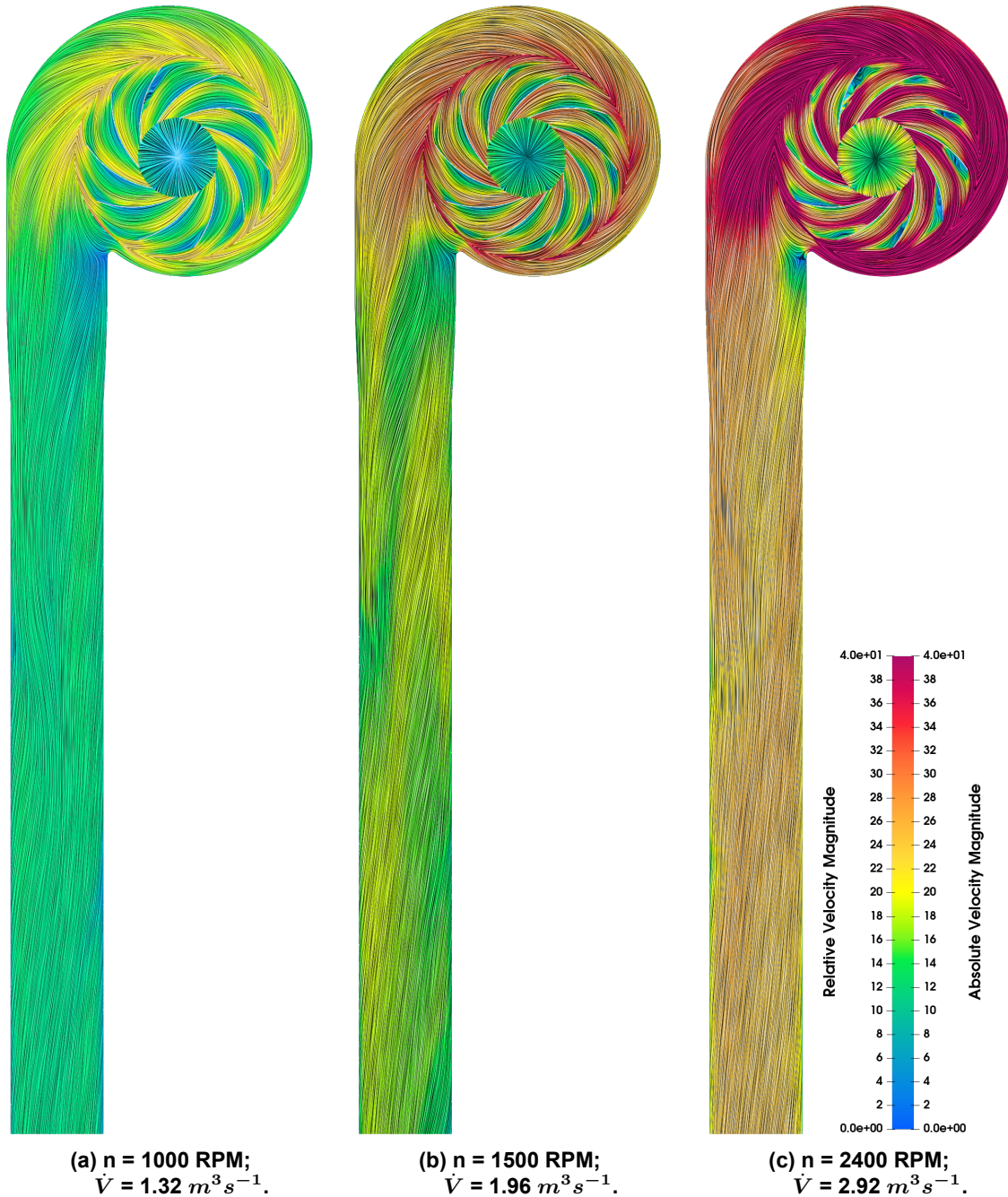
Figure 4-20: Velocity Surface-LICs for Optimal Points of TS002V0007 (RV722) at Different Impeller Speeds and at Impeller Mid Cross-Section.

Relative Velocity Magnitude

Absolute Velocity Magnitude

(a) n = 1000 RPM; $\dot{V}$ = 1.32 $m^3 s^{-1}$.

(b) n = 1500 RPM; $\dot{V}$ = 1.96 $m^3 s^{-1}$.

(c) n = 2400 RPM; $\dot{V}$ = 2.92 $m^3 s^{-1}$.
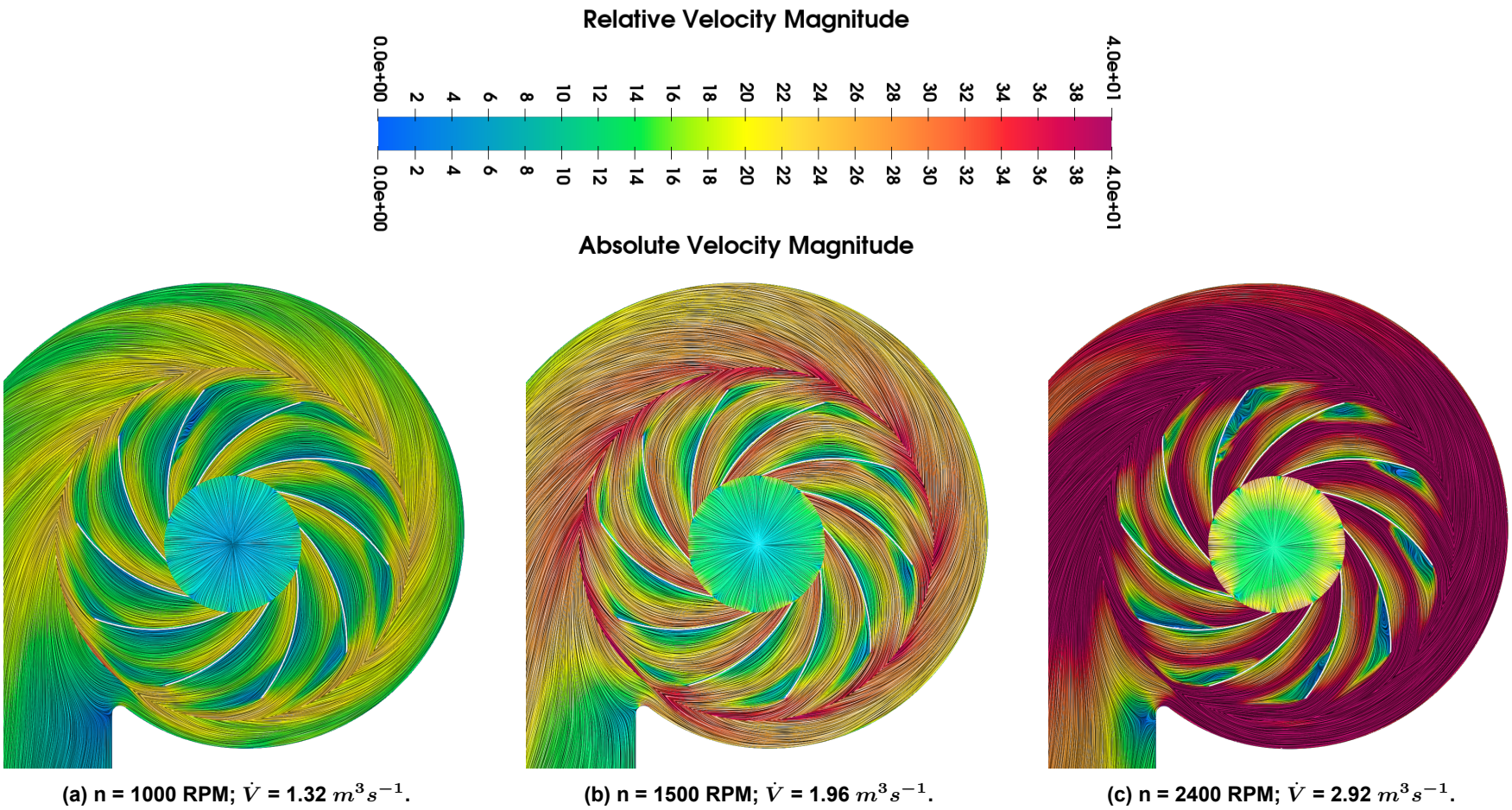
Figure 4-21: Zoomed-in Views of Impeller Zones Showing Velocity Surface-LICs for Optimal Points of TS002V0007 (RV722) at Different Impeller Speeds and at Impeller Mid Cross-Section.

4.4   Influence of Turbulence and Friction

With laminar flow and no friction on the fan walls, there will be no frictional losses on the wall and an increase in the efficiency as well as the total pressure rise is expected. To access the ability of the numerical simulation methodology used for the current thesis research, the mesh variant TS002V0007 was simulated for all operating points listed in Table 4-6 at 1500 RPM. Figure 4-22 shows a comparison of efficiency and total pressure rise with and without friction and turbulence. As expected, both efficiency and total pressure rise increase for the case of no friction and turbulence.

(a) Efficiency.   (b) Total Pressure Rise.
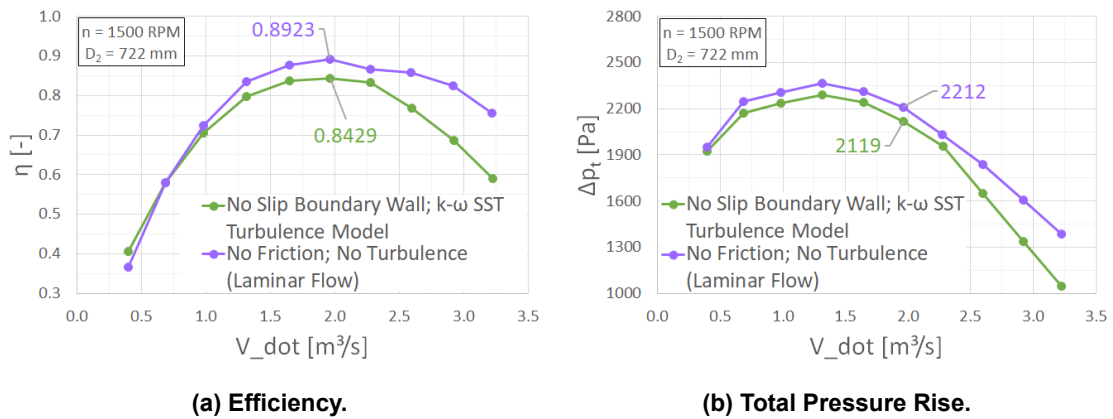
Figure 4-22: Comparison of Simulation Results for TS002V0007 (RV722) with and without Friction and Turbulence.

The y+ values on the blade surfaces for the turbulence and friction free case of the mesh variant TS002V0007 at the optimal point, $\dot{V} = 1.96 ms^{-1}$, are as shown in Table 4-10 and are visualised in Figure 4-23. The velocity Surface-LICs for the same operating point at the impeller mid cross-section are shown in Figure 4-24.
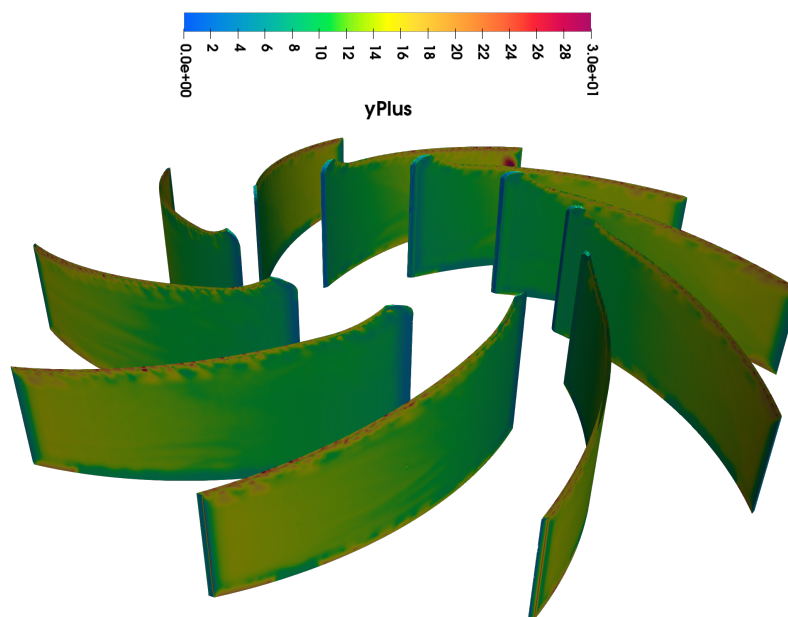
Figure 4-23: Visual Representation of Y+ Values for Turbulence and Friction Free TS002V0007 (RV722) at the Optimal Point, n = 1500 RPM and $\dot{V}$ = 1.96 ms^{-1}.

(a) n = 1500 RPM;
D_2 **= 722 mm.**

(b) n = 1500 RPM;
D_2 **= 722 mm.**
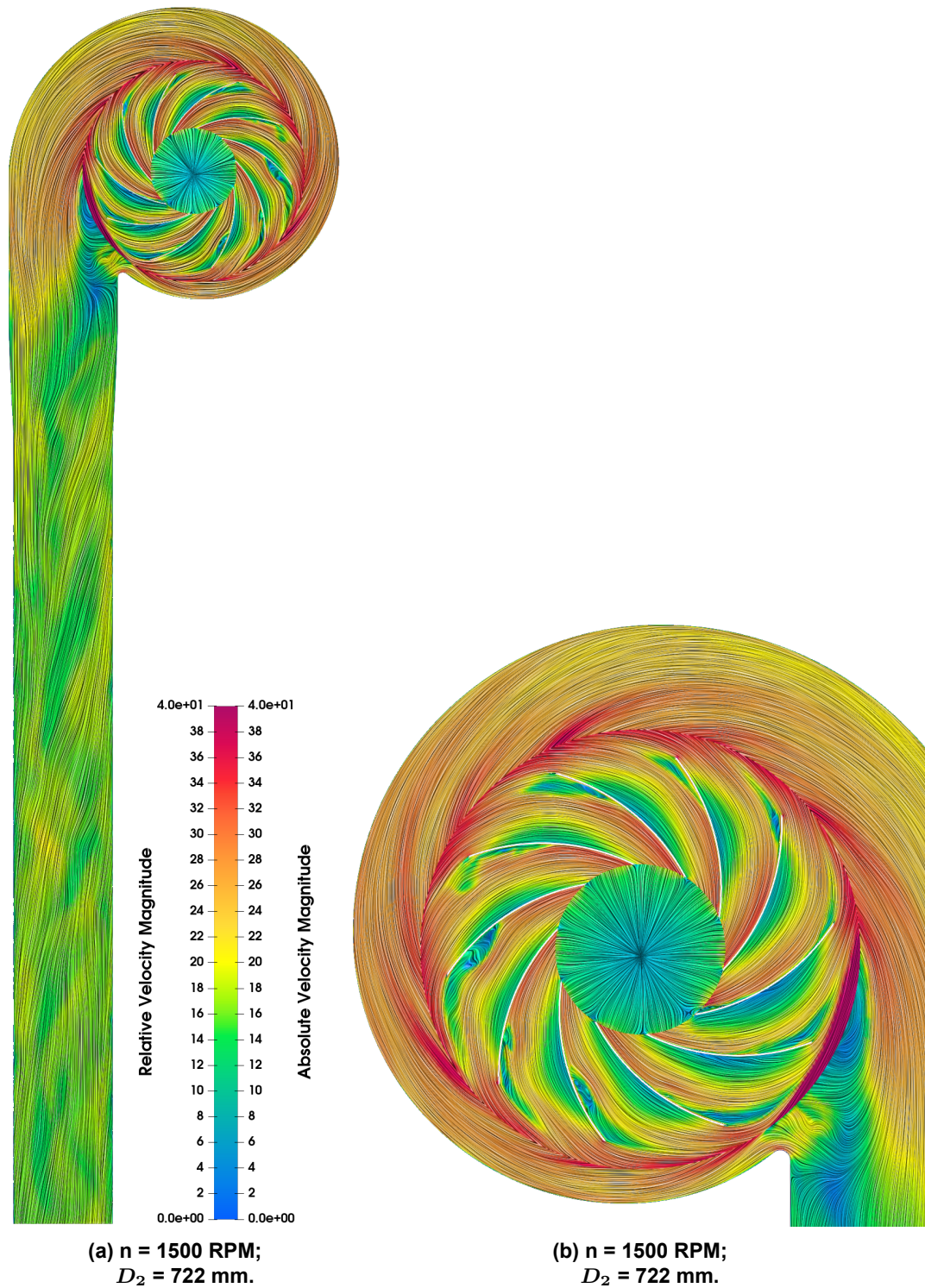
Figure 4-24: Velocity Surface-LICs for Turbulence and Friction Free TS002V0007 (RV722) at the Optimal Point, $\dot{V}$ = 1.96 ms^{-1}, at Impeller Mid Cross-Section.

	Pressure Side			Suction Side		
	Min y+	Max y+	Average y+	Min y+	Max y+	Average y+
TS003V0002	1.2799	60.9124	10.1284	0.6324	95.7328	11.2765

Table 4-10: Y+ Values for Turbulence and Friction Free TS002V0007 at its Optimal Point $\dot{V}$ = 1.96 ms^{-1}.

	Pressure Side			Suction Side		
	Min y+	Max y+	Average y+	Min y+	Max y+	Average y+
n = 1000 RPM	3.6282×10^{-3}	84.102	2.2288	0.2163×10^{-3}	409.976	3.4021
n = 1500 RPM	4.7242×10^{-3}	96.451	5.9134	2.7113×10^{-3}	608.476	3.6903
n = 2400 RPM	8.3260×10^{-3}	167.818	10.1040	5.9234×10^{-3}	934.515	6.6639

Table 4-11: Y+ Values at Optimal Points for TS003V0002 at Different Impeller Speeds.

4.5 Anomalies in Simulation of Fan at 1000 RPM

The fan efficiencies for TS002V0007 (RV722) running at 1000 RPM for the operating points 9 and 10 from Table 4-6 were not plotted in Figures 4-17. Table 4-12 lists the efficiencies and total pressure rise for TS002V0007 at 1000 RPM for these two operating points.

Operating Point Number	Mass Flowrate at Outlet [kg/s]	Corresponding Volume Flowrate [m^3/s]	Impeller Speed [RPM]	Efficiency η [-]	Δp_t [Pa]
9	3.51	2.93	1000	0.6745	-269
10	3.87	3.23	1000	3.0345	-642

Table 4-12: Efficiency and Total Pressure Rise for TS002V0007 at 1000 RPM for Two Extreme Full Load Points.

Since the fan is operating at the extremities in the full load condition with a low impeller speed, it cannot achieve the expected volume flow rate. And as discussed in Section 4.1, the outlet side is provided with velocity boundary condition. With this setup the outlet starts to suck air out from the fan, leading to increased fluid velocities at the outlet. This sort of behaviour is physically unrealistic and it hence the unrealistic efficiency values obtained at these operating points can safely be ignored. The suction of fluid from the outlet is visualised in Figure 4-25 for the operating point number 9 in Table 4-12. Given that there is no change in the cross sectional area of the mesh components- Outlet Pipe and Extra Pipe, the fluid velocity should remain constant once it exits the spiral casing. However, as seen in Figure 4-25 the velocity increases as it approaches the fan outlet. An example of how the velocities should have looked like is presented in Figure 4-26, which represents the absolute fluid velocity at the optimal point, i.e.- $\dot{V} = 1.96\ ms^{-1}$, of the same fan running at n = 1000 RPM. The fluid velocity at optimal point increases as it flows through the blade passage, as can be observed in Figure 4-26b, and reduces gradually as it flows through the spiral casing and remains constant once it exits the spiral casing, as observed in Figure 4-26a.

Absolute Velocity Magnitude (m/s)
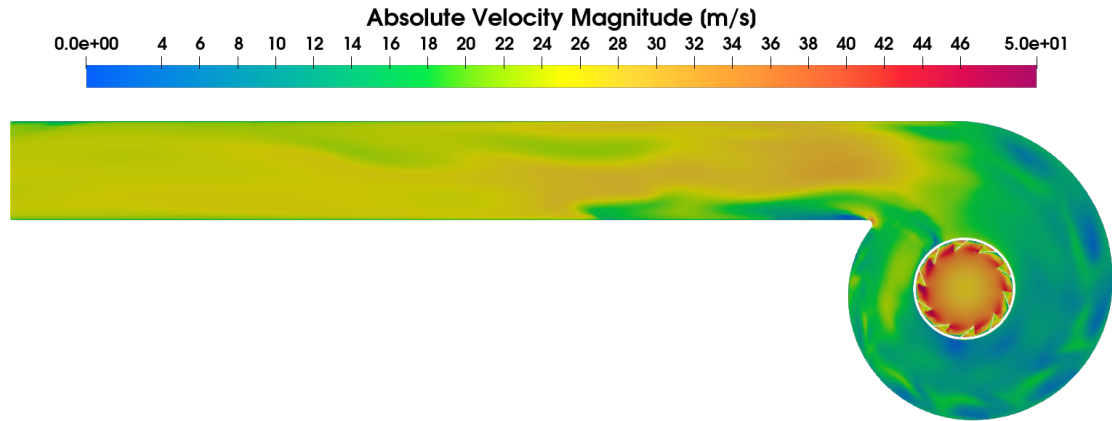
(a) Cross-sectional View at Casing Mid.

(b) Cross-sectional View at Impeller Mid.

Figure 4-25: Cross-sectional Views Showing Absolute Fluid Velocity at Point 9, i.e.- $\dot{V}$ = 2.93 ms^{-1}, of TS002V0007 (RV722) running at n = 1000 RPM.

Absolute Velocity Magnitude (m/s)
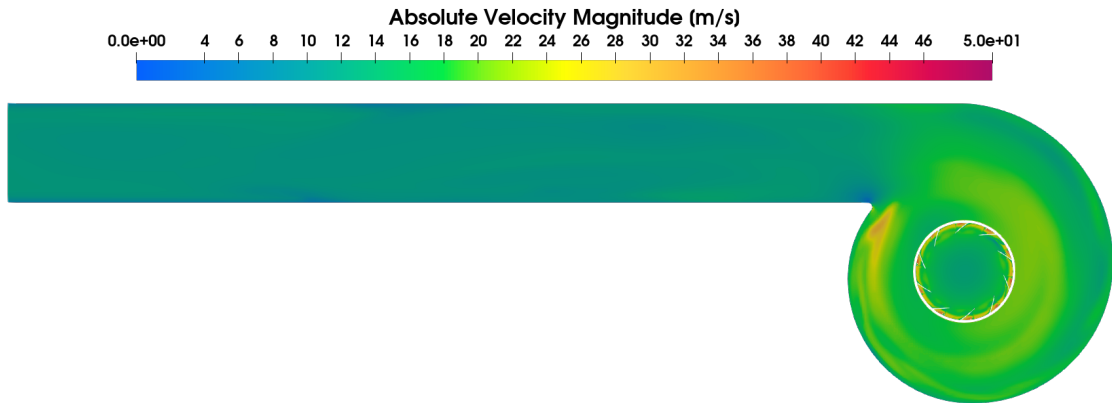
(a) Cross-sectional View at Casing Mid.

(b) Cross-sectional View at Impeller Mid.

Figure 4-26: Cross-sectional Views Showing Absolute Fluid Velocity at the Optimal Point, i.e.- $\dot{V}$ = 1.96 ms^{-1}, of TS002V0007 (RV722) running at n = 1000 RPM.

5 Design and Validation of a Fan Using Excel Tool

Now that the numerical simulation methodology had been validated, it could be used to simulate new fan designs generated via the excel methodology. However, to validate the design capability of the excel tool, it would have been essential not only to simulate the new design but also to manufacture it and validate the simulation results against its test bench results. But since the test bench results for the reference fan RV722 were already available, it would only be beneficial if a very similar fan was designed and simulated. That way the manufacturing of the new fan and running it at the test bench could be avoided. Hence, fan TS003V0002 was designed with a design point very similar to the optimal point of TS002V0007 (RV722) running at 1500 RPM. The design point details for the fan TS002V0003 are as shown in Table 5-1 and Figure 5-1 shows the different CAD views for the same fan. Since the fan was intended to be similar to RV722 and not the same, the outer diameter of the newly designed fan is $D_2 = 741$ mm. TS003V0002 was simulated for the same operating points listed in Table 4-6 at three impeller speeds of 1000 RPM, 1500 RPM, and 2400 RPM. This was done in order to have a proper base for comparison of numerical simulation results of TS003V0002 with those of TS002V0007.

Parameters	Value
Volume Flow Rate $[m^3/s]$	1.96
Total Pressure Rise $[Pa]$	2244
Rotational Speed $[RPM]$	1500
Density $[kg/m^3]$	1.2
Number of Blades	10
Shroud Angle $[\gamma]$	11°

Table 5-1: Design Point Details for TS003V0002.

Based on the experience of simulating multiple variants during the thesis research, certain changes were applied to the newly designed fan model TS003V0002 to reduce the complexity and improve the simulation time without compromising on the simulation methodology itself. The component Extra Pipe as shown in Figure 4-3, was eliminated since it served no purpose. The flow is already fully developed by the time it reaches the end of the component Outlet Pipe from Figure 4-3. This is evident from Figures 4-20 and 4-26. The diameter of the component Outlet Pipe is 316 mm and its length is 1927 mm. The ratio of the pipe length to diameter is 6.1, which is a good and sufficient ratio for a fully developed flow to form at the pipe outlet. The mesh component division for TS003V0002 is as seen in Figure 5-2.
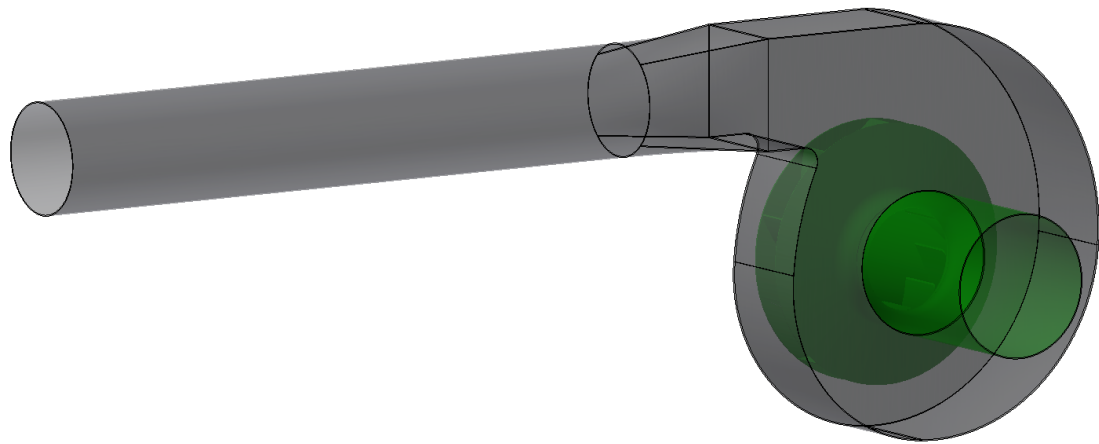
(a) Isometric View.
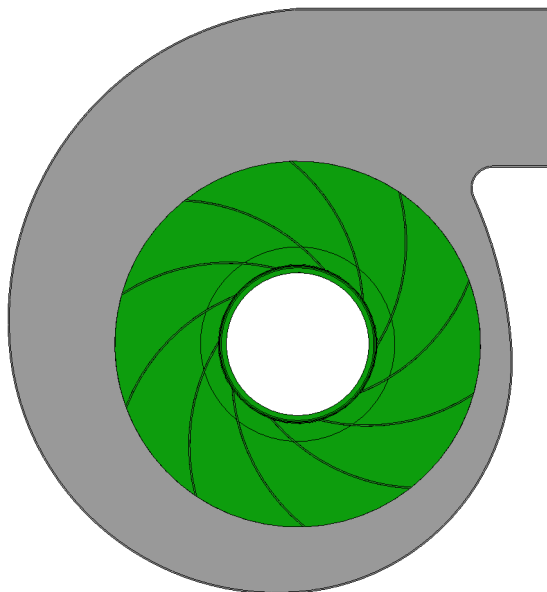
(b) Cross-sectional Rear View.
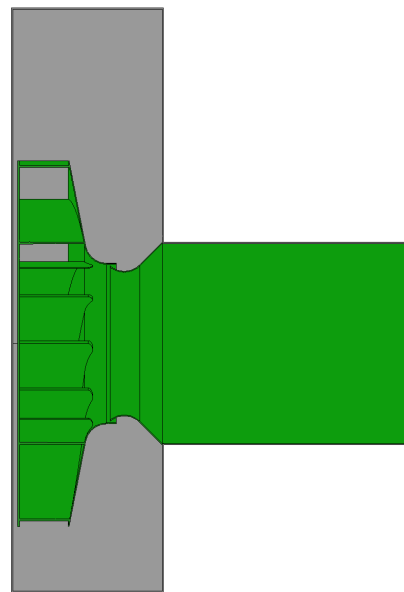
(c) Side View.

Figure 5-1: CAD Views of TS003V0002.

Component 3

1927.2 mm

400 mm

Measurement point
in TCAE Simulation

Component 1
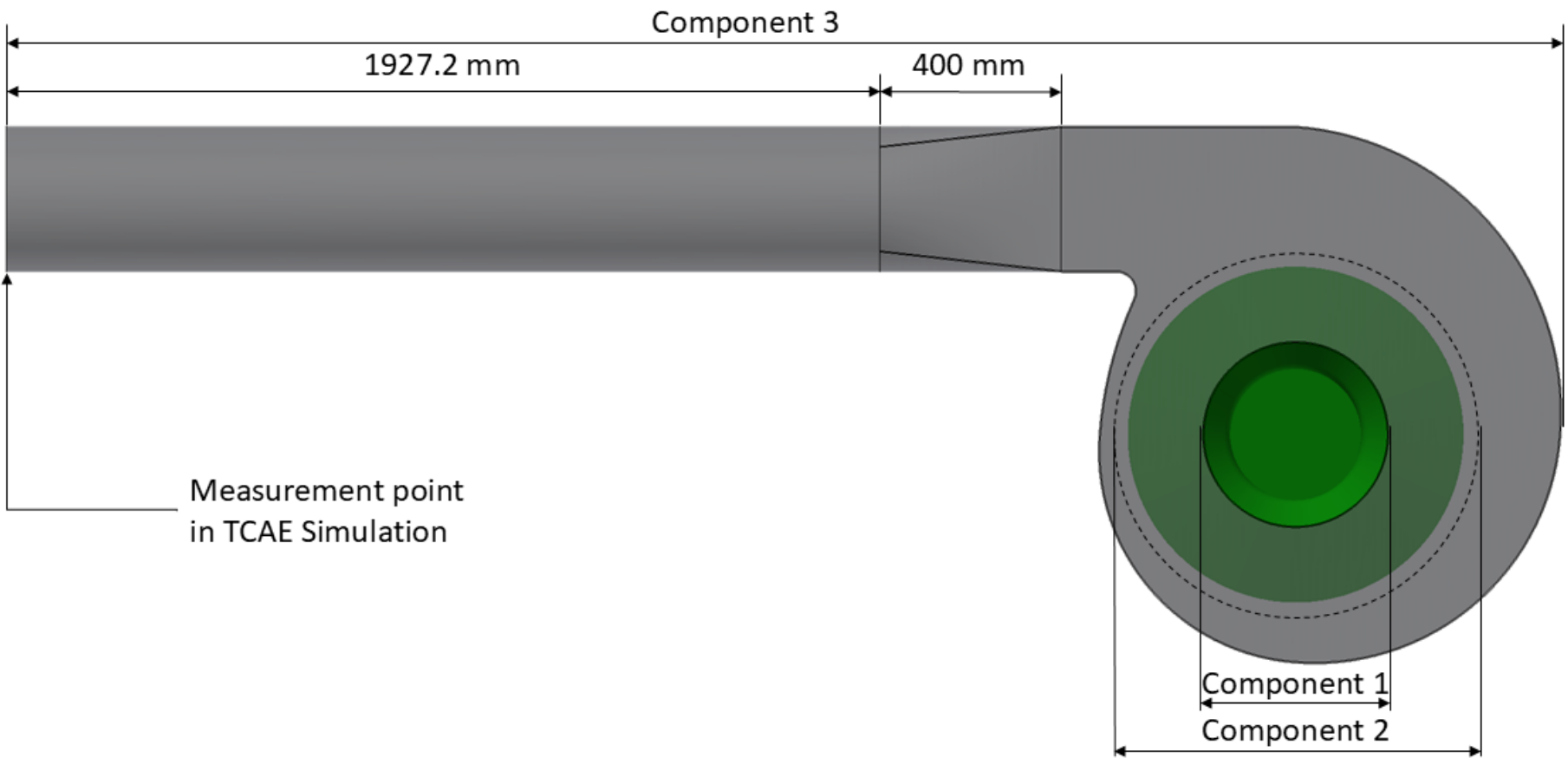
Component 2

Figure 5-2: Mesh Components for RV722.

The fan model TS003V0002 was meshed in a way similar to the mesh variant TS002V0007, leading to a very fine mesh refinement and uniform distribution of cells and a satisfactory inflation layer thickness on the blade surfaces. A comparison of number of mesh cells generated in different components and simulation details are listed in Table 5-2, together with those of TS002V0007 for cross comparison. The "—" in Table 5-2 means that the component is merged with the previously listed component and "*" means that the component is eliminated.

	Mesh Refinement and Simulation Time Details	
	TS002V0007	TS003V0002
Suction	910 541	808 665
Impeller	9 622 997	10 219 376
Casing	10 997 665	10 883 686
Loft	—	—
Outlet Pipe	—	—
Extra Pipe	611 086	*
Total	22 142 289	21 911 727
Number of cores employed	24	24
Mesh time	0.75 hours	1.5 hours
Total simulation time	55.5 hours	56.5 hours
Number of core-hours	1332	1356
Number of operating points	10	10
Iterations per operating point	1000	1000

Table 5-2: Mesh Refinement and Simulation Time Details with Respect to Table 4-4 for TS003V0002 in Comparison to TS002V0007.

The resulting y+ values on the blade surfaces of TS003V0002 for all three impeller speeds at their corresponding optimum points are presented in Table 4-11 and are visualised in Figure 5-3.

(a) TS003V0002; n = 1000 RPM;
$\dot{V}$ = 1.32 $m^3 s^{-1}$.

(b) TS003V0002; n = 1500 RPM;
$\dot{V}$ = 1.96 $m^3 s^{-1}$.

(c) TS003V0002; n = 2400 RPM;
$\dot{V}$ = 2.93 $m^3 s^{-1}$.

yPlus
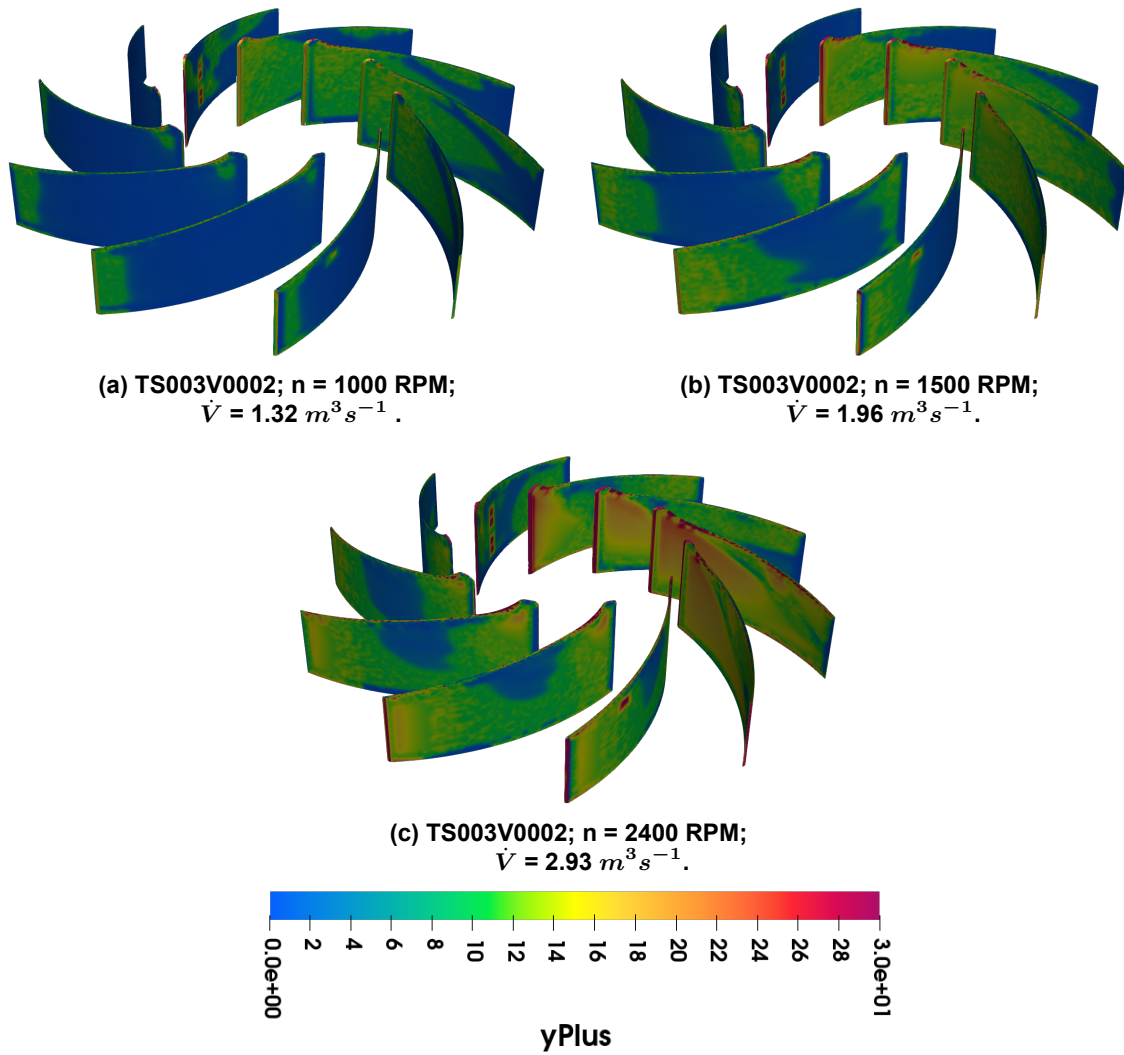
Figure 5-3: Visual Representation of Y+ Values on the Blade Surfaces of TS003V0002 for Different Impeller Speeds at Corresponding Optimal Points.

Figure 5-4 shows a comparison of fan efficiency and pressure rise as achieved by the variant TS002V0007 for all three impeller speeds. The efficiency result for the last operating point at 1000 RPM is omitted from the graph in Figure 5-4a for the same reasons discussed in Section 4.5. And as seen in the case of TS002V0007, discussed under Section 4.3, the optimum efficiencies for different impeller speeds are pretty much the same, again emphasising the fact that it is just one machine (fan) with same performance characteristics. The same is visualised in Figure 5-5 by plotting the dimensionless characteristic curves for the fan at different impeller speeds. Further, Table 5-3 lists the fan Reynolds number corresponding to different impeller speeds for TS003V0002 in comparison to those of

TS002V0007.

Impeller Speed N [RPM]	Fan Reynolds Number, Re_{fan}	
	TS002V0007	TS003V0002
1000	2.52×10^6	2.59×10^6
1500	3.78×10^6	3.88×10^6
2400	6.05×10^6	6.21×10^6

Table 5-3: Fan Reynolds Numbers for Different Impeller Speeds of TS003V0002 in Comparison to those of TS002V0007.

(a) Efficiency.

(b) Total Pressure Rise.
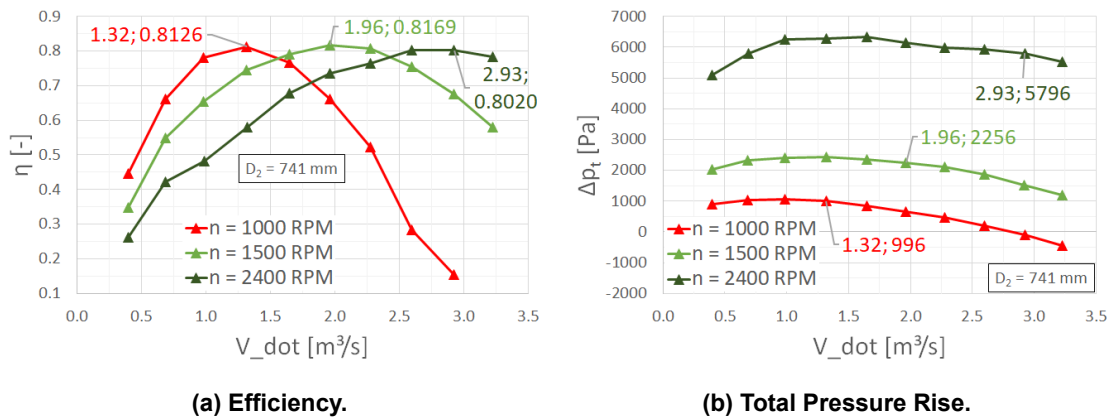
Figure 5-4: Efficiency and Total Pressure Rise for TS003V0002 at Different Impeller Speeds.

(a) η v/s ϕ.

(b) ψ v/s ϕ.
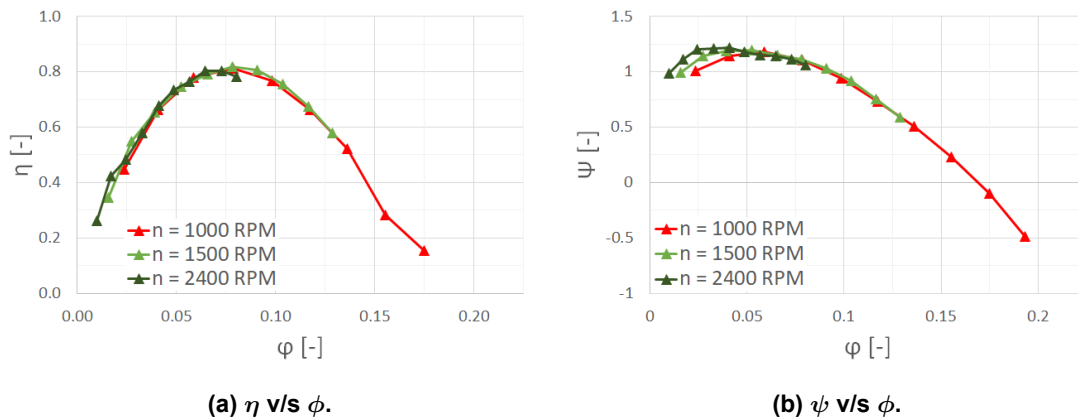
Figure 5-5: Dimensionless Characteristic Curves for TS003V0002.

The characteristic curves for TS003V0002 at different impeller speeds overlap each other to a very good extent, once again proving the accuracy and reliability of the numerical simulation method. Figure 5-6 shows a comparison of efficiencies and total pressure rise for both, the reference fan (RV722) and the newly designed fan (TS003V0002) at all three impeller speeds. It is evident from Figures 5-6a, 5-6c, and 5-6e that the efficiencies for

the newly designed fan at the optimum points corresponding to each impeller speed are around 2 to 3 percent lower compared to those of the reference fan. This is because the new fan is designed in the excel tool as per Horvat [17] and fits right in accordance to the reasons discussed in Section 3.2.

(a) Comparison of η at n = 1000 RPM.

(b) Comparison of ΔP_t at n = 1000 RPM.

(c) Comparison of η at n = 1500 RPM.

(d) Comparison of ΔP_t at n = 1500 RPM.

(e) Comparison of η at n = 2400 RPM.

(f) Comparison of ΔP_t at n = 2400 RPM.
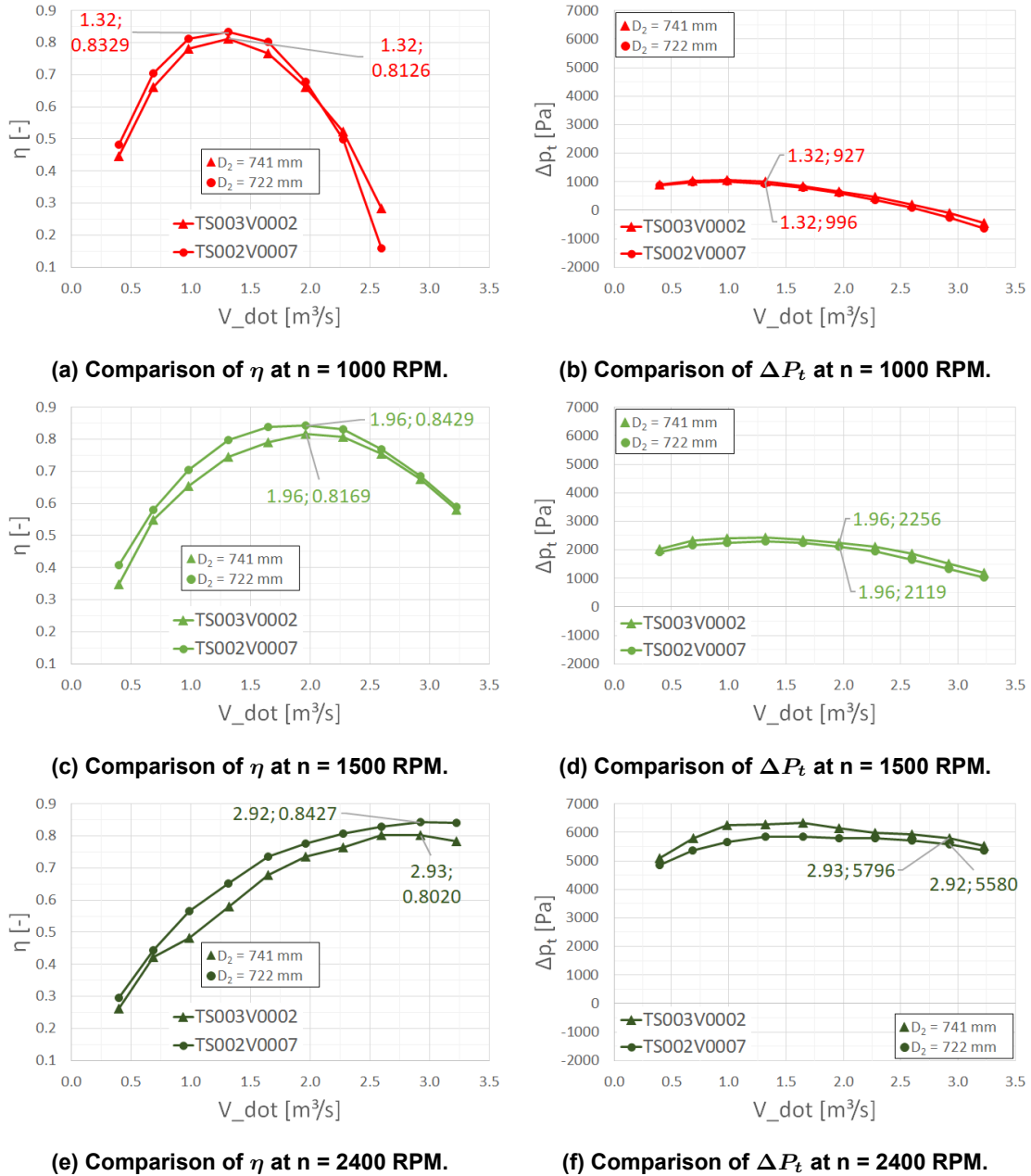
Figure 5-6: Comparison of Efficiency and Total Pressure Rise at Different Impeller Speeds for TS003V0002 and TS002V0007.

Figure 5-7 show the velocity Surface-LICs for TS003V0002 at different impeller speeds and their corresponding optimal points. The flow within the casing and the Outlet Pipe exhibits a similar trend to that of the reference fan and there are no curls or flow separation regions visible. However, there is considerable flow separation within the blade passages. This can be observed much better in a zoomed in view on the impeller region as shown in Figure 5-9.

(a) n = 1000 RPM;
$\dot{V}$ = 1.32 $m^3 s^{-1}$.

(b) n = 1500 RPM;
$\dot{V}$ = 1.96 $m^3 s^{-1}$.

(c) n = 2400 RPM;
$\dot{V}$ = 2.93 $m^3 s^{-1}$.
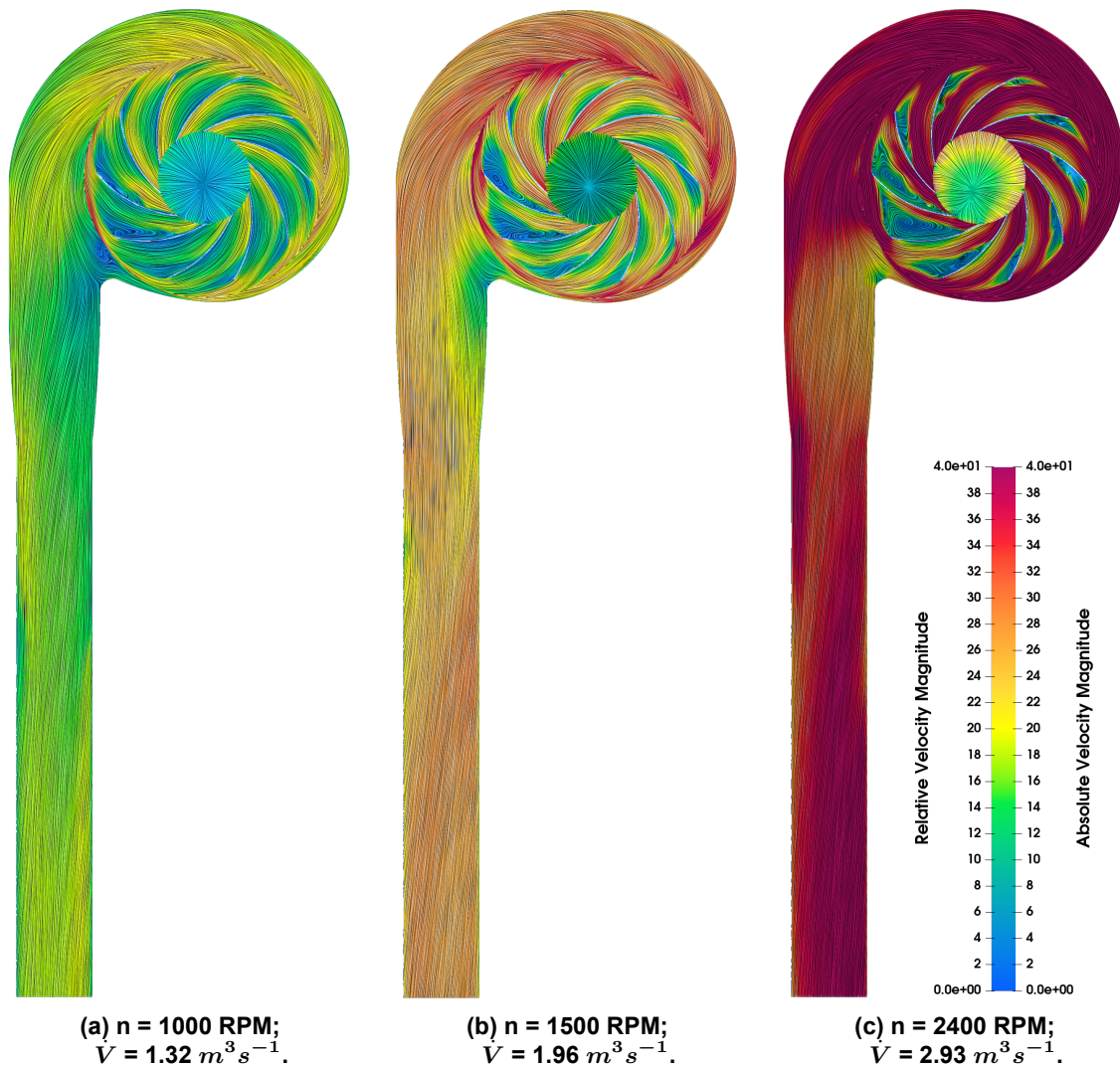
Figure 5-7: Velocity Surface-LICs for Optimal Points of TS003V0002 at Different Impeller Speeds and at Impeller Mid Cross-Section.

Figure 5-8 shows a comparison of velocity Surface-LICs in the impeller zones for TS002V0007 (RV722) and TS003V0002 running at 2400 RPM and on the impeller mid cross-section and at their optimal points, i.e.- point 9 in Table 4-6. It can be observed that there are very few curls with small magnitudes within the blade passages and no curls at all in the casing zone for RV722. Whereas, there are significantly developed curls in the blade passages for TS003V0002, especially near the tongue region. In Figure 5-8b a very interesting trend can be observed. The curl in the blade channel has the highest magnitude just before hitting the tongue and its magnitude reduces gradually as the blade rotates further away from the tongue. This also leads to unequal feeding of air into the blade passages and can be clearly observed in Figure 5-8b, where the center of the air velocity field in the suction zone moves closer to the blade passage that is at the tongue. This shows that the blade passage at the tongue are unable to breathe in air properly and the ones away from the tongue are able to suck in good amount of air. Figure 5-8a shows the ideal and equal distribution of air to all the blade passages with the center of velocity field situated right in the center of the

suction zone.

(a) TS002V0007; n = 2400 RPM; $\dot{V}$ = 2.92 m^3s^{-1}. (b) TS003V0002; n= 2400 RPM; $\dot{V}$ = 2.93 m^3s^{-1}.
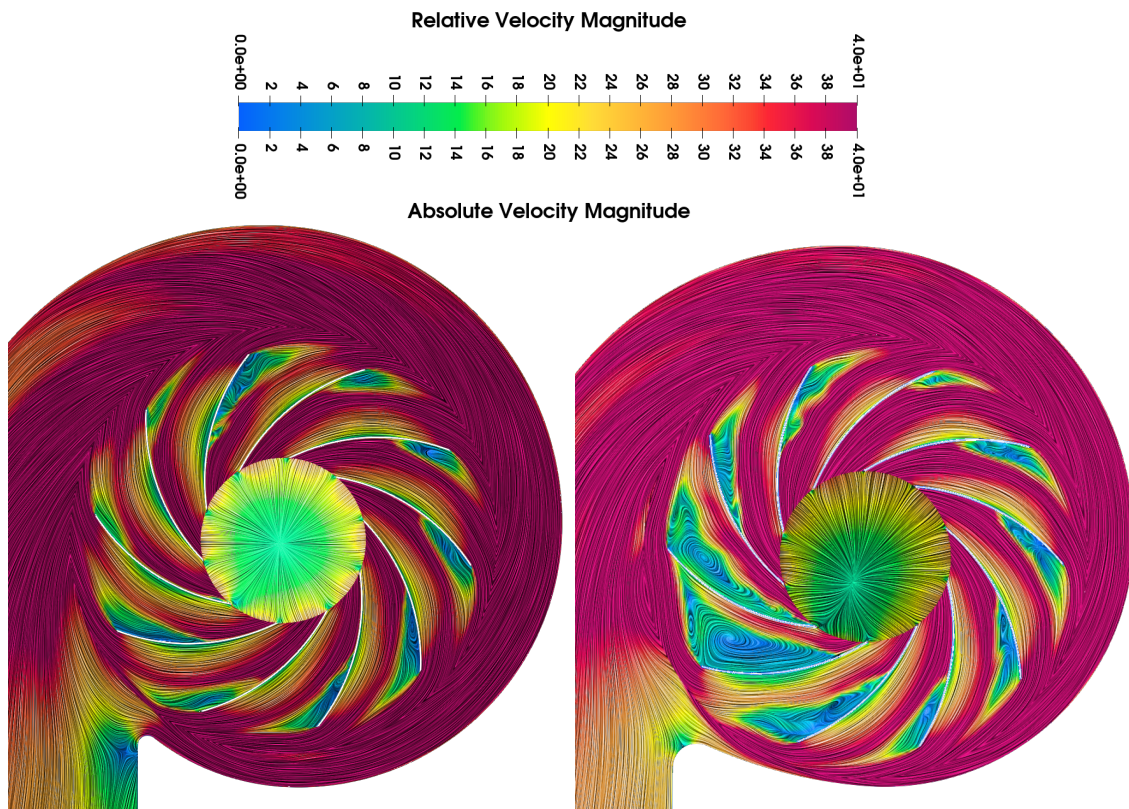
Figure 5-8: Comparison of Velocity Surface-LICs for Optimal Points of TS002V0007 and TS003V0002 at 2400 RPM and at Impeller Mid Cross-Section.

Relative Velocity Magnitude

0.0e+00 2 4 6 8 10 12 14 16 18 20 22 24 26 28 30 32 34 36 38 4.0e+01

Absolute Velocity Magnitude

(a) n = 1000 RPM; $\dot{V}$ = 1.32 $m^3 s^{-1}$.

(b) n = 1500 RPM; $\dot{V}$ = 1.96 $m^3 s^{-1}$.

(c) n = 2400 RPM; $\dot{V}$ = 2.92 $m^3 s^{-1}$.
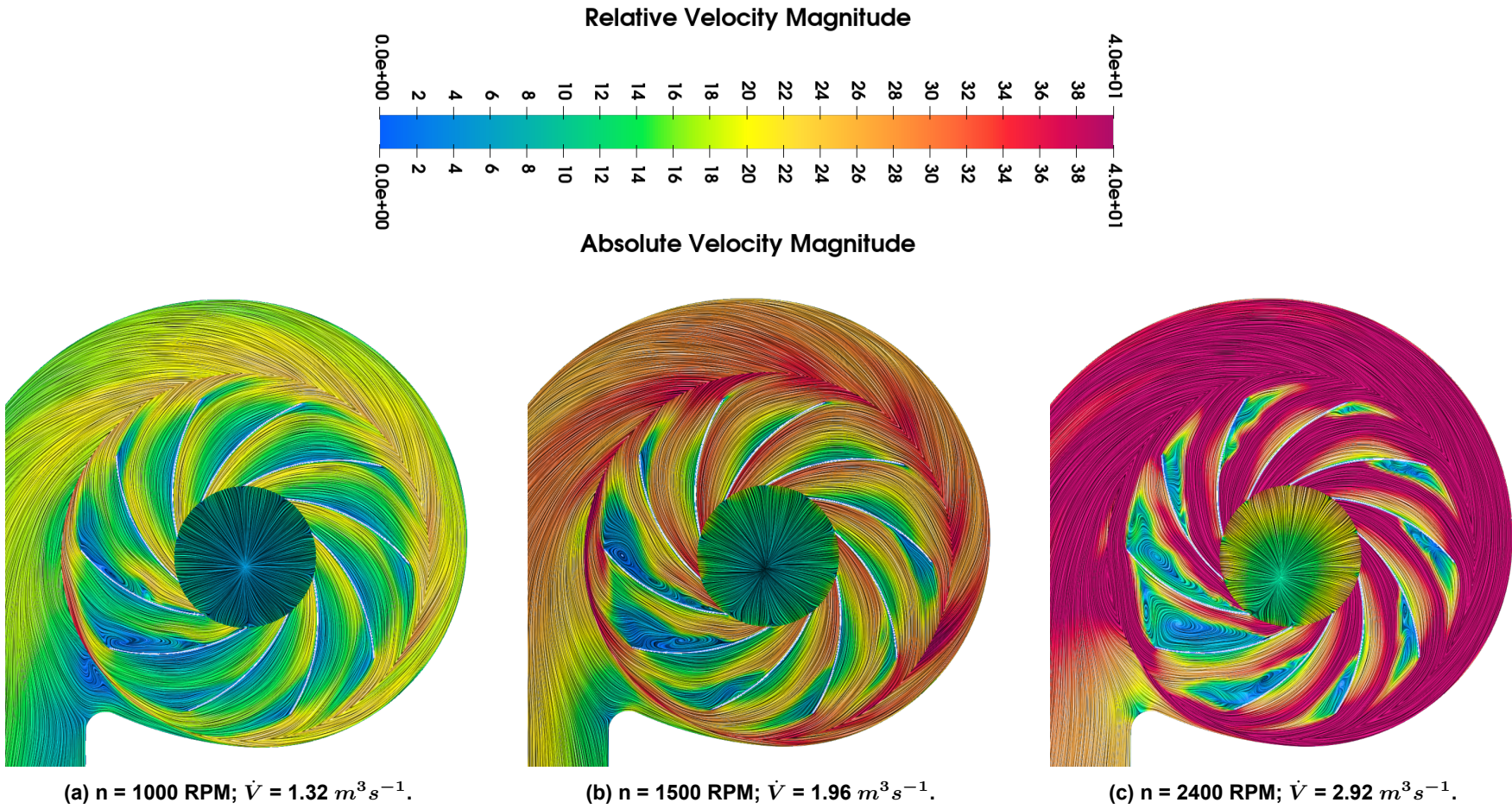
Figure 5-9: Zoomed-in Views of Impeller Zones Showing Velocity Surface-LICs for Optimal Points of TS003V0002 at Different Impeller Speeds and at Impeller Mid Cross-Section.

6 Conclusion

The commercial numerical simulations tool TCAE had to be tested for its reliability and reproducibility by developing a simulation methodology in it and validating its results against test bench results and atleast one other commercial numerical simulation tool. A reliable simulation methodology was proposed and tested against various mesh refinements and impeller speeds and for more than one fan design. The simulation methodology proved itself very much capable and competitive compared to other expensive numerical simulation tools as seen in Section 4.1 and 5. Different mesh refinements were tested and a general set of guidelines were laid down for meshing fan models within TCAE using snappyHexMesh tool. The simulation methodology was also tested for various impeller speeds where it was able to predict the fan performance to a good degree without violating the fan performance characteristics.

During the course of this thesis, the available fan design methodologies and tools at the institute of ISAVE in Hochschule Düsseldorf were studied extensively. Certain aspects of the excel fan design tool lack proper backing up with literature or experimental results as pointed out in Section 3.2. The excel fan design tool is capable of designing a nearly perfect impeller as per Bommes methodology. But more research and detailed simulation based testing is needed to improve the casing design methodology employed in the current excel tool. Additionally, a casing spiral width optimisation strategy that takes into consideration and does not violate the Bommes methodology of designing the impeller needs to be developed in the future.

Finally, a new fan model, TS003V0002, was designed independently using the excel tool and simulated using the proposed numerical simulation methodology. Its simulation results were validated against expected results in Section 5. The newly designed fan model had small deviations of about 2-3% in fan efficiency from the expected results for the reasons discussed in Section 3.2. In the future, the tool could be expanded to include casing spiral designs as per more than one methodology or literature along with other parameter variations. For example, the Bommes impeller position, the Horvat impeller position, spiral designed as per Equation 3.1 [20, Ch. 3.6, p. 73].

References

[1] DIRECTIVE (EU) 2023/1791 OF THE EUROPEAN PARLIAMENT AND OF THE COUNCIL of 13 september 2023 on energy efficiency and amending Regulation (EU) 2023/955 (recast). Official Journal of the European Union, September 2023.

[2] Lewis, R. I. *TURBOMACHINERY PERFORMANCE ANALYSIS*. Elsevier Science & Technology Books, 1996.

[3] Pai, B. U. *Turbomachines*. Wiley India, 2013.

[4] Cory, W. *Fans and Ventilation*. Elsevier Science, 2005.

[5] Eurovent 1/1. *Fan Terminology*. Technical report, EUROVENT EUROPEAN IN-DUSTRY ASSOCIATION, Paris, 1984.

[6] ISO 13348:2006(E). *Industrial fans - Tolerances, methods of conversion and technical data presentation*. Standard, International Organization for Standardization, Geneva, Switzerland, March 2006.

[7] Bleier, F. P. *Fan Handbook Selection, Application, and Design*. McGraw-Hill, 1997.

[8] Carolus, T. *Ventilatoren*. Springer-Verlag GmbH, fourth edition, February 2020.

[9] FanManDan. *"Fan Types - Why Choose An Mixed Flow / Diagonal Fan"*. Available online under: https://www.hydroexperts.com.au/Fan-Types-Why-Choose-an-Mixed-Flow-/-Diagonal-Fan, Nov 2019, last accessed on 30.07.2022.

[10] Bommes, L., Fricke, J., and Klaes, K. *Ventilatoren*. Vulkan-Verlag Essen, first edition, 1994.

[11] Greitzer, E. M., Spakovszkyl, Z. S., and Waitz, I. A. Thermodynamics and Propulsion. Available online under: https://web.mit.edu/16.unified/www/FALL/thermodynamics/notes/node91.html#: :text=The Lecture Notes.

[12] Schade, H., Kunz, E., Kameier, F., and Paschereit, O. *Strömungslehre*. DE GRUYTER STUDIUM, fifth edition, November 2021. ISBN: 978-3-11-064144-8.

[13] Massey, B. and Revised by Ward-Smith, J. *Mechanics of Fluids*. Taylor & Francis, London and New York, eighth edition, 2005.

[14] Epple, Ph., Durst, F., and Delgado, A. A theoretical derivation of the Cordier diagram for turbomachines. *Proceedings of the Institution of Mechanical Engineers, Part C: Journal of Mechanical Engineering Science*, pages 354–368, 2011.

[15] Bommes, L. and Reinartz, D. Entwurfspolynome zur optimalen Auswahl und Be-messung von Industrieventilatoren radialer Bauart. *Wissenschaftlich- Technische Konferenz Industrieventilatoren, Zakopane*, October 1997.

[16] Bommes, L. and Reinartz, D. Polynomisches Verfahren zur optimalen Gestaltug von Radialventilatoren. *HLH*, Bd. 48(Nr.4):pages 20–32, April 1997.

[17] Horvat, I. and Kameier, F. Laufrad_inventor_eingabe.xls, June 2009. Internal.

[18] Wikipedia: Leonhard Bommes, 2022. Available online under: https://de.wikipedia.org/wiki/Leonhard_ Bommes, last accessed on 31.08.2022.

[19] Horvat, I. and Kameier, F. CAE für Radialventilatoren unter dem Gesichtspunkt des Umweltschutzes – Energieeffizienz, Haltbarkeit, Lärm. Abschlussbericht, Labor für Strömungstechnik und Akustik, Fachhochschule Düsseldorf, Düsseldorf, October 2009.

[20] Mode, F. *VENTILATORANLAGEN*. De Gruyter, Berlin, fourth edition, 1972.

[21] Güntzel, D. and Gottschalk, J. Rechnergestützte Untersuchung eines Radialventilators im Hinblick auf seine Bemessungsgrößen und sein Betriebsverhalten. Diplomarbeit, Department of Mechanical and Process Engineering, Fachhochschule Düsseldorf, Düsseldorf, February 1987.

[22] Müller, G. Auslegung und Erprobung einer leisen und effizienten Radialventilatoreneinheit für den Einsatz in einem Océ Farbkopierer. Diplomarbeit, Department of Mechanical and Process Engineering, Fachhochschule Düsseldorf, Düsseldorf, July 2001.

[23] Kameier, F. and Horvat, I. centrifugal_fan_design_ISAVE_excel2016_education_061217_mit_inventor.xls. Microsoft Excel, August 2024. Lecture Material.

[24] Kameier, F. ventilatorauslegung_skizzen_lösung_neu23052024.pptx, May 2024. Lecture Material.

[25] Pohlmann, T. RV722-CFD.xlsx, Sheet:Daten, March 2022.

[26] Sariaslan, E. Messung und Prognose von Ventilatorgeräuschen. Diplomarbeit, Department of Mechanical and Process Engineering, Fachhochschule Düsseldorf, Düsseldorf, August 2004.

[27] Strauch, H. J. and Schneider, J. Berechnung und Entwurf eines Radialventilators und experimentelle Überprüfung der aerodynamischen und akustischen Betriebsdaten an einem Modelventilator. Diplomarbeit, Department of Mechanical and Process Engineering, Fachhochschule Düsseldorf, Düsseldorf, May 1989.

[28] CFD SUPPORT s.r.o., Czech Republic. *TCAE Manual*, Version 24.03 edition, 2023. Available online under: https://www.cfdsupport.com/download/TCAE-manual.pdf, last accessed on 15.09.2024.

[29] jousefm. What is y+ (yplus)? Available online under: https://www.simscale.com/forum/t/what-is-y-yplus/82394, November 2020, last accessed on 09.09.2024.

[30] Vinerm. Required Y+ Range for k-Omega Standard and SST. Available online under: https://www.cfd-online.com/Forums/fluent/225077-required-y-range-k-omega-standard-sst.html, March 2020, last accessed on 09.09.2024.

[31] Cadence CFD Solutions. Y+ Boundary Layer Thickness. Available online under: https://resources.system-analysis.cadence.com/blog/msa2023-y-boundary-layer-thickness.

[32] Phelan, J. J., Russell, S. H., and Zeluff, W. C. A study of the influence of reynolds number on the performance of centrifugal fans. *Journal of Engineering for Power*, Vol. 101:pages 670–676, October 1979.

Appendices

Appendix A: Simulation Results from TCAE for Each Operating Point

The simulation result data used to plot graphs in Figures 4-12,4-17, 4-18, 4-22, 5-4, and 5-5 and their derived graphs in other figures are represented in the following tables.

Operating Point Number	Volume Flowrate [m³/s]	Efficiency η [-]	Total Pressure Rise Δp_t [Pa]	Flow Coefficient ϕ [-]	Pressure Coefficient ψ [-]
1	0.40	0.4351	2156	0.0170	1.1173
2	0.68	0.6063	2261	0.0295	1.1720
3	0.98	0.7228	2240	0.0423	1.1608
4	1.32	0.7806	2307	0.0567	1.1959
5	1.65	0.8237	2255	0.0709	1.1689
6	1.96	0.8347	2140	0.0845	1.1093
7	2.28	0.8170	1962	0.0981	1.0170
8	2.60	0.7654	1699	0.1119	0.8804
9	2.93	0.6881	1372	0.1259	0.7109
10	3.23	0.6298	1162	0.1390	0.6023

Table A-1: Numerical Simulation Results for TS002V0003 from TCAE; n = 1500 RPM; D_2 = 722 mm.

Operating Point Number	Volume Flowrate [m³/s]	Efficiency η [-]	Total Pressure Rise Δp_t [Pa]	Flow Coefficient ϕ [-]	Pressure Coefficient ψ [-]
1	0.38	0.4700	2182	0.0164	1.1309
2	0.66	0.6482	2255	0.0285	1.1689
3	0.97	0.7367	2238	0.0416	1.1601
4	1.30	0.7914	2238	0.0560	1.1602
5	1.63	0.8267	2252	0.0700	1.1672
6	1.94	0.8423	2144	0.0834	1.1110
7	2.25	0.8176	1962	0.0967	1.0171
8	2.56	0.7658	1692	0.1103	0.8768
9	2.88	0.6959	1375	0.1242	0.7129
10	3.18	0.6009	1093	0.1370	0.5668

Table A-2: Numerical Simulation Results for TS002V0004 from TCAE; n = 1500 RPM; D_2 = 722 mm.

Operating Point Number	Volume Flowrate [m³/s]	Efficiency η [-]	Total Pressure Rise Δp_t [Pa]	Flow Coefficient ϕ [-]	Pressure Coefficient ψ [-]
1	0.40	0.4829	872	0.0255	1.0168
2	0.69	0.7047	974	0.0442	1.1358
3	0.98	0.8124	998	0.0635	1.1638
4	1.32	0.8329	927	0.0850	1.0813
5	1.65	0.8017	798	0.1064	0.9311
6	1.96	0.6789	590	0.1267	0.6881
7	2.28	0.4998	368	0.1470	0.4293
8	2.60	0.1599	94	0.1677	0.1098
9	2.92	0.6745	-269	0.1888	-0.3141
10	3.23	3.0345	-642	0.2084	-0.7491

Table A-3: Numerical Simulation Results for TS002V0007 from TCAE; n = 1000 RPM; D_2 = 722 mm.

Operating Point Number	Volume Flowrate [m³/s]	Efficiency η [-]	Total Pressure Rise Δp_t [Pa]	Flow Coefficient ϕ [-]	Pressure Coefficient ψ [-]
1	0.40	0.4070	1924	0.0170	0.9973
2	0.69	0.5799	2173	0.0295	1.1266
3	0.98	0.7045	2238	0.0424	1.1602
4	1.32	0.7983	2290	0.0567	1.1868
5	1.65	0.8372	2242	0.0709	1.1621
6	1.96	0.8429	2119	0.0845	1.0985
7	2.28	0.8322	1959	0.0981	1.0152
8	2.60	0.7681	1652	0.1118	0.8564
9	2.92	0.6856	1338	0.1258	0.6936
10	3.23	0.5905	1046	0.1389	0.5421

Table A-4: Numerical Simulation Results for TS002V0007 from TCAE; n = 1500 RPM; D_2 = 722 mm.

Operating Point Number	Volume Flowrate [m³/s]	Efficiency η [-]	Total Pressure Rise Δp_t [Pa]	Flow Coefficient ϕ [-]	Pressure Coefficient ψ [-]
1	0.40	0.2951	4855	0.0107	0.9829
2	0.69	0.4432	5351	0.0185	1.0834
3	0.98	0.5654	5668	0.0265	1.1476
4	1.32	0.6527	5860	0.0355	1.1865
5	1.65	0.7351	5843	0.0443	1.1830
6	1.96	0.7751	5801	0.0528	1.1744
7	2.28	0.8071	5781	0.0613	1.1705
8	2.60	0.8286	5714	0.0699	1.1570
9	2.92	0.8427	5580	0.0787	1.1298
10	3.23	0.8405	5359	0.0869	1.0851

Table A-5: Numerical Simulation Results for TS002V0007 from TCAE; n = 2400 RPM; D_2 = 722 mm.

HSD

ISAVE

Operating Point Number	Volume Flowrate [m³/s]	Efficiency η [-]	Total Pressure Rise Δp_t [Pa]	Flow Coefficient ϕ [-]	Pressure Coefficient ψ [-]
1	0.40	0.3670	1952	0.0171	1.0120
2	0.69	0.5806	2246	0.0295	1.1639
3	0.98	0.7249	2305	0.0423	1.1947
4	1.32	0.8357	2363	0.0566	1.2246
5	1.65	0.8769	2314	0.0708	1.1991
6	1.96	0.8923	2212	0.0844	1.1464
7	2.27	0.8668	2029	0.0979	1.0517
8	2.59	0.8579	1838	0.1117	0.9525
9	2.92	0.8252	1606	0.1257	0.8324
10	3.22	0.7549	1384	0.1387	0.7174

Table A-6: Numerical Simulation Results for TS002V0007 from TCAE; n = 1500 RPM; D_2 = 722 mm; Friction and Turbulence Free.

Operating Point Number	Volume Flowrate [m³/s]	Efficiency η [-]	Total Pressure Rise Δp_t [Pa]	Flow Coefficient ϕ [-]	Pressure Coefficient ψ [-]
1	0.40	0.4463	911	0.0236	1.0093
2	0.69	0.6623	1032	0.0410	1.1437
3	0.98	0.7803	1066	0.0588	1.1808
4	1.32	0.8126	996	0.0787	1.1036
5	1.65	0.7666	852	0.0985	0.9435
6	1.96	0.6619	661	0.1173	0.7327
7	2.28	0.5215	455	0.1361	0.5042
8	2.60	0.2834	209	0.1553	0.2318
9	2.93	0.1541	−89	0.1749	−0.0986
10	3.23	1.0590	−439	0.1931	−0.4867

Table A-7: Numerical Simulation Results for TS003V0002 from TCAE; n = 1000 RPM; D_2 = 741 mm.

Operating Point Number	Volume Flowrate [m³/s]	Efficiency η [-]	Total Pressure Rise Δp_t [Pa]	Flow Coefficient ϕ [-]	Pressure Coefficient ψ [-]
1	0.40	0.3474	2019	0.0158	0.9943
2	0.69	0.5480	2319	0.0274	1.1419
3	0.98	0.6540	2405	0.0392	1.1840
4	1.32	0.7453	2430	0.0525	1.1965
5	1.65	0.7916	2340	0.0656	1.1519
6	1.96	0.8169	2256	0.0782	1.1109
7	2.28	0.8064	2098	0.0907	1.0329
8	2.60	0.7546	1866	0.1035	0.9186
9	2.92	0.6761	1526	0.1165	0.7511
10	3.23	0.5792	1201	0.1287	0.5911

Table A-8: Numerical Simulation Results for TS003V0002 from TCAE; n = 1500 RPM; D_2 = 741 mm.

Operating Point Number	Volume Flowrate [m³/s]	Efficiency η [-]	Total Pressure Rise Δp_t [Pa]	Flow Coefficient ϕ [-]	Pressure Coefficient ψ [-]
1	0.40	0.2608	5107	0.0099	0.9822
2	0.69	0.4224	5797	0.0171	1.1148
3	0.99	0.4820	6246	0.0245	1.2012
4	1.32	0.5804	6285	0.0328	1.2088
5	1.65	0.6781	6325	0.0411	1.2164
6	1.96	0.7351	6138	0.0489	1.1805
7	2.28	0.7630	5986	0.0567	1.1513
8	2.60	0.8022	5941	0.0647	1.1426
9	2.93	0.8020	5796	0.0729	1.1147
10	3.23	0.7829	5529	0.0804	1.0634

Table A-9: Numerical Simulation Results for TS003V0002 from TCAE; n = 2400 RPM; D_2 = 741 mm.

HSD

ISAVE

Appendix B: Simulation Results From Ansys CFX for RV722

The results for numerical simulation of RV722 CAD model in Ansys CFX as reported by [25] are listed in Table B-1.

Operating Point Number	Volume Flowrate [m³/s]	Efficiency η [-]	Total Pressure Rise Δp_t [Pa]	Flow Coefficient ϕ [-]	Pressure Coefficient ψ [-]
1	0.39	0.4498	2147	0.0169	1.1128
2	0.68	0.6221	2176	0.0294	1.1277
3	0.98	0.7139	2233	0.0424	1.1572
4	1.32	0.7867	2225	0.0567	1.1533
5	1.65	0.8201	2202	0.0711	1.1413
6	1.96	0.8196	2085	0.0844	1.0806
7	2.28	0.7961	1890	0.0980	0.9795
8	2.60	0.7563	1637	0.1120	0.8484
9	2.93	0.6963	1360	0.1260	0.7050
10	3.23	0.6281	1143	0.1389	0.5925

Table B-1: Numerical Simulation Results for RV722 from Ansys CFX; n = 1500 RPM; D_2 = 722 mm.

Appendix C: Test Bench Results for RV722

The results for numerical simulation of RV722 CAD model in Ansys CFX as reported by [25] are listed in Table C-1.

Operating Point Number	Volume Flowrate [m³/s]	Efficiency η [-]	Total Pressure Rise Δp_t [Pa]	Flow Coefficient ϕ [-]	Pressure Coefficient ψ [-]
1	0.39	0.5119	2480	0.0166	1.2854
2	0.68	0.6594	2543	0.0287	1.3180
3	0.98	0.7595	2534	0.0413	1.3135
4	1.32	0.8243	2475	0.0553	1.2828
5	1.65	0.8605	2382	0.0693	1.2347
6	1.96	0.8654	2239	0.0828	1.1605
7	2.28	0.8499	2068	0.0962	1.0719
8	2.60	0.8259	1872	0.1100	0.9705
9	2.92	0.7690	1610	0.1243	0.8347
10	3.23	0.6892	1323	0.1376	0.6857

Table C-1: Test Bench Results for RV722; n = 1500 RPM; D_2 = 722 mm.

Appendix D: Mesh Refinement Settings Used for All Simulation Models in TCAE

The following figures show the mesh refinement settings applied in TCAE for meshing the CAD models used for numerical simulations.

TS002V0003

name	type	reference frame	min refinement	max refinement	layers
Suction-Impeller-interface	outletInterface	static	3	3	-
Suction-inlet	inlet	static	1	1	-
Suction-wall	wall	static	1	1	10

SnappyHexMesh parameters
Background mesh cell size: 0.02   Use cube cell ✓

Figure D-1: Mesh Refinement Settings Applied to Component Suction of TS002V0003 in TCAE; D_2 = 722 mm.

name	type	reference frame	min refinement	max refinement	layers	gap refinement
Casing-Impeller-leakageinterface	inletInterface	static	3	3	-	4
Impeller-Casing-interface	outletInterface	rotating	2	2	-	4
Impeller_Hub-wall	hub	rotating	1	1	10	4
Impeller_Nozzle-bottomwall	wall	static	3	3	10	4
Impeller_Shroud-wall	shroud	rotating	1	1	10	4
Impeller_blades_LeadingEdges	bladeLeadingEdge	rotating	4	4	10	4
Impeller_blades_PressureSide	bladePressureSide	rotating	1	1	10	4
Impeller_blades_SuctionSuide	bladeSuctionSide	rotating	1	1	10	4
Impeller_blades_TrailingEdges	bladeTrailingEdge	rotating	4	4	10	4
Suction-Impeller-interface	inletInterface	static	2	2	-	4

SnappyHexMesh parameters
Background mesh cell size: 0.01   Use cube cell ✓

Figure D-2: Mesh Refinement Settings Applied to Component Impeller of TS002V0003 in TCAE; D_2 = 722 mm.

name	type	reference frame	min refinement	max refinement	layers	gap refinement
Casing-Impeller-leakageinterface	outletInterface	static	3	3	-	4
Casing-Loft-interface	outletInterface	static	1	1	-	-
Casing-tongue	cutWater	static	2	2	10	4
Casing-wall	wall	static	1	1	10	4
Casing_Hub_bottomwall	hub	rotating	1	1	10	4
Casing_Hub_sidewall	hub	rotating	3	3	10	4
Casing_Nozzle-wall	wall	static	2	2	10	4
Casing_Shroud-topwall	shroud	rotating	4	4	10	4
Casing_Shroud_sidewall	shroud	rotating	4	4	10	4
Casing_Shroud_wall	shroud	rotating	1	1	10	4
Impeller-Casing-interface	inletInterface	rotating	2	2	-	4

SnappyHexMesh parameters
Background mesh cell size: 0.01   Use cube cell ✔

Figure D-3: Mesh Refinement Settings Applied to Component Casing of TS002V0003 in TCAE; D_2 = 722 mm.

name	type	reference frame	min refinement	max refinement	layers
Casing-Loft-interface	inletInterface	static	2	2	-
Loft-OutletPipe-interface	outletInterface	static	0	0	-
Loft-wall	wall	static	0	0	10

SnappyHexMesh parameters
Background mesh cell size: 0.02   Use cube cell ✔

Figure D-4: Mesh Refinement Settings Applied to Component Loft of TS002V0003 in TCAE; D_2 = 722 mm.

name	type	reference frame	min refinement	max refinement	layers
Loft-OutletPipe-interface	inletInterface	static	0	0	-
OutletPipe-ExtraPipe-interface	outletInterface	static	0	0	-
OutletPipe-wall	wall	static	0	0	10

SnappyHexMesh parameters
Background mesh cell size: 0.02   Use cube cell ✔

Figure D-5: Mesh Refinement Settings Applied to Component Outlet Pipe of TS002V0003 in TCAE; D_2 = 722 mm.

HSD

ISAVE

name	type	reference frame	min refinement	max refinement	layers
ExtraPipe-outlet	outlet	static	0	0	-
ExtraPipe-wall	wall	static	0	0	10
OutletPipe-ExtraPipe-interface	inletInterface	static	0	0	-

SnappyHexMesh parameters
Background mesh cell size: 0.02 — Use cube cell ✓

Figure D-6: Mesh Refinement Settings Applied to Component Extra Pipe of TS002V0003 in TCAE; D_2 = 722 mm.

TS002V0004

name	type	reference frame	min refinement	max refinement	layers
Suction-Impeller-interface	outletInterface	static	2	2	-
Suction-inlet	inlet	static	1	1	-
Suction-wall	wall	static	1	1	10

SnappyHexMesh parameters
Background mesh cell size: 0.02 — Use cube cell ✓

Figure D-7: Mesh Refinement Settings Applied to Component Suction of TS002V0004 in TCAE; D_2 = 722 mm.

name	type	reference frame	min refinement	max refinement	layers	gap refinement
Casing-Impeller-leakageinterface	inletInterface	static	4	4	-	5
Impeller-Casing-interface	outletInterface	rotating	2	2	-	5
Impeller_Hub-wall	hub	rotating	2	2	10	5
Impeller_Nozzle-bottomwall	wall	static	5	5	10	5
Impeller_Shroud-wall	shroud	rotating	2	2	10	5
Impeller_blades_LeadingEdges	bladeLeadingEdge	rotating	5	5	10	5
Impeller_blades_PressureSide	bladePressureSide	rotating	2	2	10	-
Impeller_blades_SuctionSuide	bladeSuctionSide	rotating	2	2	10	-
Impeller_blades_TrailingEdges	bladeTrailingEdge	rotating	5	5	10	5
Suction-Impeller-interface	inletInterface	static	2	2	-	5

SnappyHexMesh parameters
Background mesh cell size: 0.02 — Use cube cell ✓

Figure D-8: Mesh Refinement Settings Applied to Component Impeller of TS002V0004 in TCAE; D_2 = 722 mm.

	name	type	reference frame	min refinement	max refinement	layers	gap refinement
	Casing-Impeller-leakageinterface	outletInterface	static	4	4	-	5
	Casing-Loft-interface	outletInterface	static	1	1	-	-
	Casing-tongue	cutWater	static	3	3	10	5
	Casing-wall	wall	static	2	2	10	5
	Casing_Hub_bottomwall	hub	rotating	2	2	10	5
	Casing_Hub_sidewall	hub	rotating	5	5	10	5
	Casing_Nozzle-wall	wall	static	2	2	10	5
	Casing_Shroud-topwall	shroud	rotating	5	5	10	5
	Casing_Shroud_sidewall	shroud	rotating	5	5	10	5
	Casing_Shroud_wall	shroud	rotating	2	2	10	5
	Impeller-Casing-interface	inletInterface	rotating	2	2	-	5

SnappyHexMesh parameters
Background mesh cell size   0.02   Use cube cell ✔

Figure D-9: Mesh Refinement Settings Applied to Component Casing of TS002V0004 in TCAE; D_2 = 722 mm.

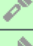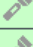|	name	type	reference frame	min refinement	max refinement	layers
	Casing-Loft-interface	inletInterface	static	1	1	-
	Loft-OutletPipe-interface	outletInterface	static	0	0	-
	Loft-wall	wall	static	1	1	10

SnappyHexMesh parameters
Background mesh cell size   0.02   Use cube cell ✔

Figure D-10: Mesh Refinement Settings Applied to Component Loft of TS002V0004 in TCAE; D_2 = 722 mm.

	name	type	reference frame	min refinement	max refinement	layers
	Loft-OutletPipe-interface	inletInterface	static	0	0	-
	OutletPipe-ExtraPipe-interface	outletInterface	static	0	0	-
	OutletPipe-wall	wall	static	0	0	10

SnappyHexMesh parameters
Background mesh cell size   0.02   Use cube cell ✔

Figure D-11: Mesh Refinement Settings Applied to Component Outlet Pipe of TS002V0004 in TCAE; D_2 = 722 mm.

HSD

ISAVE

	name	type	reference frame	min refinement	max refinement	layers
	ExtraPipe-outlet	outlet	static	0	0	-
	ExtraPipe-wall	wall	static	0	0	10
	OutletPipe-ExtraPipe-interface	inletInterface	static	0	0	-

SnappyHexMesh parameters

Background mesh cell size: 0.02   Use cube cell ✔

Figure D-12: Mesh Refinement Settings Applied to Component Extra Pipe of TS002V0004 in TCAE; D_2 = 722 mm.

TS002V0007

	name	type	reference frame	min refinement	max refinement	layers
	Suction-Impeller-interface	outletInterface	static	1	1	-
	Suction-inlet	inlet	static	0	0	-
	Suction-wall	wall	static	0	0	7

SnappyHexMesh parameters

Background mesh cell size: 0.005   Use cube cell ✔
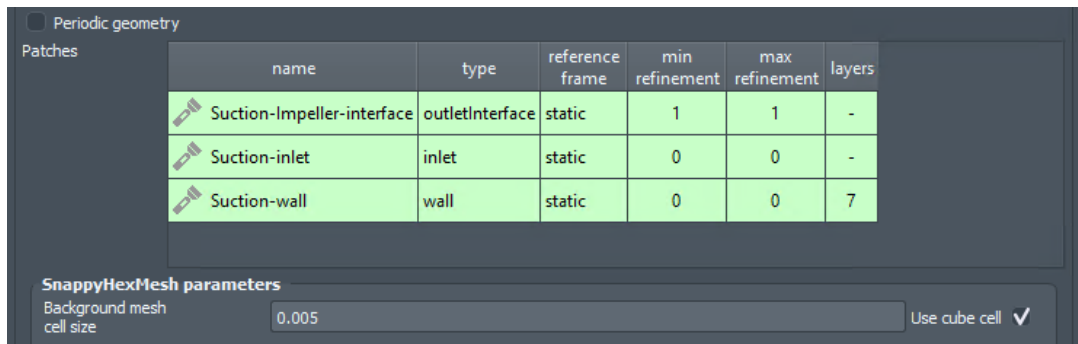
Figure D-13: Mesh Refinement Settings Applied to Component Suction of TS002V0007 in TCAE; D_2 = 722 mm.

	name	type	reference frame	min refinement	max refinement	layers	gap refinement
	Casing-Impeller-leakageInterface	inletInterface	static	3	3	-	-
	Impeller-Casing-interface	outletInterface	static	2	2	-	-
	Impeller_Hub-wall	hub	rotating	2	2	7	-
	Impeller_Nozzle-staticwall	wall	static	3	3	7	4
	Impeller_Shroud-wall	shroud	rotating	2	2	7	4
	Impeller_blade_LeadingEdges	bladeLeadingEdge	rotating	3	3	-	-
	Impeller_blade_PressureSides	bladePressureSide	rotating	1	1	7	-
	Impeller_blade_SuctionSides	bladeSuctionSide	rotating	1	1	7	-
	Impeller_blade_TrailingEdges	bladeTrailingEdge	rotating	3	3	-	-
	Suction-Impeller-interface	inletInterface	static	1	1	-	-

SnappyHexMesh parameters

Background mesh cell size: 0.005   Use cube cell ✔

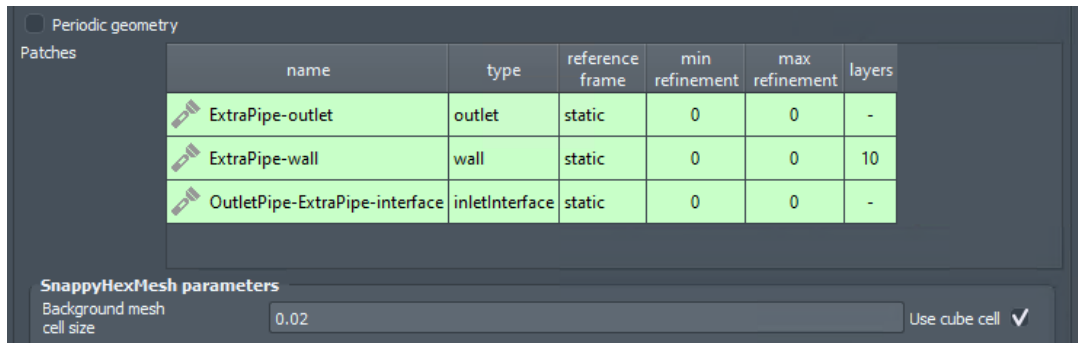**Figure D-14: Mesh Refinement Settings Applied to Component Impeller of TS002V0007 in TCAE; D_2 = 722 mm.**

HSD

ISAVE

name	type	reference frame	min refinement	max refinement	layers	gap refinement
Casing-ExtraPipe-interface	outletInterface	static	1	1	-	-
Casing-Hub-bottomwall	hub	rotating	2	2	7	-
Casing-Hub-sidewall	hub	rotating	3	3	-	-
Casing-Impeller-leakageInterface	outletInterface	static	4	4	-	4
Casing-Shroud-sidewall	shroud	rotating	5	5	-	5
Casing-Shroud-topwall	shroud	rotating	5	5	-	5
Casing-bottomwall	wall	static	2	2	7	-
Casing-tongue	cutWater	static	3	3	-	-
Casing-wall	wall	static	1	1	7	-
Casing_Nozzle-wall	wall	static	3	3	7	4
Casing_Shroud-wall	shroud	rotating	3	3	7	5
Impeller-Casing-interface	inletInterface	static	3	3	-	-

SnappyHexMesh parameters
Background mesh cell size: 0.01   Use cube cell ✓

Figure D-15: Mesh Refinement Settings Applied to Component Casing of TS002V0007 in TCAE; D_2 = 722 mm.

name	type	reference frame	min refinement	max refinement	layers
Casing-ExtraPipe-interface	inletInterface	static	1	1	-
ExtraPipe-outlet	outlet	static	1	1	-
ExtraPipe-wall	wall	static	1	1	7

SnappyHexMesh parameters
Background mesh cell size: 0.01   Use cube cell ✓

Figure D-16: Mesh Refinement Settings Applied to Component Extra Pipe of TS002V0007 in TCAE; D_2 = 722 mm.

TS003V0002

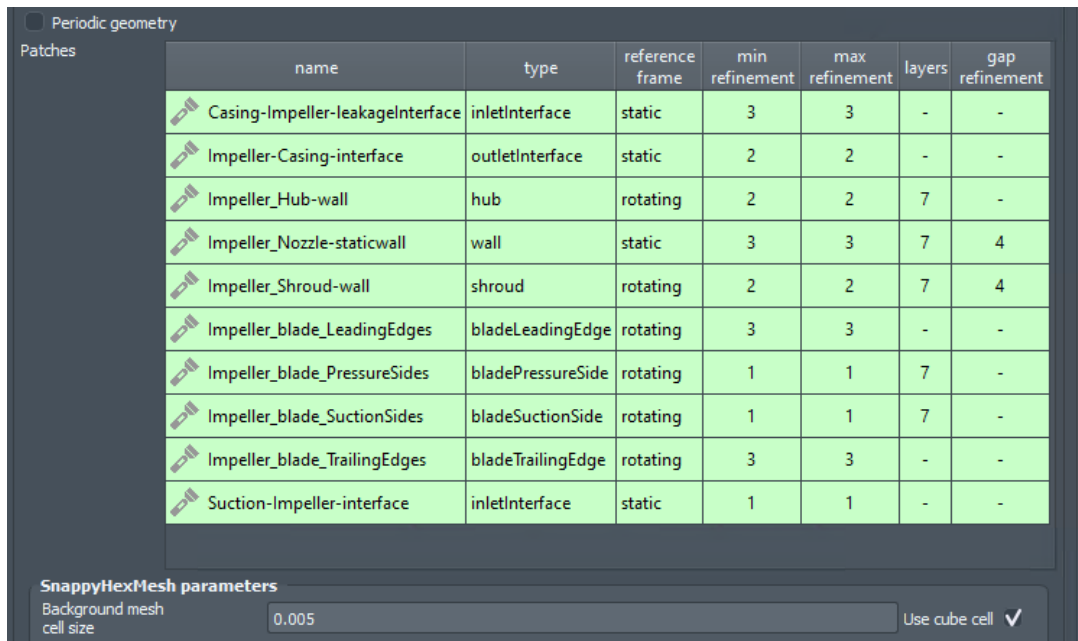| name	type	reference frame	min refinement	max refinement	layers
Suction-Impeller-interface	outletInterface	static	1	1	-
Suction-inlet	inlet	static	0	0	-
Suction-wall	wall	static	0	0	7

SnappyHexMesh parameters
Background mesh cell size: 0.005   Use cube cell ✓

Figure D-17: Mesh Refinement Settings Applied to Component Suction of TS003V0002 in TCAE; D_2 = 741 mm.

Periodic geometry

Patches

name	type	reference frame	min refinement	max refinement	layers	gap refinement
Casing-Impeller-leakageInterface	inletInterface	static	3	3	-	-
Impeller-Casing-interface	outletInterface	static	2	2	-	-
Impeller_Hub-wall	hub	rotating	2	2	7	-
Impeller_Nozzle-staticwall	wall	static	3	3	7	4
Impeller_Shroud-wall	shroud	rotating	2	2	7	4
Impeller_blade_LeadingEdges	bladeLeadingEdge	rotating	3	3	-	-
Impeller_blade_PressureSide	bladePressureSide	rotating	1	1	7	-
Impeller_blade_SuctionSide	bladeSuctionSide	rotating	1	1	7	-
Impeller_blade_TrailingEdges	bladeTrailingEdge	rotating	3	3	-	-
Suction-Impeller-interface	inletInterface	static	1	1	-	-

SnappyHexMesh parameters

Background mesh cell size: 0.005   Use cube cell ✓

Figure D-18: Mesh Refinement Settings Applied to Component Impeller of TS003V0002 in TCAE; D_2 = 741 mm.

Periodic geometry

Patches

name	type	reference frame	min refinement	max refinement	layers	gap refinement
Casing-Impeller-leakageInterface	outletInterface	static	4	4	-	4
Casing-bottomwall	wall	static	2	2	7	-
Casing-outlet	outlet	static	1	1	-	-
Casing-tongue	cutWater	static	2	2	7	-
Casing_Hub-bottomwall	hub	rotating	2	2	7	-
Casing_Hub-sidewall	hub	rotating	3	3	-	-
Casing_Nozzle-wall	wall	static	3	3	7	4
Casing_Shroud-sidewall	shroud	rotating	5	5	-	5
Casing_Shroud-topwall	shroud	rotating	5	5	-	5
Casing_Shroud_wall	shroud	rotating	3	3	7	5
Casing_wall-a	wall	static	1	1	7	-
Casing_wall-nearImpeller	wall	static	2	2	7	4
Impeller-Casing-interface	inletInterface	static	3	3	-	4

SnappyHexMesh parameters

Background mesh cell size: 0.01   Use cube cell ✓

Figure D-19: Mesh Refinement Settings Applied to Component Casing of TS003V0002 in TCAE; D_2 = 741 mm.

Appendix E: Components Map in TCAE for All Simulation Models

The following figures show the components map for all the CAD models used for numerical simulations. The component map highlights direction of flow of fluid through different components and interfaces.
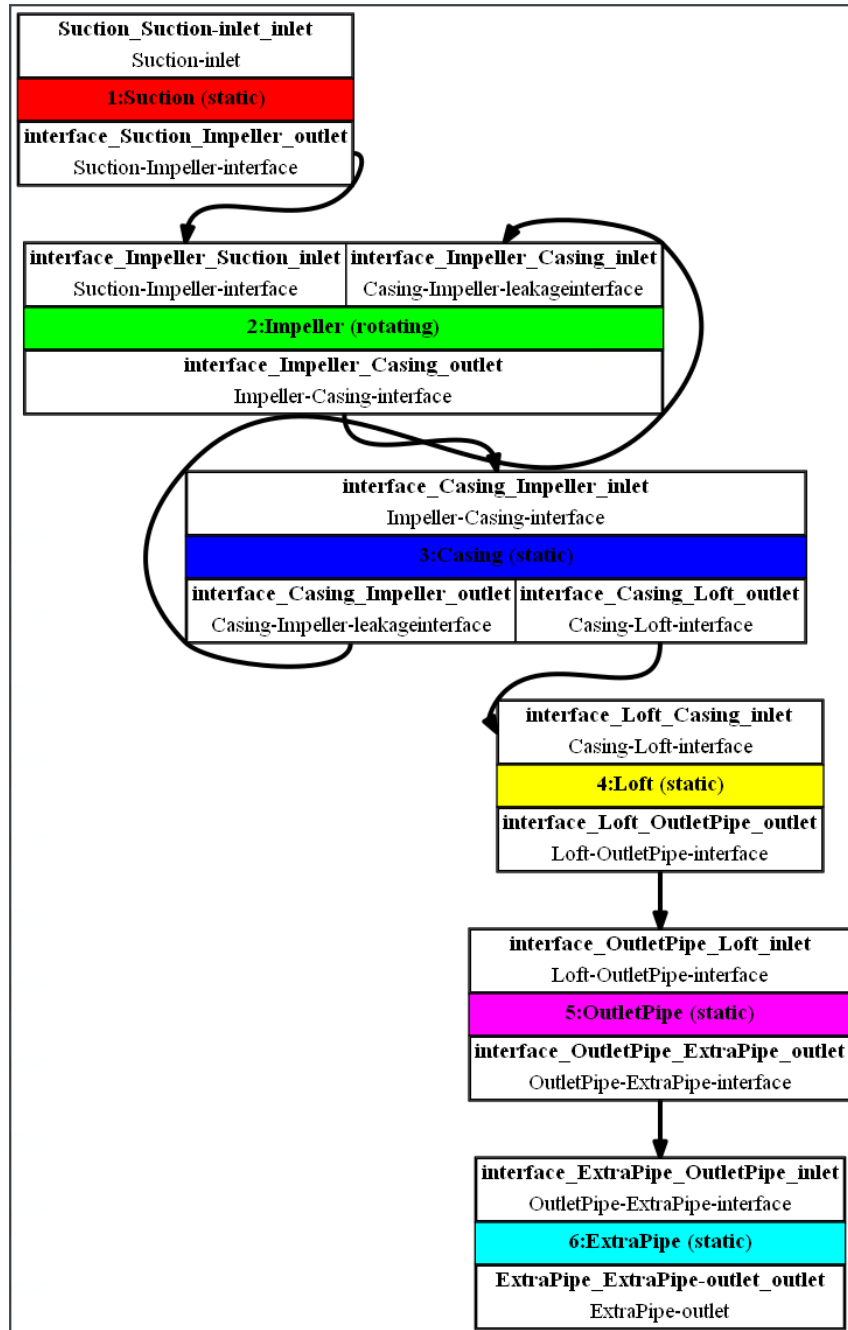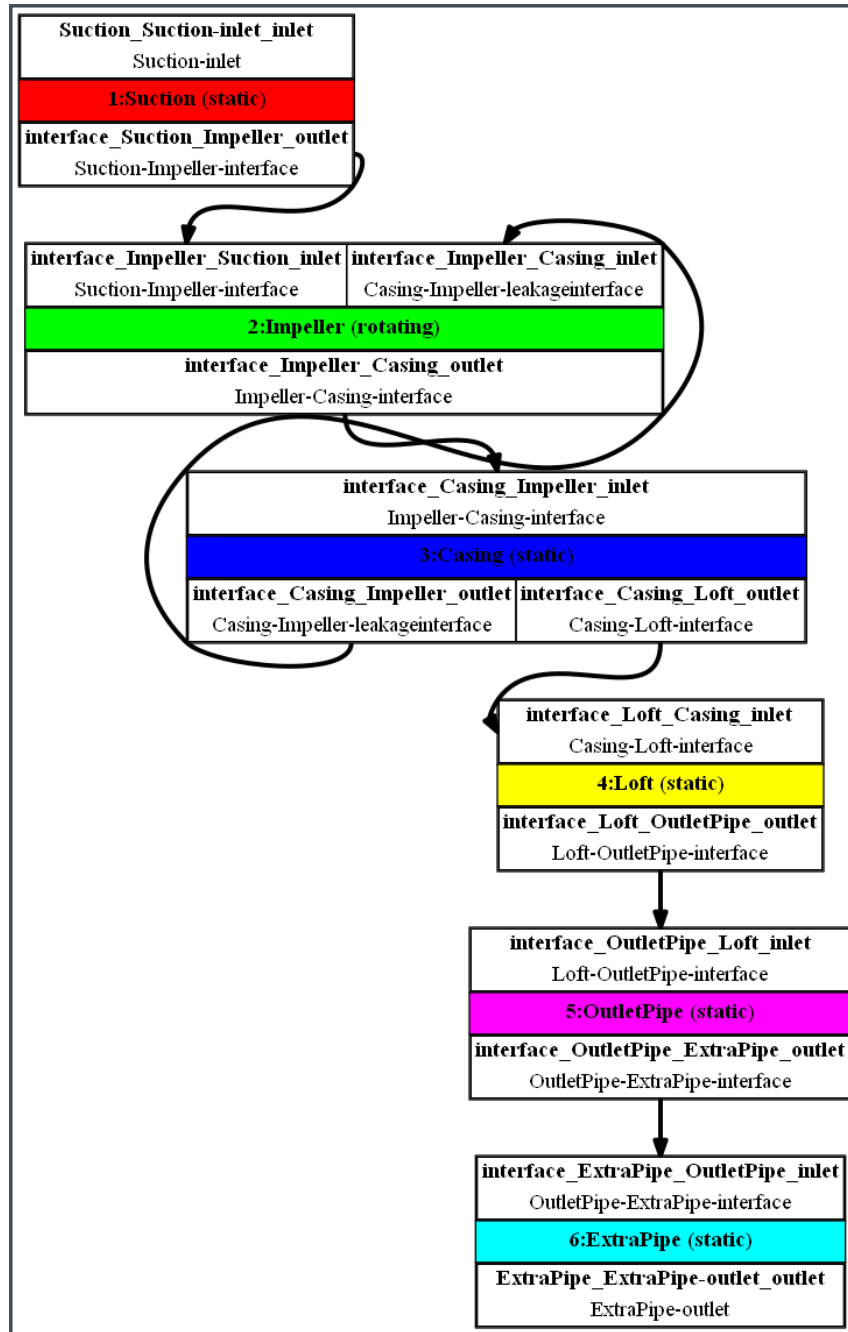

Figure E-1: Components Map for TS002V0003 in TCAE; D_2 = 722 mm.

HSD   ISAVE

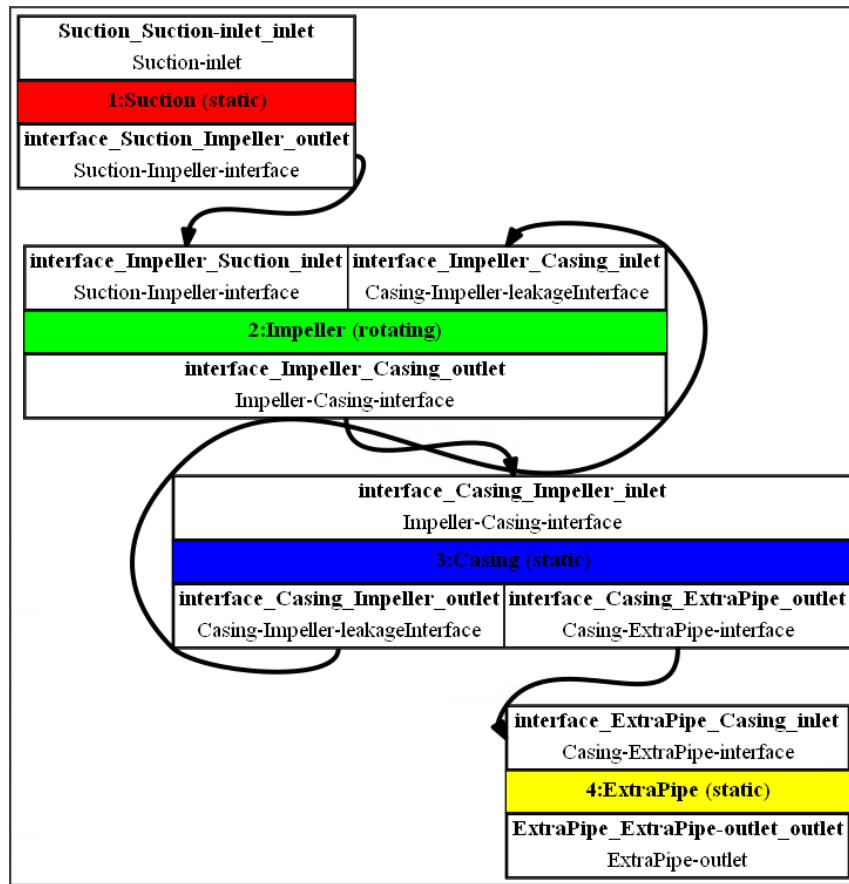**Figure E-2: Components Map for TS002V0004 in TCAE;** D_2 = 722 mm.

Figure E-3: Components Map for TS002V0007 in TCAE; D_2 = 722 mm.

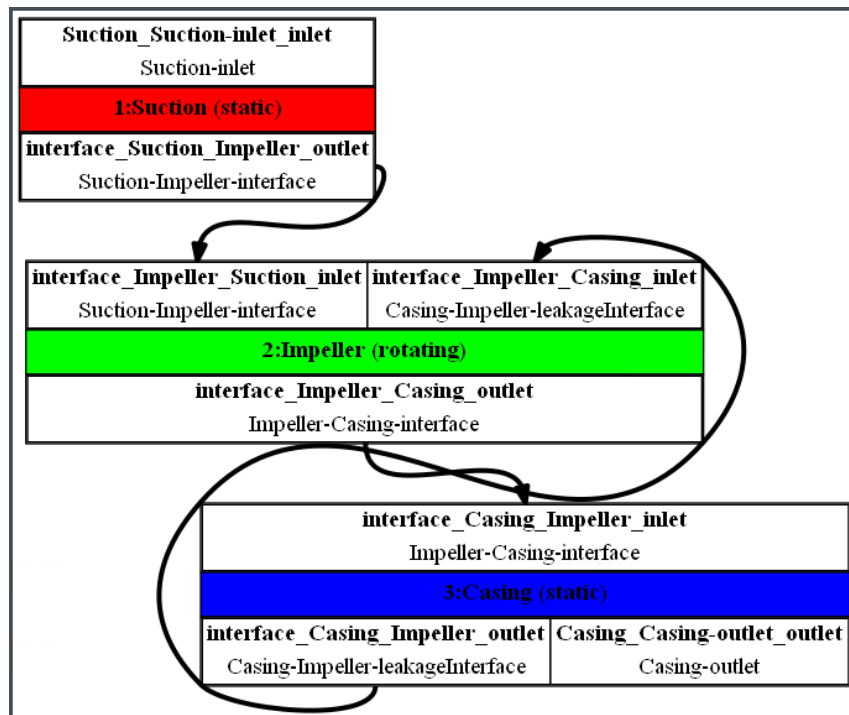**Figure E-4: Components Map for TS003V0002 in TCAE; D_2 = 722 mm.**

Appendix F: Dimensional Quantities of Fan Models

	RV722	TS003V0002
Impeller Outer Diameter, $D_2[mm]$	722	740.8
Impeller Inlet Diameter, $D_1[mm]$	315	321.2
Blade Outlet Width, $b_2[mm]$	92.7	97.8
Blade Inlet Width, $b_1[mm]$	132.5	138.5
Shroud Angle, γ	11°	11°
Blade Outlet Angle, β_2	41°	41.3°
Blade Inlet Angle, β_1	31°	31.3°
Shroud Radius of Curvature, $r_D[mm]$	45	45
Suction Nozzle Radius of Curvature, $r_D[mm]$	45	45
Suction Pipe Diameter, $D_A[mm]$	400	405
Gap Width, $s_w[mm]$	3.2	3.2
Gap Length, $s_l[mm]$	12.6	12.9
Casing Width, $B[mm]$	315	304.8
Impeller Blade Radius, $R[mm]$	383.3	394.8
Number of Blades, $s_w[mm]$	10	10
$r_z[mm]$	361	370.4
$r_1{'}[mm]$	469.9	430.7
$r_2{'}[mm]$	531	500.8
$r_3{'}[mm]$	599.9	582.2
$r_4{'}[mm]$	677.6	676.9
$R_1[mm]$	443.3	400.6
$R_2[mm]$	502	465.8
$R_3[mm]$	567.1	541.6
$R_4[mm]$	640.6	629.7
Casing Material Thickness, $[mm]$	3	3
Impeller Blade Material Thickness, $[mm]$	3	3
Hub Material Thickness, $[mm]$	5	5
Shroud Material Thickness, $[mm]$	2	2
Nozzle Material Thickness, $[mm]$	2	2

Table F-1: Important Dimensional Quantities for the Reference Fan RV722 and the Newly Designed Fan TS003V0002.

HSD

ISAVE

Declaration in lieu of Oath

I, Abhishek Gangappa Hallur, hereby declare in lieu of oath that I have written this Master's thesis independently and have not used any aids or sources other than those specified.

This is the version to be evaluated by the Düsseldorf University of Applied Sciences.

Place, Date ___Düsseldorf, 19.09.2024___ Signature ___*(signature)*___

Eidesstattliche Erklärung

Hiermit versichere ich, Abhishek Gangappa Hallur, an Eides statt, die vorliegende Master-Thesis selbständig verfasst und keine weiteren als die angegebenen Hilfsmittel und Quellen benutzt zu haben.

Dies ist die von der Hochschule Düsseldorf zu bewertende Version.

Ort, Datum ___Düsseldorf, 19.09.2024___ Unterschrift ___*(signature)*___